

Solid Lubrication Bearing Design Through Analytical and Empirical Vibration Analysis of Characteristic Frequencies

Christopher A. Schultz
Marquette University

Recommended Citation

Schultz, Christopher A., "Solid Lubrication Bearing Design Through Analytical and Empirical Vibration Analysis of Characteristic Frequencies" (2015). *Master's Theses (2009 -)*. 310.
https://epublications.marquette.edu/theses_open/310

**SOLID LUBRICATION BEARING DESIGN THROUGH ANALYTICAL
AND EMPIRICAL VIBRATION ANALYSIS
OF CHARACTERISTIC FREQUENCIES**

by

Christopher A. Schultz, B.S.

A Thesis submitted to the Faculty of the Graduate School, Marquette University,
in Partial Fulfillment of the Requirements for the
Degree of Master of Science in Mechanical Engineering

Milwaukee, Wisconsin

May 2015

ABSTRACT
SOLID LUBRICATION BEARING DESIGN THROUGH ANALYTICAL
AND EMPIRICAL VIBRATION ANALYSIS
OF CHARACTERISTIC FREQUENCIES

Christopher A. Schultz, B.S.

Marquette University, 2015

Ball bearings with solid lubrication lack the damping mechanisms of oil and produce well-defined vibration characteristics based upon given geometry and speed of operation. This work takes advantage of the high signal to noise ratio in x-ray bearings and develops an algorithm to statistically track bearing performance based upon fundamental bearing theory, Monte Carlo simulation, Order Analysis, and Weibull statistics. The technique gathers vibration data solely related to the theoretical operation of a bearing, negates the background noise, and provides descriptive vibration amplitude statistics of individual bearing components for evaluation.

The practical implications of the thesis described herein allow the bearing engineer to optimize designs for life and noise by essentially tracking bearing component condition during operation. The output of the research is a tool/methodology to study and describe the vibration pattern of a bearing in operation. The concepts are tested and verified through the creation of a vibration transfer function between a sub-assembly bearing test rig and a bearing at full assembly level. Developed with Weibull statistics, the function correctly describes populations of vibration amplitude approximately 50% of the time within a 72% confidence interval. This was possible because the statistical methodology created found physically meaningful vibration patterns, not random vibration patterns.

ACKNOWLEDGEMENTS

Christopher A. Schultz, B.S.

The completion of this capstone project is the result of help from numerous individuals through which it otherwise would not be possible. First and foremost, I would like to extend my utmost gratitude to my wife, Megan. Thank you so much for your patience and support (some would say perseverance) in this pursuit of a higher education throughout these last few years. I hope to one day live up to your level of love and understanding.

Dr. James Rice provided just the right amount of hands-on support and focus, specifically on the written portion of the thesis. Thank you for your many hours of proofreading, use of red pen, and guidance to bring the project into perspective for an audience.

I also would like to thank my co-workers Strider Hunt, Mike Danyluk, and Gayle Armstrong. Specifically, my manager Tom Murray deserves much credit for backing the whole endeavor, classwork and thesis alike. Thank you for the encouragement and continued support.

Finally, a special thanks to Nancy, Steve, Tim, Darrell, and Marilyn Schultz is required. The five of you provided the sound foundation I use to start each day of the rest of my life. Dad, you are the smartest man I have ever met and expect to ever meet. Mom and Dad, please hold this thesis as accreditation of your success as parents.

TABLE OF CONTENTS

ABSTRACT.....	2
1 Introduction	11
1.1 Problem Statement.....	12
1.2 Objective of Work	14
1.3 Focus of Work	15
2 Literature Review.....	16
2.1 Overview of X-ray Production for Diagnostic Imaging.....	16
2.2 X-ray and Bearing Environment	18
2.3 Fundamental Bearing Design	21
2.3.1 Bearing Materials: Races and Balls	22
2.3.2 Bearing Materials: Lubrication.....	23
2.3.3 Bearing Design Geometry	29
2.3.4 Application of Bearing Geometry	31
2.3.5 Thermal Compensation.....	33
2.4 Bearing Characteristic Frequencies.....	39
3 Data Collection Procedures.....	44
3.1 Bearing Assemblies Under Test	45
3.2 Test Platforms	48
3.3 Raw Data Collection: Vibration Measurements and Frequency Transformation.....	53

3.4	Procedures Used for Development of Matlab Model.....	60
3.4.1	Initial Data Review: Microsoft Excel	61
3.4.2	Data Observations	65
3.4.3	Model Refinement: Monte Carlo Simulation.....	67
3.4.4	Runspeed Normalization Through Order Analysis.....	74
4	Results and Discussion	77
4.1	Matlab Vibration Analysis Tool	78
4.1.1	Runspeed Detection and the Application of Order Analysis	79
4.1.2	Spectral Analysis and Data Mining.....	84
4.1.3	Effectiveness of Matlab Vibration Analysis Algorithm	87
4.1.4	Data Storage	100
4.1.5	Data Analysis: Method of Descriptive Vibration Amplitude Statistics.....	103
4.2	Vibration Transfer Function	109
4.2.1	Visual Observations	110
4.2.2	Bearing Test Rig and Casing Measurement System Correlation Methodology.....	115
4.2.3	Effectiveness of Transfer Function	122
5	Conclusions and Recommendations	125
	BIBLIOGRAPHY	127

LIST OF TABLES

Table 2.1: Melting Point of Lead and Silver.	26
Table 2.2: Technical and dimensional characteristics of a bearing specified on a print [15].	29
Table 2.3: Bearing design equations [15, 17].	30
Table 2.4: Calculations of the elliptical shape of the contact area.	36
Table 3.1: Monte Carlo simulation of inner race defect frequency due to component tolerance stackup.	68
Table 3.2: Effect of rotor slip on resonant and harmonic frequencies.	70
Table 3.3: Monte Carlo simulation: inner race defect frequency due to component tolerance stackup & runspeed variation.	73
Table 3.4: Summary of the influence of component and runspeed tolerance stackup on theoretical frequencies.	75
Table 4.1: Resonant characteristic bearing frequencies at a constant, normalized runspeed of 100Hz.	85
Table 4.2: Third harmonic calculations.	86
Table 4.4: Example of Weibull statistics of outer race vibration amplitude distributions.	108
Table 4.5: Sample data set from bearing 178404GI0 at casing level.	118
Table 4.6: Bearing specific transfer function of eta values.	120
Table 4.7: Accuracy of transfer function for ten predictions.	122

TABLE OF FIGURES

Figure 2.1: Example of an x-ray tube [46].	17
Figure 2.2: Example of the use of an x-ray anode without rotation.	18
Figure 2.3: Cross-section of an x-ray tube anode.	19
Figure 2.4: Damaged bearing spectrum compared to an undamaged bearing spectrum [15].	24
Figure 2.5: Peaks in failing bearing distinctly rising above the broadband noise [36].	25
Figure 2.6: Example of distinct characteristic vibration peaks of an x-ray bearing spectrum.	26
Figure 2.7: Tracks through fresh snow [36].	27
Figure 2.8: Cross-section of radial ball bearing with contact angle [15].	32
Figure 2.9: Reaction forces on bearings.	34
Figure 2.10: Shaft (inner race) load distribution [4].	35
Figure 2.11: Ball load distribution [4].	35
Figure 2.12: Elliptical stress distribution in point contact [4].	36
Figure 2.13: Bearing Equation Mind Map.	37
Figure 2.14: Elastic compliance of ball bearing [19].	39
Figure 2.15: Outer race defect [37].	40
Figure 2.16: SKF ball bearing.	41
Figure 2.17: Amplitude modulation and sidebands [10].	42
Figure 2.18: Amplitude modulated sidebands [18].	43
Figure 3.1: Block diagram of data collection procedures.	44
Figure 3.2: Bearing assembly under test.	45
Figure 3.3: One of two bearings in bearing assembly.	45
Figure 3.4: Two of two bearings in bearing assembly.	45
Figure 3.5: Anode assembly under test.	47

Figure 3.6: Cross-section of anode assembly.....	47
Figure 3.7: Full casing-level x-ray tube.	48
Figure 3.8: Bearing test rig platform.....	49
Figure 3.9: Cross-section of anode-end of bearing rig design.	49
Figure 3.10: Diagram of simple harmonic motion [33].....	50
Figure 3.11: Examples of different methods torque star-patterns [7].	51
Figure 3.12: Accelerometer placement on x-ray tube casing.	54
Figure 3.13: Accelerometer system response [22].	54
Figure 3.14: Vibration in time series [26].	55
Figure 3.15: Synopsis of Fast Fourier Transform [27].	56
Figure 3.16: Measuring an integer number of periods gives an ideal FFT [43].	57
Figure 3.17: Measuring a non-integer number of periods adds spectral leakage to the FFT [43].	58
Figure 3.18: Applying a window minimizes the effect of spectral leakage [43].	58
Figure 3.19: Example of FFT spectral data from test procedures.....	62
Figure 3.20: Bearing 1, Measurement 1: 786Hz.	63
Figure 3.21: Bearing 1, Measurement 2: 783Hz.	63
Figure 3.22: Bearing 1, Measurement 3: 784Hz.	64
Figure 3.23: Vibration spectrum indicating runspeed vibration peak.	69
Figure 3.24: Vibration spectrum zoomed in on runspeed vibration spike.	69
Figure 3.25: Bearing 1, Measurement 1	71
Figure 3.26: Bearing 1, Measurement 2	72
Figure 3.27: Bearing 1, Measurement 3	72
Figure 3.28: Probability distribution comparisons of component and speed variations.	75
Figure 4.1: Block diagram of vibration analysis algorithm.....	78

Figure 4.2: Raw dataset of FFT spectrum: to be used to demonstrate order analysis.....	80
Figure 4.3: Runspeed vbe at 98Hz with set point of 100Hz.....	80
Figure 4.4: Inner race vbe at 769Hz with 98Hz runspeed.....	80
Figure 4.5: Monte Carlo graph of expected inner race frequencies.....	80
Figure 4.6: Raw dataset shifted by 100/98 for all frequencies.....	81
Figure 4.7: Normalized dataset to be used for vibration analysis.	82
Figure 4.8: Runspeed vbe at 100Hz	82
Figure 4.9: Inner race freq. at 786Hz due to 100Hz runspeed.....	82
Figure 4.10: Monte Carlo graph of expected inner race frequencies.....	82
Figure 4.11: Characteristic peaks first identified in Excel to be captured for analysis in the vibration analysis program.	87
Figure 4.12: Characteristic peaks identified and captured with Matlab algorithm for statistical analysis.....	88
Figure 4.13: Characteristic peaks identified and captured with Matlab algorithm for statistical analysis.....	90
Figure 4.15: Shaft speed harmonic peak and ball defect frequency peak.....	94
Figure 4.16: BDF error propagates through to harmonics.....	95
Figure 4.17: Correlation between measurements of a single bearing on the test rig.....	97
Figure 4.18: Measurement correlation within bearing rig system. One bearing's vibration signature trends to itself over multiple measurements.	98
Figure 4.19: Vibration amplitudes from Matlab program plotted against standardized frequency values.	102
Figure 4.20: Example of Matlab vibration amplitude output of resonant frequencies and harmonics.	104

Figure 4.21: Probability density function of outer race defect frequency vibration amplitude distribution.....	105
Figure 4.22: Weibull distribution examples with differing effects of the shape parameter β [42].	106
Figure 4.23: Two Weibull probability density functions to compare defects between bearings.	108
Figure 4.24: Example 1 of casing level vibration compared against bearing rig, 0-5000Hz.	111
Figure 4.25: Example 1 of casing level vibration compared against bearing rig, 0-2000Hz.	112
Figure 4.26: Example 2 of casing level vibration compared against bearing rig.	113
Figure 4.27: Diagram of Data Collection and Analysis for Transfer Function Development	116
Figure 4.28: Conceptual example of different system responses for the same bearing.	119
Figure 4.29: Conceptual review of the confidence intervals of the transfer function.	121
Figure 4.30: Graph of percent accuracy at each frequency for ten bearings.	122
Figure 4.31: Transfer function with the best correlation between predicted and measured data at casing level.....	123
Figure 4.32: Transfer function with the worst correlation between predicted and measured data at casing level.....	124

1 Introduction

This work specifically focuses on ball bearings for use in the application of x-ray production. It can, however, be transferred to any work involving the use of bearings with solid lubrication or any other type of lubrication and any application of machine condition monitoring.

The application of x-ray bearings is unique because most bearings in the world operate with grease or oil; x-ray bearings use solid lubrication such as lead or silver because they operate in a vacuum in temperatures above 500°C. The motivation for this work stems from the fact that there does not exist industry standards to efficiently develop and test bearings with solid lubrication for life and noise in an x-ray environment. The design cycle of an x-ray bearing is resource intensive. For all intents and purposes, this work will provide the tools and foundation to fail faster, reduce costs, and increase efficiency to expedite the x-ray bearing design cycle.

The oil in conventional bearings suppresses and/or dampens vibration during operation [15]. Ball bearings with solid lubrication, such as those used in an x-ray environment, lack oil and therefore create an advantage to the process of machine condition monitoring. This work exploits the lack of oil. The lack of damping provides access to component-specific vibration amplitudes during operation for statistical analysis as a means to describe component condition. The following thesis is an analytical technique to predict the location of discrete vibration spikes with fundamental bearing theory, Monte Carlo simulation, and Order Analysis. A technique such as this can be used to optimize the life and noise of bearings with solid lubrication by tracking the component statistics throughout testing and life-cycles. The work is concluded with the application of a vibration transfer function between a sub-assembly and a full assembly.

1.1 Problem Statement

There exists today extensive research on rolling contact fatigue, life, and vibration analyses for oil and grease bearings [15, 30]. More often than not, what is absent from both literature and industry is research into the more specialized application of solid film lubrication, such as silver, in an x-ray environment. In fact, the operating environment is so specialized there are less than a handful of suppliers in the world that produce bearings of sufficient quality, cleanliness, and precision required to operate in a high vacuum, high voltage, and high heat environment. The increased specialization severely limits the amount of knowledge available to take on credible design work.

Bearing manufacturers and their employed design engineers have more than sufficient knowledge to specify a theoretically optimized design based on first principles. However, the companies do not have the ability to empirically test a given design for noise and life because it is difficult to reproduce the x-ray environment: bearing companies are bearing experts, not x-ray, high-voltage, and vacuum experts.

The end use-case of an x-ray bearing varies drastically from use-case to use-case. To complicate the matter, the use-case is often proprietary information that belongs to the x-ray tube designer, not the bearing designer. Bearing companies have domain knowledge of bearings but fall short of knowledge in x-ray production fundamentals. For example, they lack the basic boundary conditions associated with radiation heat transfer in a vacuum. The x-ray tube designer's choice of geometry, emissivity, mass, and even materials are unbeknownst to the bearing designer, let alone the thermal protocols and load on the bearing itself. This type of information is considered proprietary and is not readily available to the bearing engineer.

The x-ray environment is a black box of sorts which makes it difficult for bearing designers to prove out, compare, and/or optimize designs. To what standard should they design? Engineers at bearing companies have tried to implement test rigs, but it is no trivial pursuit; their efforts were quickly abandoned. In the bearing industry, there does not exist the ability to quickly and cost effectively cycle through Designs of Experiments (DOE) for x-ray applications. The motivation of this work is to develop a means of statistical vibration analysis to compare bearings against one another and populations of bearings against one another to extend design capabilities and reduce costs.

1.2 Objective of Work

For bearing design, generally two things are of concern: life and noise. This work develops the methodology and logic to statistically describe the condition of components by focusing on fundamental vibration frequencies tied to bearing theory. The objective of this research is to increase the diagnostic capabilities of solid lubrication bearings by taking advantage of the lack of oil damping in the bearing assembly.

The success of this embodiment is defined as the ability to reliably and repeatedly find the expected frequency vibration peak within spectral data. An accelerometer captures the vibration amplitudes over a given frequency range of interest. The data runs through a Fast Fourier Transform (FFT) and is converted from the time to the frequency domain. It is hypothesized that the fundamental bearing characteristic vibrations are well-defined and traceable in a bearing with solid lubrication. The ensemble of data will be used to describe the condition of the bearing and its components with a characteristic value bounded by a given confidence limit with Weibull statistics. Upon successful proof of the aforementioned hypothesis, the resulting concepts and algorithms can be used to evaluate and compare bearing designs, trend performance over time, and/or decrease design cycle time. The research does not attempt to optimize a bearing design but instead lays out a tool to that effect to be applied to both noise and life.

Finally, this work concludes with the application of the statistical algorithm to create a vibration transfer function between a sub-assembly and a full assembly. This is an example of a use of the design tool to verify the concepts presented and an example to increase design cycle efficiency.

1.3 Focus of Work

The objective of this work will be fulfilled by focusing on the use of ball bearings with solid film lubrication for x-ray production in healthcare diagnostic imaging. Solid lubrication is necessary because the bearing operates at high temperatures in a vacuum, an environment not meant for oils or greases with low vapor pressures. This work provides an analytical technique to predict the location of discrete vibration spikes based upon fundamental bearing theory, Monte Carlo simulation, and Order Analysis. The concepts and theories presented are verified with the use of a vibration transfer function between an x-ray anode sub-assembly and x-ray tube assembly. The reason for the transfer function is to establish proof of concept that characteristic vibration patterns create statistical significance that can be used for design optimization purposes. The existence of a transfer function between two entities directly indicates a relationship and is possible when the characteristic vibration patterns are meaningful, not random. The transfer function accomplishes the following:

1. Establishes proof of concept to support the theory that statistics describe vibration
2. Creates a platform in which to compare designs in a "Design of Experiments" fashion
3. Reduces design cycle resource requirements

The work is completed under vacuum with solid lubrication, both conditions not readily documented or accomplished in the bearing industry. An x-ray tube and operation of a bearing in an anode is described in the literature review section. Additionally, a large portion of this paper focuses on bearing fundamentals as a means to develop a sufficiently well understood knowledge base of the physics under test.

2 Literature Review

2.1 Overview of X-ray Production for Diagnostic Imaging

Healthcare in the world today becomes increasingly more important as the population ages. Non-invasive technologies, like diagnostic imaging through use of x-ray, help promote faster diagnoses without complications and costs of exploratory surgery. CT (computed tomography) scanners, for example, are critical pieces of equipment in emergency situations often when there is literally no time available to waste for the safety of the patient. Hospitals count on system reliability to create an image every time.

An x-ray system for diagnostic imaging generally includes a detector, an x-ray tube, and a bearing to support the rotation of a target/anode inside the x-ray tube. X-rays originate from the tube, pass through a patient, and are captured on the detector. The patient attenuates the x-rays passing through on the way to the detector. The detector creates an image by converting different levels of attenuated x-ray beam into data [29].

More specifically, x-rays originate on the surface of a rotating target. Below is a schematic of an x-ray tube. This assembly consists of a filament (the cathode) and a target (the anode). A large potential difference (beyond 100 kilovolts) across the tube pulls electrons off of the filament in a focused beam that bombards the spinning target material. The electron beam knocks out of orbit the electrons in the target material. When the target electrons change orbit in this manner, they release energy in the x-ray spectrum to be used for purposes of diagnostic imaging. Of all the energy that goes into producing the x-rays, about 99% goes to heat. Therefore, most bearings conduct heat out of the system and operate beyond the 500°C temperature level [29].

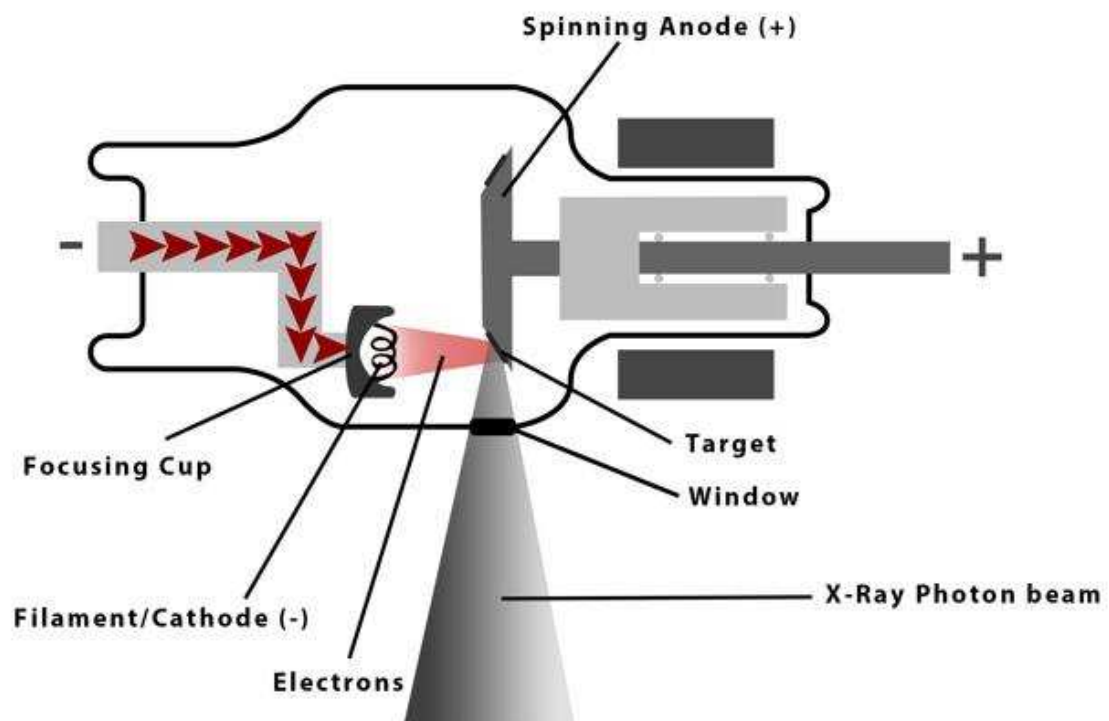


Figure 2.1: Example of an x-ray tube [46].

2.2 X-ray and Bearing Environment

The focal spot rises to about 2900°C during x-ray production with a heat flux up to 8300 W/mm^2 . The thermal energy focused on a small area can easily melt and/or vaporize a hole through a stationary target material as shown below in the picture [16, 40].

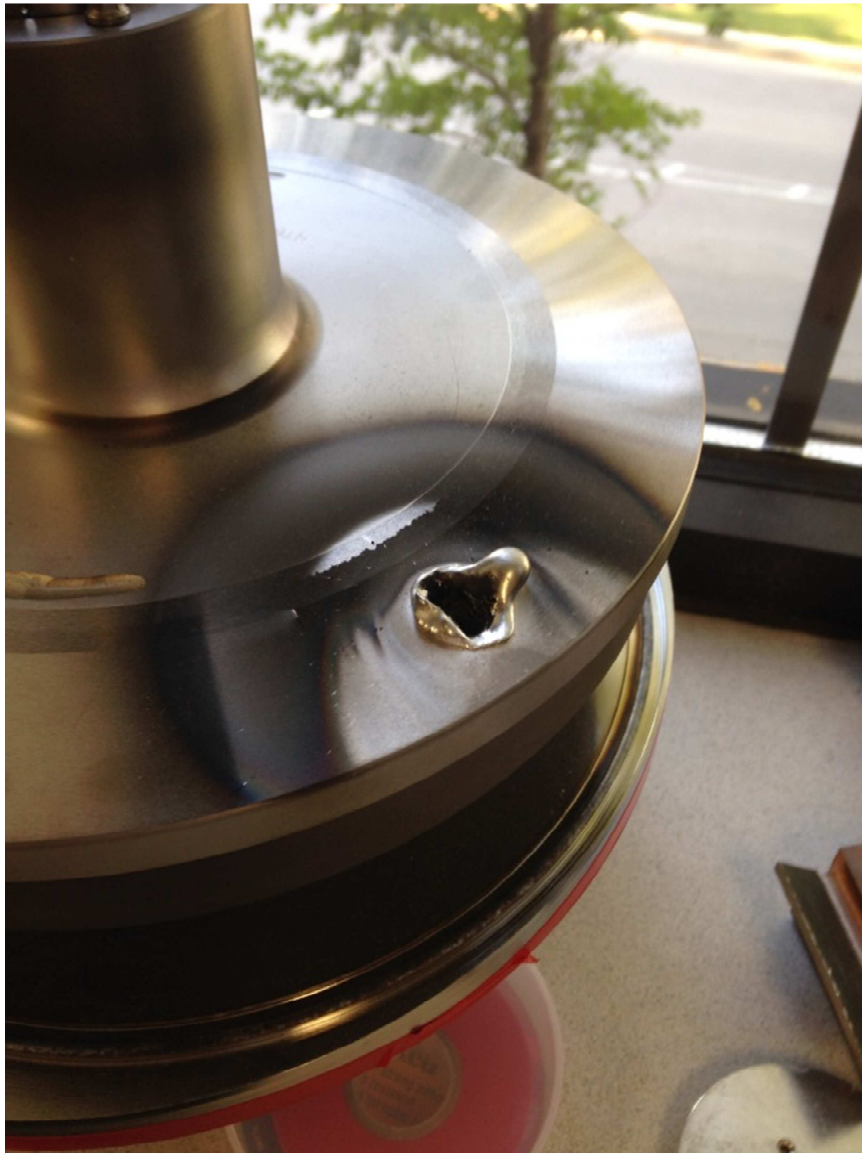


Figure 2.2: Example of the use of an x-ray anode without rotation.

Therefore, the x-ray tube typically rotates the target to deliver fresh material for purposes of distributing heat generated at the focal spot [29]. Catastrophic material failure, as evidenced in

the picture above, is avoided because rotation keeps the heat generation per unit area per unit time at a permissible level during x-ray production. As such, the anode must be composed of an integral bearing assembly to rotate the target assembly [16, 40], generally from 6k-10k RPM.

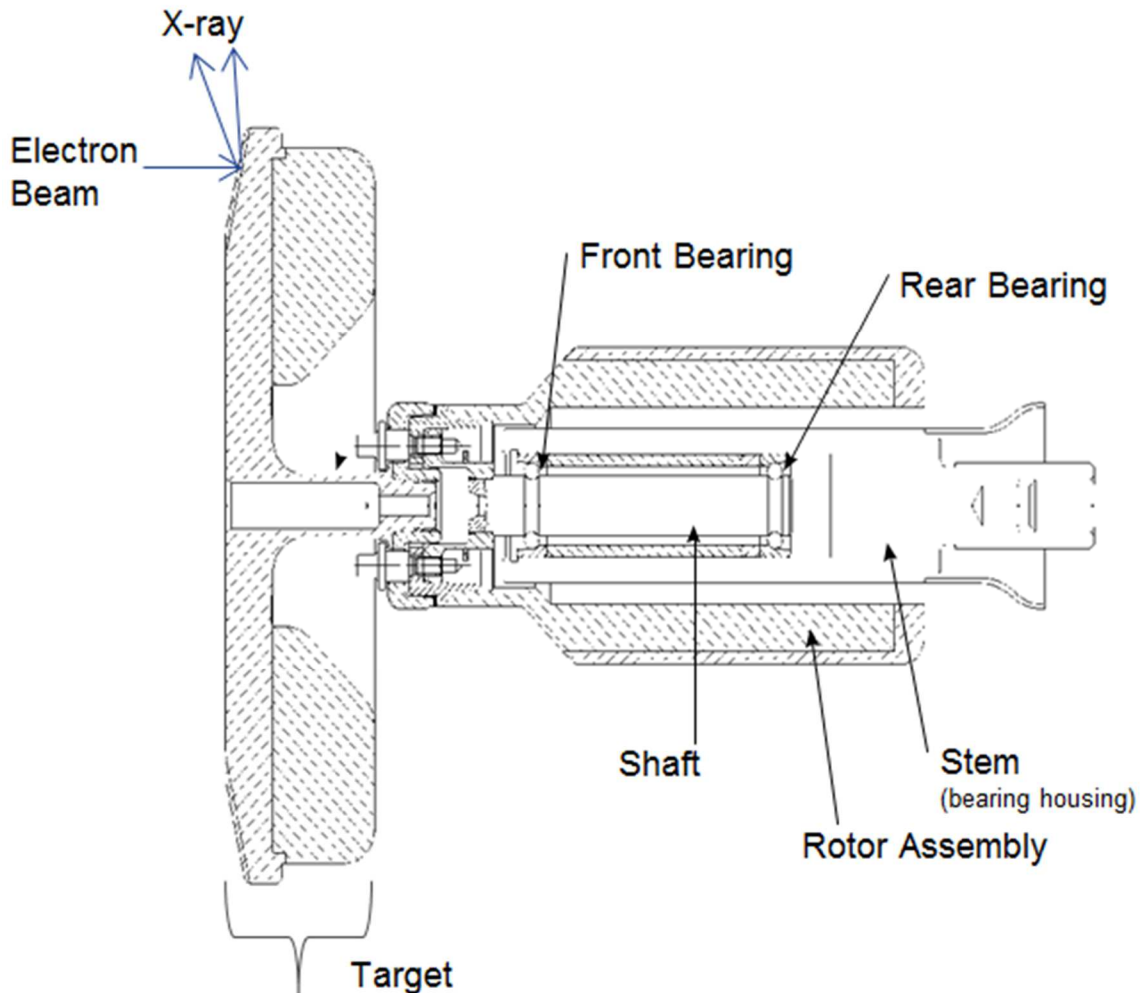


Figure 2.3: Cross-section of an x-ray tube anode.

The figure above is a cross-section example of an x-ray tube anode. The entire assembly operates in a high vacuum (below $10^{-4} Pa$) environment to reduce high voltage instability when 100,000+ volts are applied across the system. The heat generated at the focal spot conducts through the assembly system and causes the bearing to experience high temperatures, up to $550^{\circ}C$ [16].

The convergence of high vacuum, high voltage, high heat, and high rotation speeds sets up a specialized environment in which to operate. The bearing's balls and races must maintain high strength and hardness at elevated temperatures. They are typically made of a high speed tool steel which works well in the 400 – 500°C range with stresses up to 2.5GPa [29].

Traditional lubrication techniques such as grease and oil outgas into the high vacuum, high voltage environment rendering the tube electrically unstable; any particulate instantly becomes a lightning rod. Therefore, there is another means to provide lubrication to the system. "X-ray tube bearing rolling elements are typically coated with a solid layer, or tribological system of a metal with lubricating properties, such as silver" applied with an ion plating or electroplating process [29]. Additionally, the bearing and lubricant must conduct electricity to complete the cathode-electron beam-anode circuit.

Typical failure modes include contamination, wear of the plated lubricant, and loss of lubricant in the contact region [29]. More subjectively, a bearing can have sub-optimal operating characteristics, like noise, that don't necessarily inhibit x-ray production, but diminish the perception of quality. Or, on the other hand, noise, and inherently vibration, could forecast imminent failure as well.

The extreme conditions explored above create a specialized use-case not easily or cost effectively replicated. It is the intent of this research to increase the documentation and work around the optimization of bearings with solid lubrication through the development of predictive, traceable vibration characteristics. The introduction of a test rig enables test repeatability, reduces costs, and reduces cycle time. The introduction of Weibull statistics provides a method to track component condition and performance.

2.3 Fundamental Bearing Design

A working knowledge of fundamental bearing design and the important characteristic frequencies allows one to pull useful data from a vibration spectrum. The section to follow highlights metallurgical and then geometrical considerations of bearing design, as well as how design considerations impact vibration. The knowledge gained through this rudimentary review establishes the foundation of the methodology to optimize bearing life and noise through vibration analysis.

2.3.1 Bearing Materials: Races and Balls

When making material choices, several considerations are in order. The materials must be compatible with the use case and system-level influences. The material must be vacuum compatible and extremely clean for operation. If they are not, the system runs the risk of contaminating the vacuum space, which causes high voltage instability and renders the tube inoperable.

The material must maintain high strength and hardness during operation up to 550°C. In general, high speed tool steels like SKH4 or Rex20 are acceptable [16, 29]. These two materials each exhibit high moduli of elasticity to resist plastic deformation. As a frame of reference, aluminum is about 68GPa whereas bearing tool steels are 230+GPa with hardness above 60HRC. Large values of elastic moduli and hardness resist damage and wear quite well.

The ball and race materials must also be electrically conductive to create x-rays. The process is driven by a potential difference beyond 100,000V. The cathode sends an electron beam to the target/anode, so any materials touching the target must aid in conduction to complete the circuit. This requirement therefore reduces the choice of materials. For example, it would be advantageous to use ceramic balls for their increased strength and superior modulus of elasticity. They also have superior surface finishes relative to most steel balls available. The improved surface finish not only functionally lasts longer, but operates more quietly than their steel counterparts. However, ceramics do not conduct electricity and are not used in x-ray bearings.

2.3.2 Bearing Materials: Lubrication

X-ray bearings require the use of a solid lubricant such as silver or lead. Traditional oil and/or grease lubrication cannot withstand the temperatures and vacuum requirements in the x-ray environment.

Silver is a face-centered cubic alloy which minimally work hardens; it acts as an elastic-perfectly plastic material. It is also electrically conductive [29]. During operation, the lubricant plastically deforms and flows across the ball and race surfaces to create a film. The film lubrication prevents direct ball-to-raceway contact, reducing friction, shear forces, and adhesive wear processes [29]. For the duration of this thesis, silver will be discussed and will be mentioned in conjunction with or in place of the phrase “solid lubrication”.

For purposes of vibration diagnostics of x-ray bearings, there are three things this work notes about solid lubrication:

1. Solid lubrication does not readily dampen vibration as does oil
2. The lack of damping creates more system-level vibration
3. Solid lubrication itself contributes to vibration

The intent of this work is to exploit the fact that oil is not present to dampen fundamental, characteristic vibrations [15]. It hypothesizes that the lack of oil creates a distinct advantage to machine condition monitoring because the lack of damping provides direct access to the fundamental bearing characteristic frequencies. Classical machine monitoring, almost exclusively done on production-type equipment with conventional (oil) bearings, is used to track generic broadband spectra amplitude changes and finally specific defects as the failure progresses towards incipient failure and end of life [8]. Bearings with solid lubrication exhibit distinct peaks early and throughout life will prove to be beneficial as a means to describe the bearing components at any given point in time.

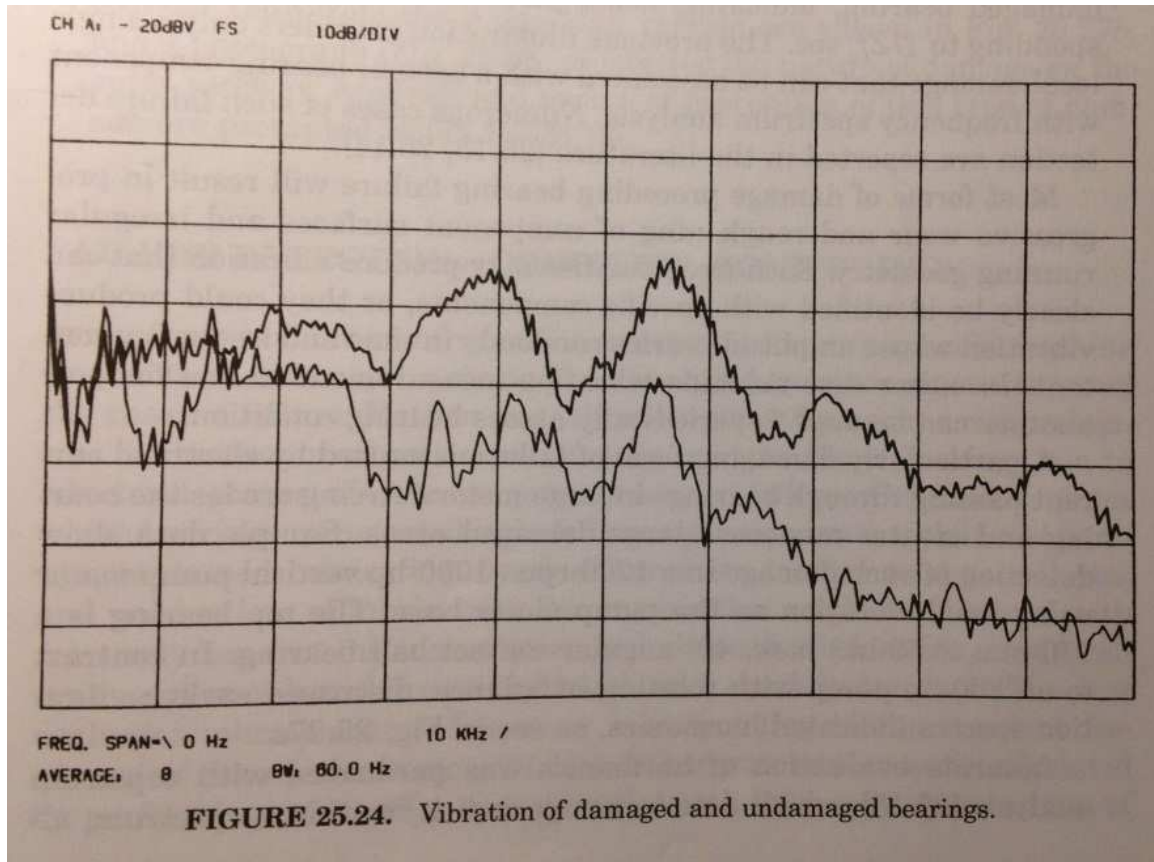


Figure 2.4: Damaged bearing spectrum compared to an undamaged bearing spectrum [15].

The figure above is spectra from an oil bearing. The upper line is the damaged bearing while the lower is the undamaged bearing. One can simply see an amplitude shift in this example of classical machine vibration monitoring. Note there are no distinct frequency peaks and the undamaged spectrum has nearly the same shape and pattern as the damaged bearing spectrum with higher magnitude. One can make high level assessments: the bearing is not in optimal operation as compared to the reference, undamaged bearing spectrum, because the vibration amplitude is higher. It is difficult and/or nearly impossible to describe the conditions of individual bearing components; the progression of failure is not far enough along to develop distinct peaks to give insight into the mode of failure (i.e. inner race defects, outer race defects,

ball defects etc.). However, as the failure progresses, only then will distinct frequencies have an opportunity to rise up out of the vibration floor as in the following figure:

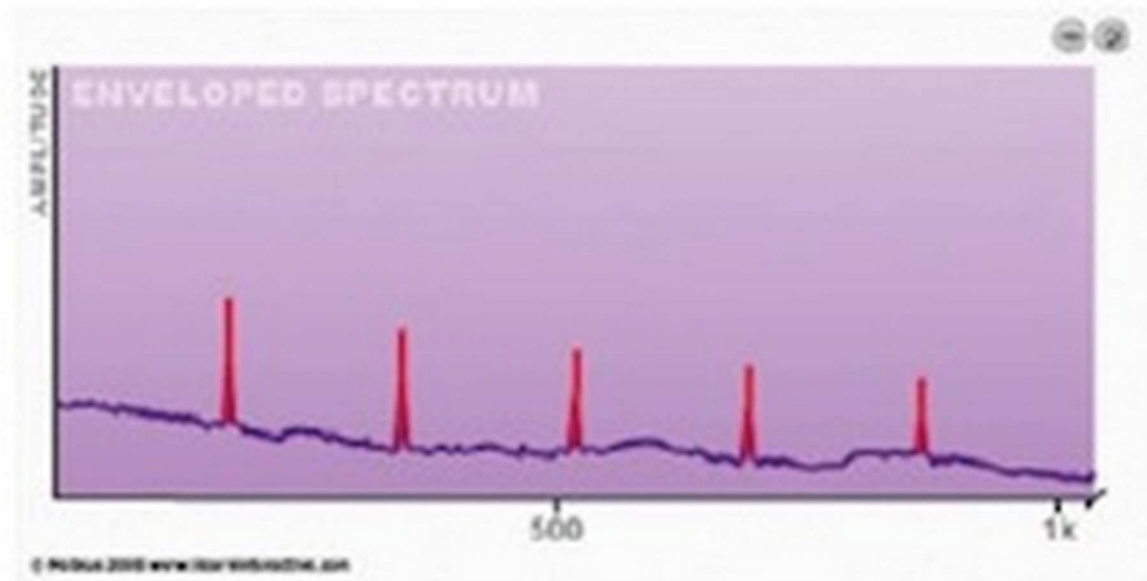


Figure 2.5: Peaks in failing bearing distinctly rising above the broadband noise [36].

The peaks in the figure above rise up out of the broadband floor, a high signal-to-noise ratio. They are specific to bearing defects and occur in oil bearings near imminent failure. On the other hand, x-ray bearings exhibit distinct peaks in this manner from day one, and throughout life, as opposed to at the end of life. It is at this point where this work departs from traditional machine monitoring. The fact that x-ray bearings utilize solid lubrication without the damping effects of oil allows the employment of characteristic frequency tracking, the central theme of this work. When component peaks are more readily available, from there so it flows a more complete description of the bearing. Theoretically, it is hypothesized that one can monitor bearing life, bearing run in, and create a method for which to compare design changes.

The following figure is an example of an x-ray bearing spectrum. The major difference that one notices is the large signal-to-noise ratio in the x-ray bearing spectrum as compared to the oil bearing. The vibration spectrum in x-ray bearings is not nearly as damped and the

characteristic operational frequencies of the bearing components easily cut through the broadband noise floor in the absence of oil.

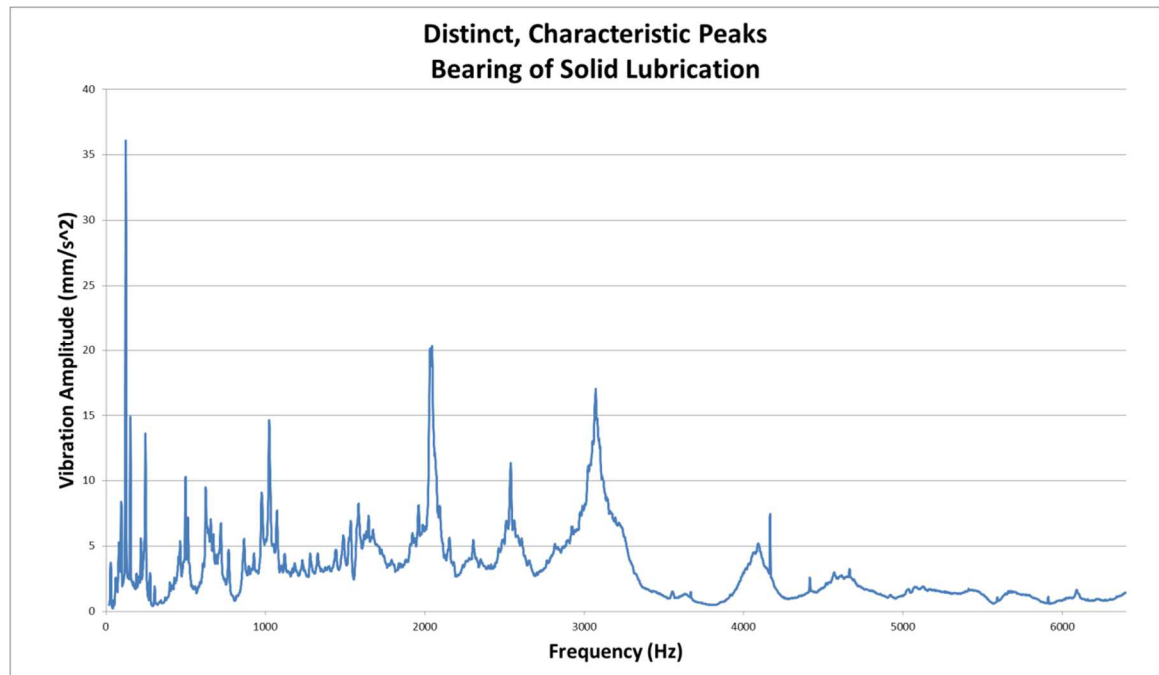


Figure 2.6: Example of distinct characteristic vibration peaks of an x-ray bearing spectrum.

X-ray bearings generally use two types of solid, pure elements as lubricants: lead or silver. The use of each is dictated by anode manufacturing processing and operational temperatures.

	Lead	Silver
Melting point	327C	962C

Table 2.1: Melting Point of Lead and Silver.

For the sake of discussion, let us assume silver is the primary lubricant, not lead. The silver must be mechanically spread across balls and bearing raceways to create a film of lubrication. Where possible or practical, the addition of thermal energy aids in the mechanical transfer because heat tends to increase malleability which helps to thin out the silver. The silver

transfer occurs some during anode processing and more so during bearing run in, a situation in which the bearing operates until it reaches an established steady state condition [29].

The difficulty and problem with using solid lubrication is achieving uniform application. Non-uniform lubrication is a source of vibration and noise (it should be noted that silver is not in liquid state during bearing operation). The silver will not move without ball interaction. The ball contacts the raceway in a very small elliptical area, especially compared to the potential area for the ball to roll within the area of the track. The small elliptical contact area essentially plows through the solid lubricant in the same way a sled or snowmobile cuts through fresh snow:

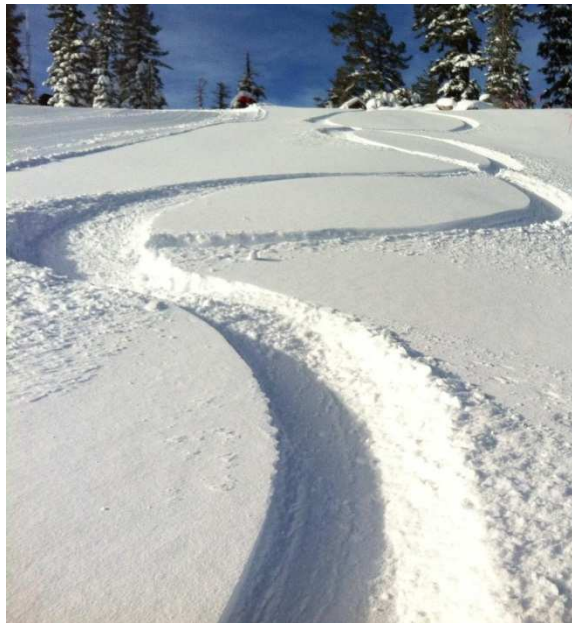


Figure 2.7: Tracks through fresh snow [36].

The ball contact area carries the load of the bearing and is on the order of 0.02mm^2 [15]. The small surface area creates a tremendous amount of stress which squeezes plastically deformed excess silver out of the ball path. As in the snow picture above, the center of the path flattens to some degree, but there are clear ridges off to the sides of the operation. As the ball continues to roll, both new and old areas receive attention from the ball's contact area. The

intent of bearing run in is to remove the excess lubricant (i.e. the ridges) to create a uniform film through repeated rolling and squeezing to reach a steady state operating condition [31].

As previously noted, one of the notes earlier about solid lubrication was that the lubrication itself contributes to vibration. Silver can become the surface irregularities that create frequencies of vibration modeled by the bearing characteristic frequencies equations. The irregularities include the aforementioned ridges as well as patches, or accumulation, of lubrication. The process of spreading silver and smoothing ridges is done over time, not instantaneously. Often, the path of the ball crosses itself, also illustrated in the snow picture. When this happens, the ball experiences a bump. If, for example, this was on the inner race, this bump would show up as an inner race vibration because solid lubricants have little means of reducing and/or controlling vibration of rolling elements or balls [15]. It is interesting to note that the non-uniform solid lubrication is measureable in the same fashion as a defect. Simply stated, one of the applications of this work will lay the foundation to track the efficacy of silver transfer and design iterations to promote silver transfer.

2.3.3 Bearing Design Geometry

It is prudent to understand the relationship between the design geometry, mechanical/thermal stress, and vibration. Presented are some of the main inputs and outputs expected during bearing design. These are the variables that can be tested in a bearing rig and monitored with the vibration technique designed in this thesis. This section is a design guide and is not presented with the intent to create an optimized design.

Note: All nomenclature taken from Harris's Rolling Bearing Analysis [15].

2.3.3.1 Design Input

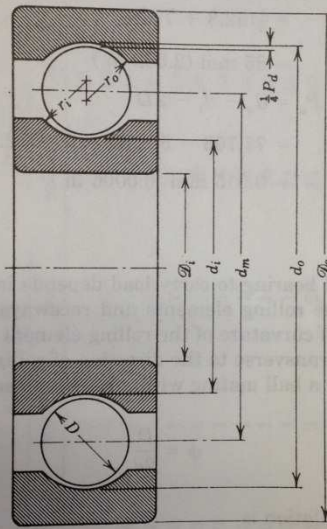
Description	Symbol	Schematic of select characteristics
1. Material a. Balls b. Races c. Lubricant d. Hub/flange	<i>N/A</i>	 <p data-bbox="925 1459 1445 1480">FIGURE 2.1. Radial ball bearing showing diametral clearance.</p> <p data-bbox="1153 1491 1209 1522">[15]</p>
2. Surface finish	<i>N/A</i>	
3. Lubrication thickness	<i>N/A</i>	
4. Ball diameter	<i>D</i>	
5. Number of balls	<i>Z</i>	
6. Inner race diameter	<i>d_i</i>	
7. Outer race diameter	<i>d_o</i>	
8. Inner race groove curvature	<i>r_i</i>	
9. Outer race groove curvature	<i>r_o</i>	

Table 2.2: Technical and dimensional characteristics of a bearing specified on a print [15].

2.3.3.2 Design Output

The design inputs have the following output relationships in a bearing:

Eqn.	Parameter/Variable	Description
Equation 2.1	$P_{max} = \frac{3Q_{max}}{2\pi ab}$	Maximum Hertzian contact pressure
Equation 2.2	$a = \left[\frac{6\hat{E}Q_{max}R_{eq}}{\pi KE_{eq}} \right]^{\frac{1}{3}}$	Major diameter of elliptical contact area
Equation 2.3	$b = \left[\frac{6K^2\hat{E}Q_{max}R_{eq}}{\pi E_{eq}} \right]^{\frac{1}{3}}$	Minor diameter of elliptical contact area
Equation 2.4	Combination of equations 1-3: $P_{max} = \frac{3Q_{max}}{2\pi ab} = \frac{3}{2} \left[\frac{Q_{max}E_{eq}^2}{36\pi KR_{eq}^2\hat{E}^2} \right]^{\frac{1}{3}}$	
Equation 2.5	$Q_{max} = \frac{5F_r}{Z\cos\alpha^o} + \frac{F_a}{Z\sin\alpha^o}$	Maximum normal load on race due to radial and axial loads
N/A	F_r	Radial load
N/A	F_a	Axial load
N/A	Z	Number of balls
Equation 2.6	$\alpha^o = \cos^{-1} \left(1 - \frac{P_d}{2A} \right)$	Free contact angle (rads)
Equation 2.7	$R_{eq} = \left[\frac{1}{R_x} + \frac{1}{R_y} \right]^{-1}$	Equivalent radius
Equation 2.8	$R_x = \left[\frac{1}{\frac{D}{2}} + \frac{1}{\frac{d_a}{2}} \right]^{-1}$	Equivalent radius in x-plane
Equation 2.9	$R_y = \left[\frac{1}{\frac{D}{2}} - \frac{1}{r_i} \right]^{-1}$	Equivalent radius in y-plane
Equation 2.10	Combinations of equations 2.7-2.9: $R_{eq} = \left[\frac{4}{D} + \frac{2}{d_o} - \frac{1}{r_i} \right]^{-1}$	
Equation 2.11	$A = (f_o + f_i - 1)D$	Distance between raceway groove curvature centers

Equation 2.12	$f_x = \frac{r_x}{D}$	Groove curvature ratio
Equation 2.13	$\hat{E} = 1 + \frac{\pi - 1}{\alpha_r}$	Unitless elastic modulus factor
Equation 2.14	$\alpha_r = \frac{R_y}{R_x}$	Equivalent radii ratio
Equation 2.15	$K = \alpha_r^{\frac{2}{\pi}}$	Unitless factor
Equation 2.16	$E_{eq} = \left[\frac{1}{2} \left(\frac{1 - v_1^2}{E_1} + \frac{1 - v_2^2}{E_2} \right) \right]^{-1}$	Equivalent modulus of elasticity
Equation 2.17	$d_m = \frac{1}{2}(d_i + d_o)$	Bearing pitch diameter
Equation 2.18	$P_d = d_i - d_o - 2D$	Bearing diametral/radial clearance
Equation 2.19	$P_e = 2A \sin \alpha^o$	Axial/end play
N/A	D	Ball diameter
N/A	ν	Poisson's ratio
N/A	r_i	Inner raceway curvature
N/A	d_o	Outer raceway diameter
N/A	d_i	Inner raceway diameter
Equation 2.20	$f_c = \frac{\omega_{rps}}{2} \left[1 - \frac{D}{d_m} \cos \alpha \right]$	Fundamental train (cage) frequency
Equation 2.21	$f_{bpir} = \frac{Z\omega_{rps}}{2} \left[1 + \frac{D}{d_m} \cos \alpha \right]$	Ball pass frequency of the inner race (inner race defect frequency)
Equation 2.22	$f_{bpor} = \frac{Z\omega_{rps}}{2} \left[1 - \frac{D}{d_m} \cos \alpha \right]$	Ball pass frequency of the outer race (outer race defect frequency)
Equation 2.23	$f_r = \frac{\omega_{rps}P_d}{2D} \left[1 - \left(\frac{D}{d_m} \right)^2 \cos^2 \alpha \right]$	Ball spin frequency
NA	ω_{rps}	Angular speed in rev/sec

Table 2.3: Bearing design equations [15, 17].

2.3.4 Application of Bearing Geometry

This section describes how design specifications impact the operation of a bearing. It elaborates on the mathematical relationships presented in the previous table and provides physical meanings to help the engineer during design work.

2.3.4.1 Groove Curvature

Groove curvature ratio, is a measure of how well the ball and race match.

$$f = \frac{r}{D}$$

Equation 2.24: Groove curvature ratio

If the race curvature and ball share the same magnitude radius, then the ratio would be 0.50, a perfect fit. In this instance, there would be no motion. The industry standard for angular contact ball bearings runs between 0.52-0.53, with 0.52 being the quoted nominal [15].

2.3.4.2 Radial and Axial Clearance

Clearance or play is the amount of movement allowable given the relative conformities of balls to raceways. There are two types of interdependent clearances in ball bearing design:

1. Diametral/Radial clearance
2. Axial clearance

The use of clearance is important in bearing design. It creates the bearing's ability to carry different types of loads and compensate for thermal growth. When subject to a thrust load, the axial play is removed and radial play is reduced. The diametral clearance allows the shaft to shift axially relative to a stationary outer race (thus taking up the axial play) [15].

$P_d = d_i - d_o - 2D$	$P_e = 2A \sin \alpha^o$	$A = (f_o + f_i - 1)D$
Equation 2.25: Diametral (radial) clearance	Equation 2.26: Axial play	Equation 2.27: Dist. between raceway groove curvature centers

2.3.4.3 Contact Angle

The clearance built into the unloaded bearing and the groove curvature ratios determine the contact angle. X-ray bearings utilize angular contact bearings to take on a combination of radial and axial loads during operation.

The radial play indirectly specifies the contact angle:

$$\alpha^\circ = \cos^{-1} \left(1 - \frac{P_d}{2A} \right)$$

Equation 2.28: Contact Angle.

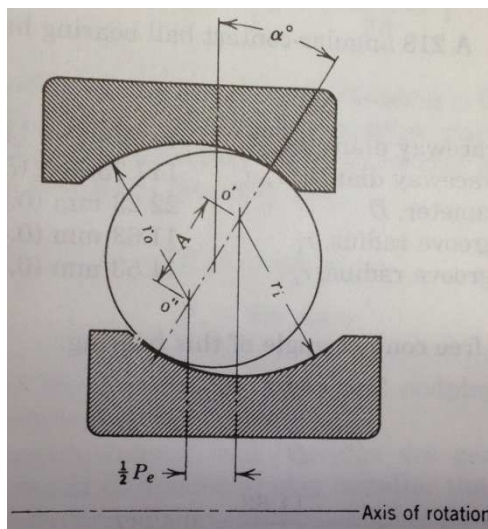


Figure 2.8: Cross-section of radial ball bearing with contact angle [15].

Typical contact angles in industry range from $10 - 45^\circ$. The larger the angle the larger the axial load supported but the smaller the radial load supported. The contact angle should be designed to match the relative proportions of each type of load expected during operation [15].

Additionally, thermal growth affects the contact angle. The material growth changes the proportions of the specified bearing components. These changes have to be taken into account for the use case to ensure the bearing operates as anticipated throughout all transient temperature differentials between components.

2.3.5 Thermal Compensation

Thermal compensation allows the bearing to continue to operate unimpeded after thermal growth. In other words, thermal compensation maintains sufficient clearance for operation during thermal growth [3]. In its crudest implementation, a thermally compensated design has the same clearance/play at operating temperature as it has at room temperature. A bearing will cease operation if the thermal growth reduces the residual radial clearance to zero. Negative clearance calculations indicate the parts will aggressively bind.

The target conducts heat through the shaft. The thermal energy then transfers to the balls, the outer races, and then the bearing housing. Thermal growth of the shaft occurs both in the radial and axial directions. What is not so obvious is the bearing-level effect: radial growth tends to squeeze the ball and reduce the contact angle; axial growth increases the contact angle and increases residual radial play. Correctly specifying clearances and contact angles will change together and balance these two competing mechanisms.

Foresight of thermal growth becomes difficult with the use of different materials with different coefficients of thermal expansion (CTE) and large temperature variations across each of the components. The x-ray tube manufacturer understands the thermal boundary conditions and is well versed in vacuum and high voltage technologies. Boundary conditions and heat transfer via radiation vary considerably in the vacuum environment of the x-ray tube. This makes it difficult to predict the amount of thermal energy getting to the bearing. The bearing itself is the largest thermal conduction path out of the vacuum, so thermal management with heat barriers and cooling methods become important in addition to the bearing design. The bearing supplier does not have control over this part of the upper-level assembly and therefore can never predict accurately the actual end use for a given x-ray tube design. This is another reason to optimize the method of testing designs through a DOE-type scenario in a bearing rig.

2.3.5.1 Contact Force, Area, and Stress

A free body diagram of a simply supported beam quantifies the radial loading imparted on bearing races:

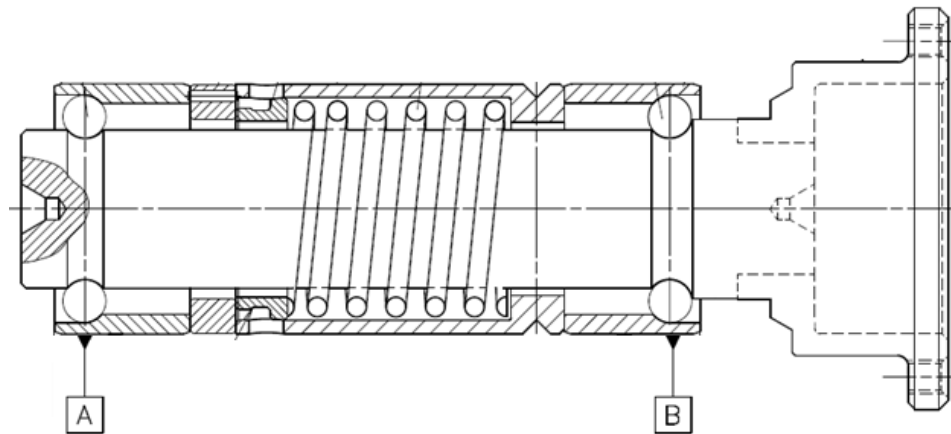


Figure 2.9: Reaction forces on bearings.

The reaction forces at A and B are considered separately during stress analysis. The positions each represent a different bearing.

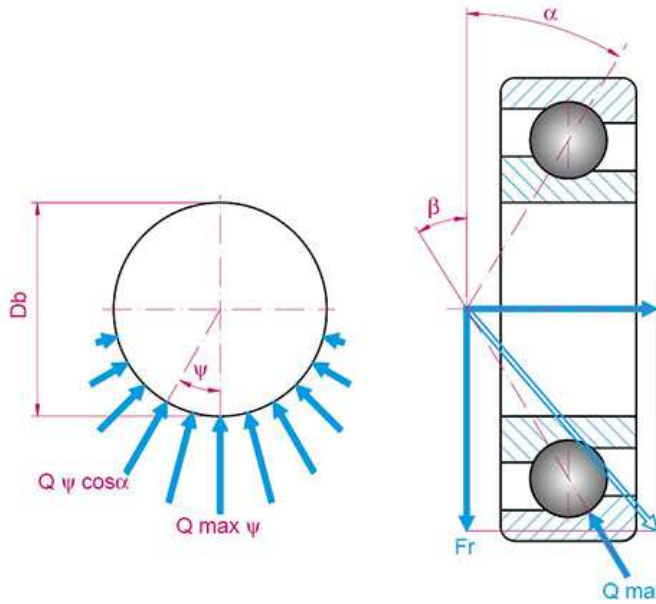


Figure 2.10: Shaft (inner race) load distribution [4].

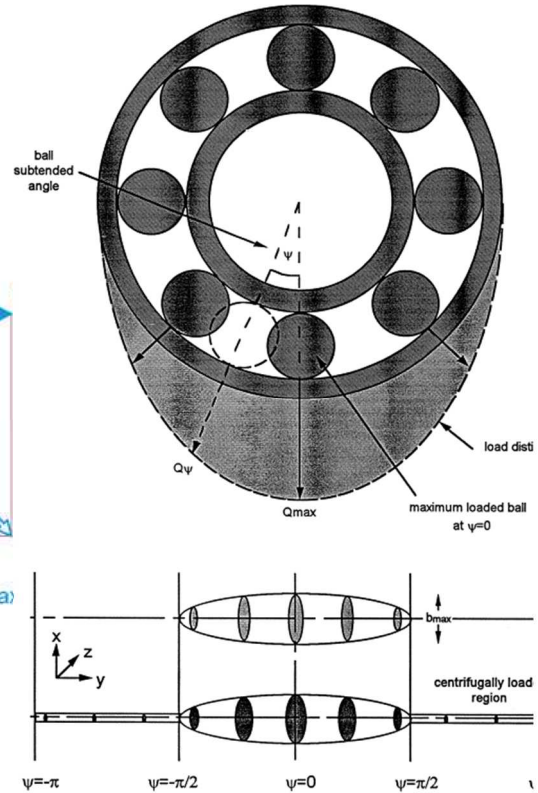


Figure 2.11: Ball load distribution [4].

$$Q_{max} = \frac{5F_r}{Z \cos \alpha^0} + \frac{F_a}{Z \sin \alpha^0}$$

Equation 2.29: Maximum normal load on race due to radial and axial loads

The total load is distributed along the bottom half of the shaft and is further distributed through the balls to the outer race. The maximum applied force Q_{max} occurs at the bottom dead center position of the ball train as shown in the graphics. Q_{max} is a normal force that is a function of both the axial and radial loads related through trigonometry of the contact angle.

The force on each individual ball is highly cyclical in nature. Obviously, the ball itself rotates. However, while the ball rotates the set of balls together rotates around the shaft. As the ball train moves around the shaft, each of the individual balls moves in and out of the load zone. The stress is cyclical because the balls see both maximum and minimum stress during the course of operation [13].

Contact mechanics is the study of deformation of solids as they come into contact with one another. The original work in the 1800’s, now known as Hertzian theory, is the fundamental basis for contact analysis in bearing design. Analysis becomes increasingly complex when friction and tangential shear forces are taken into account. For the sake of simplicity, this thesis will discuss Hertzian stresses on the surfaces of rolling contact transverse (normal) to the direction of rolling motion. The following assumptions exist in contact theory:

- The strains are small and within the elastic limit for the balls and races
- The area of contact is much smaller than the characteristic radius of the spheres in contact with one another
- The surfaces are continuous and non-conforming
- The surfaces are frictionless

In ball bearing analysis, when a spherical object meets another surface, the apparent area of contact is an ellipse as shown below in the figures.

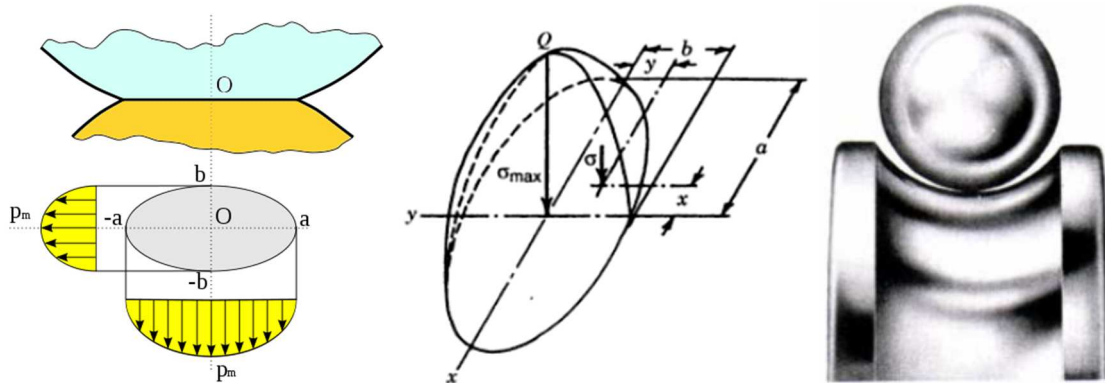


Figure 2.12: Elliptical stress distribution in point contact [4].

$a = \left[\frac{6\hat{E}Q_{max}R_{eq}}{\pi KE_{eq}} \right]^{\frac{1}{3}}$	$b = \left[\frac{6K^2\hat{E}Q_{max}R_{eq}}{\pi E_{eq}} \right]^{\frac{1}{3}}$
<p>Equation 2.30: Major diameter of elliptical contact area</p>	<p>Equation 2.31: Minor diameter of elliptical contact area</p>

Table 2.4: Calculations of the elliptical shape of the contact area.

Many technical specifications influence contact stress. This concept mindmap shows the conceptual and physical factors and interdependencies involved in designing to and calculating contact stress.

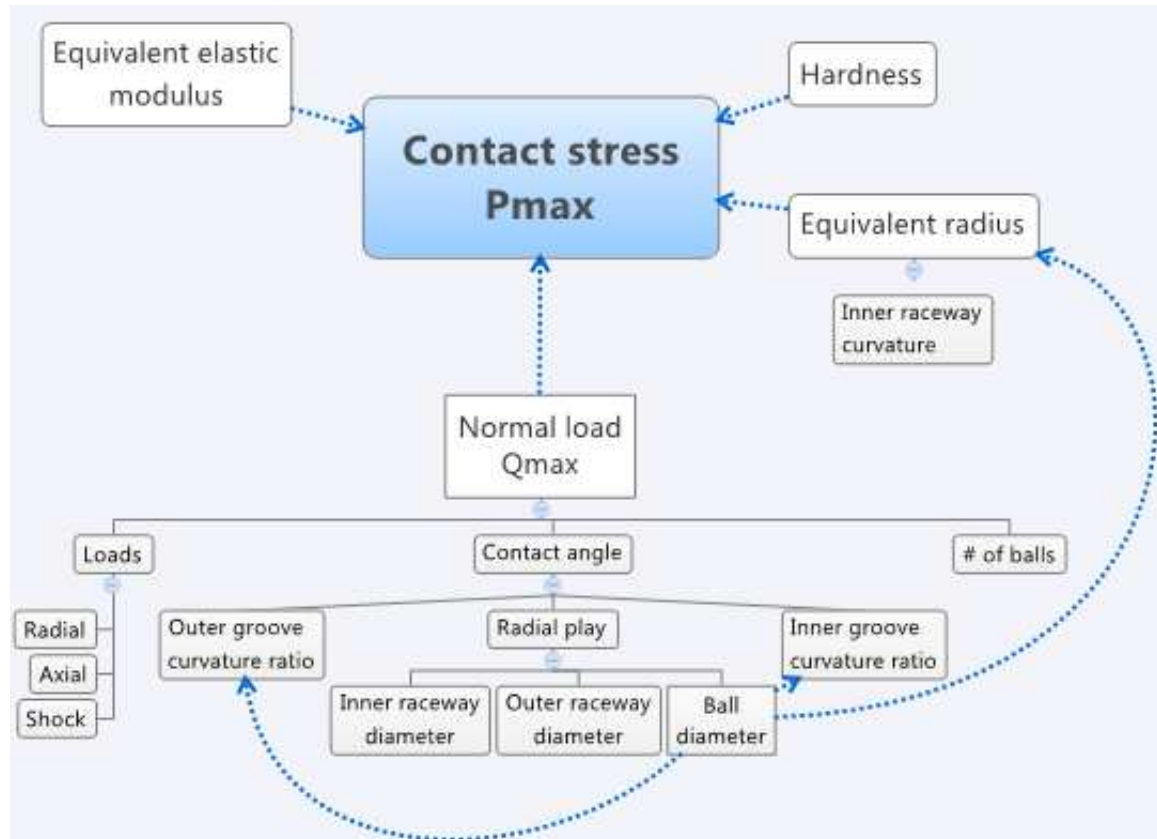


Figure 2.13: Bearing Equation Mind Map


Overall, the maximum contact stress is described in the following equation:

$$P_{max} = \frac{3Q_{max}}{2\pi ab} = \frac{3}{2} \left[\frac{Q_{max} E_{eq}^2}{36\pi K R_{eq}^2 \bar{E}^2} \right]^{\frac{1}{3}}$$

Equation 2.32: Maximum Hertzian contact pressure

The second equation of the maximum pressure is an expansion of the elliptical contact area to help emphasize that there are several non-dimensional factors and simplification parameters in the bearing equations. It is of particular interest to understand the ones with physical meaning

and how they relate to contact stress. For example, the equivalent radius R_{eq} and equivalent modulus of elasticity E_{eq} are simplifications that help guide the design stress to the most conservative number and reduce interactions of design variables in the analysis [17].

$R_x = \left[\frac{1}{\frac{D}{2}} + \frac{1}{\frac{d_0}{2}} \right]^{-1}$	$R_y = \left[\frac{1}{\frac{D}{2}} - \frac{1}{r_i} \right]^{-1}$		$R_{eq} = \left[\frac{1}{R_x} + \frac{1}{R_y} \right]^{-1}$
Equation 2.33: Equivalent radius in x-plane	Equation 2.34: Equivalent radius in y-plane		Equation 2.35: Equivalent radius

$$E_{eq} = \left[\frac{1}{2} \left(\frac{1 - \nu_1^2}{E_1} + \frac{1 - \nu_2^2}{E_2} \right) \right]$$

Equation 2.36: Equivalent modulus of elasticity

The contact stress equations suggest concepts that are perhaps counter-intuitive to general practice. That is, to minimize contact stress through material selection, one would want to choose materials with low moduli of elasticity as emphasized in the equation. A lower modulus of elasticity involved would reduce contact stress because the material would yield more easily, dramatically increasing the contact area. Thus, for a given load applied, the resulting stress significantly reduces with the increase in the surface area as the material yields more readily.

In practice, quite the opposite approach is taken. Materials of high moduli of elasticity are chosen to avoid permanent deformation. As a frame of reference, aluminum is about 68GPa whereas bearing tool steels are 200+GPa with hardness above 60HRC. Large values of elastic moduli and hardness resist damage and wear quite well. These characteristics increase contact stress by resisting elastic yield which reduces contact area [16].

2.4 Bearing Characteristic Frequencies

This section is a discussion around how bearing geometry drives specific frequencies.

The concepts presented here establish the relationship between geometry, fundamental bearing theory, and empirical vibration data. Characteristic frequencies of the bearing describe the:

- Ball/cage train (fundamental train)
- Inner race
- Outer race
- Ball spin

Balls roll in and out of the load zone under elastic deformation. Each ball takes turns in carrying the load. Due to elastic compliance, the balls act as springs to produce relative motion between the inner and outer ring. The motions of the races are described by the natural frequencies, the fundamental frequencies, of the bearing.

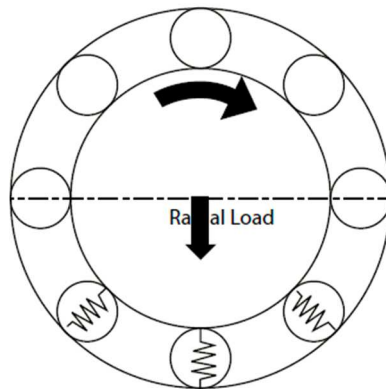


Figure 2.14: Elastic compliance of ball bearing [19].

The situation of elastic motion is an artifact of the nature of the design. It will always be present to some degree. However, in addition to this “natural” phenomenon of the bearing, the same frequencies arise due to mechanical defects on the components. The characteristic frequencies are in fact defect frequencies that define the condition of the components by the magnitude of the associated vibration. This concept is verified when a defect is intentionally

imparted upon a bearing component. The vibration frequencies manifest themselves when a defect is intentionally put on a bearing component. For example, when a single defect is located on the outer race, the bearing will exhibit a vibration due to this imperfection. One can calculate the outer race defect frequency, damage the outer race, and then proceed to measure the bearing's vibratory response. Take the following graphic as an extension to the aforementioned defect in the outer race:



Figure 2.15: Outer race defect [37]

The discrete defect, shown as a red dot at the bottom dead center position of the outer race, produces a shockwave each time a single ball passes over it. The shockwave sends a pulse of energy that ripples through the structure, causing resonance and vibration [38]. The following equation describes the theoretical frequency (the outer race "defect" frequency) one would detect with measurement equipment, assuming a stationary outer race and rotating inner race:

$$f_{bpor} = \frac{Z\omega_{rps}}{2} \left[1 - \frac{D}{d_m} \cos \alpha \right]$$

Equation 2.37: Outer race defect frequency

Likewise, discrete defects for the inner race and ball can be described as follows:

$$f_{bpir} = \frac{Z\omega_{rps}}{2} \left[1 + \frac{D}{d_m} \cos \alpha \right]$$

Equation 2.38: Inner race defect frequency

$$f_r = \frac{\omega_{rps} P_d}{2D} \left[1 - \left(\frac{D}{d_m} \right)^2 \cos^2 \alpha \right]$$

Equation 2.39: Ball spin frequency

It should be noted that the detectable ball defect occurs at $2xf_r$. f_r alone is the ball spin frequency. The ball defect frequency occurs when the area of interest on the ball hits both the inner and outer races within one full ball revolution, hence two times f_r [19].

Another characteristic is the fundamental train, or cage, frequency (FTF):

$$f_c = FTF = \frac{\omega_{rps}}{2} \left[1 - \frac{D}{d_m} \cos \alpha \right]$$

Equation 2.40: Fundamental train frequency

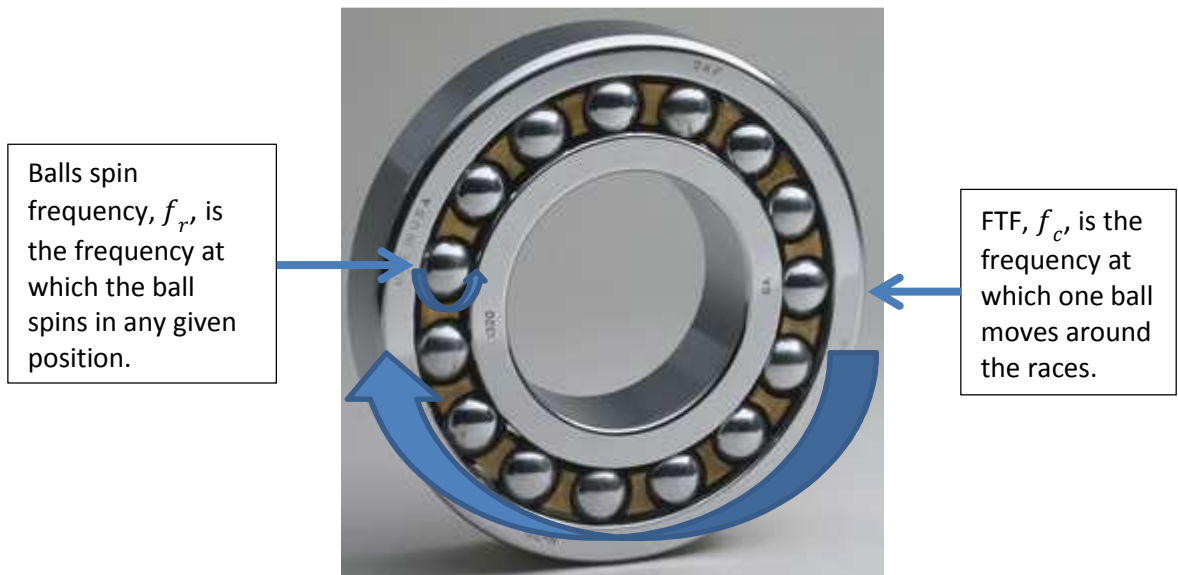


Figure 2.16: SKF ball bearing.

The fundamental train frequency (FTF) is the rate at which the entire set of balls makes one revolution around the shaft. The cage frequency is analogous to the earth making one full revolution around the sun (a year) while still spinning on its own axis. This is also the same phenomenon that creates cyclical stress on each of the balls.

The fundamental train frequency often creates sidebands around other frequencies. The presence of these FTF sidebands often indicates ball problems [37]. The subject of sidebands is somewhat abstract. It is difficult to conceptually visualize or relate to prior experiences in life. It is, however, a phenomenon of bearing operation, as well as an identifying characteristic. Sidebands are symmetrically spaced peaks about a carrier frequency signal (generally denoted by the largest, and also center, peak of the spectrum of interest). Consider the following:

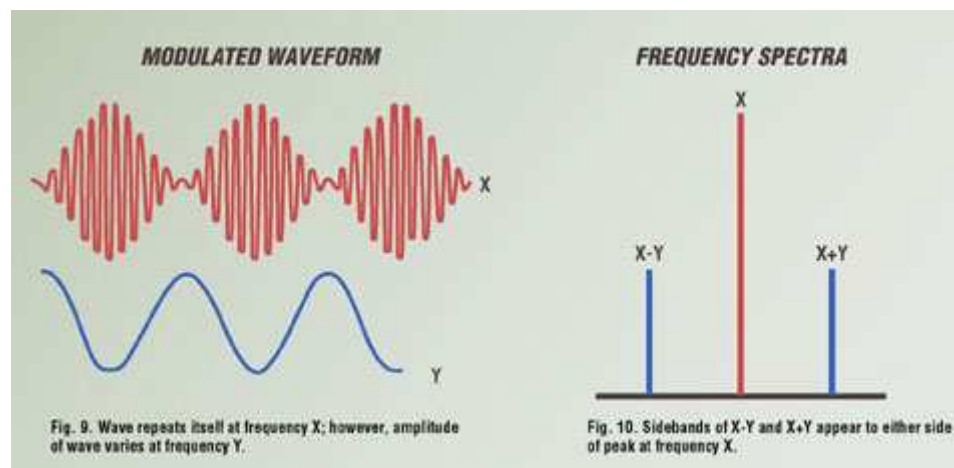


Figure 2.17: Amplitude modulation and sidebands [10].

The carrier frequency “X” changes amplitude periodically due to frequency “Y”. The frequency “Y” is the amplitude modulator and represents how the amplitude changes in time [10]. This concept is applied to AM radio signals, Amplitude Modulated frequencies.

Sidebands and amplitude modulation occur in bearing vibration analysis. In the instance that the defect is not on a stationary component, the defect will enter and leave the load zone. The energy due to the vibration shockwaves will increase as the defect approaches the load zone, finally peaking at that load zone. Subsequently, the vibration amplitude will decrease as the defect leaves the load zone [19].

If sidebands exist at the rate the shaft turns, one can suspect an inner race fault. When FTF sidebands occur, there may be a fault with the balls [37]. In the instance of a defect on a stationary component, like the outer race of a bearing with an internally rotating shaft, amplitude modulation will not occur. The loading on the stationary outer race will not change. On the other hand, as previously noted, a defect on a rotating shaft will see a varying load and produce peaks with modulated amplitudes.

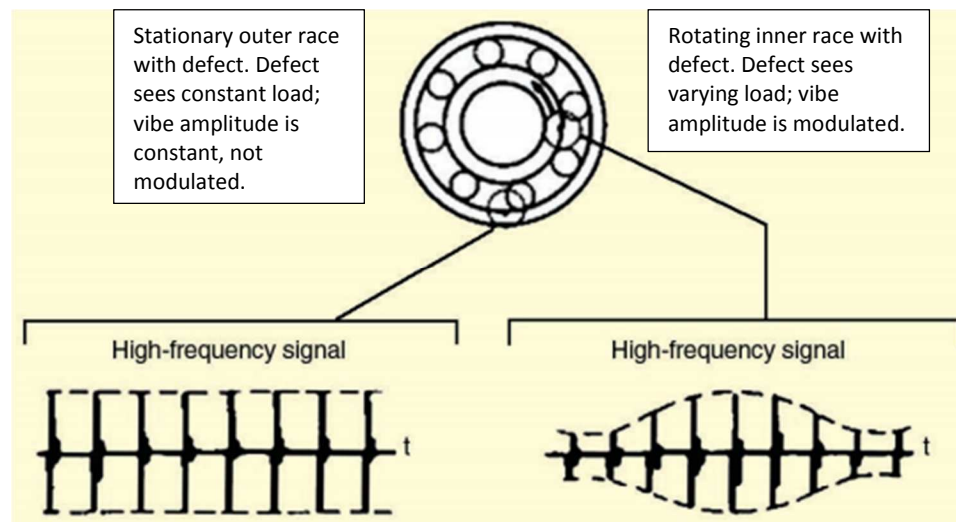


Figure 2.18: Amplitude modulated sidebands [18].

Regardless of the source of the defect, be it of inner race, outer race, or ball origination, the local fault's impact frequency and its harmonics create a signal that will be affected by the system. The transmission path of the characteristic frequencies may be diminished by damping or amplified by structural resonances. In other words, the defect impact frequency harmonics influence the system response and increase vibration amplitude in the event the harmonics align with natural frequencies in the system [18].

3 Data Collection Procedures

This section provides the background and methodology to collect data to test the premise of this thesis. The following block diagram will be described throughout this section:

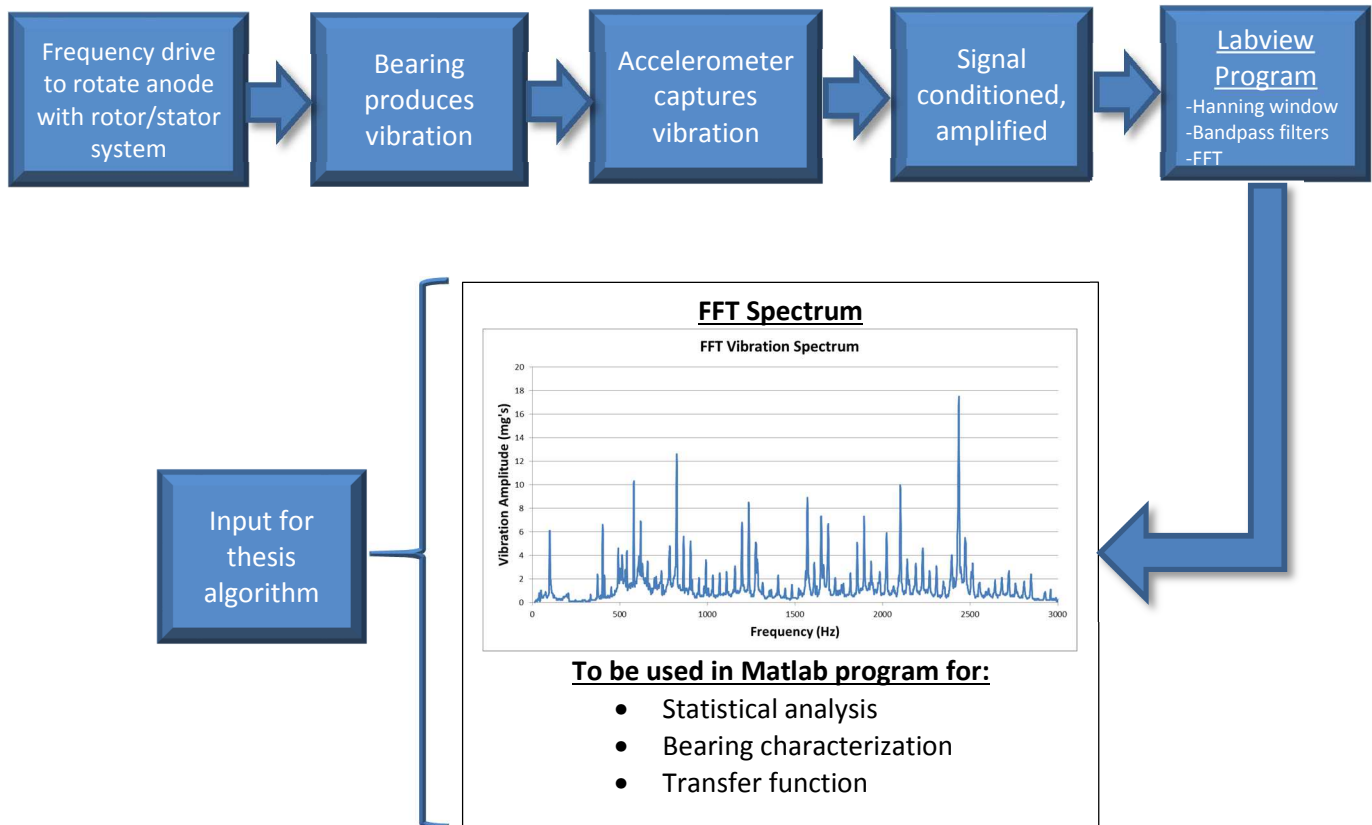


Figure 3.1: Block diagram of data collection procedures.

The data collection process is a variation of conventional machine condition monitoring techniques. A frequency drive rotates the bearing/anode assembly. Vibration is measured with an accelerometer. The signal flows through a conditioning amplifier prior to being collected in a Lab View program for post-measurement processing, including a Fast Fourier Transform (FFT). The FFT spectral data is the input into this thesis at hand and the input into the Matlab algorithm to extract descriptive statistics of a ball bearing in operation. The analytical work against the theory starts with the vibration FFT spectra.

3.1 Bearing Assemblies Under Test

A single bearing assembly is actually composed of two bearings. The following is a picture of the bearing assembly under test in this thesis.



Figure 3.2: Bearing assembly under test.

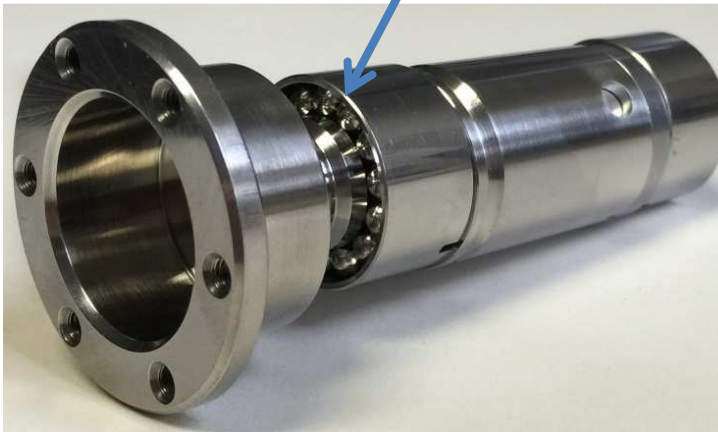


Figure 3.3: One of two bearings in bearing assembly.

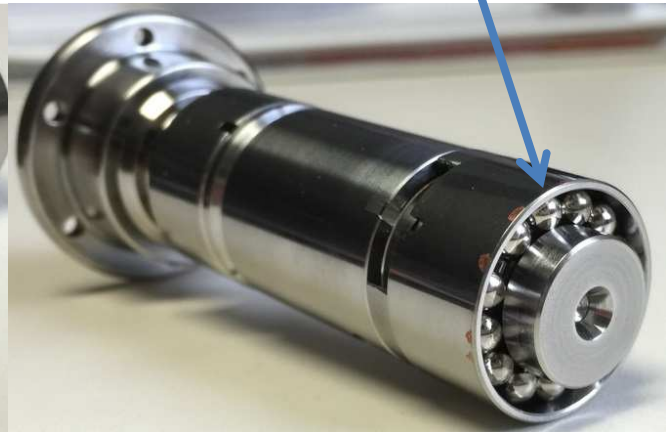


Figure 3.4: Two of two bearings in bearing assembly.

The presence and simultaneous operation of both bearings pose some risk to the accuracy of the analysis. It is not possible to differentiate between the two in the vibration signature. The accelerometer is placed well outside of the bearing housing which means the vibration produced from either of the bearings travel through the system together. It would be ideal to have one accelerometer for each end of the assembly, but accelerometers physically will not fit during operation.

The risk posed to the analysis occurs because each bearing may have slightly different geometry which would yield slightly different resonant frequencies. The differences may be on the order of less than 10Hz. For analytical purposes, the geometrical dissimilarities are accounted for during the vibration peak review. The characteristic peak is sought within a range of frequencies dependent upon possible component size combinations. If there are in fact two unique peaks within the tolerance range of the expected peak, the highest vibration peak will be taken to describe that particular type of characteristic frequency. This is the most conservative approach when describing the condition of the bearing because the largest amplitude represents the worst-case component condition.

The bearing assembly resides in the following anode sub-assembly:

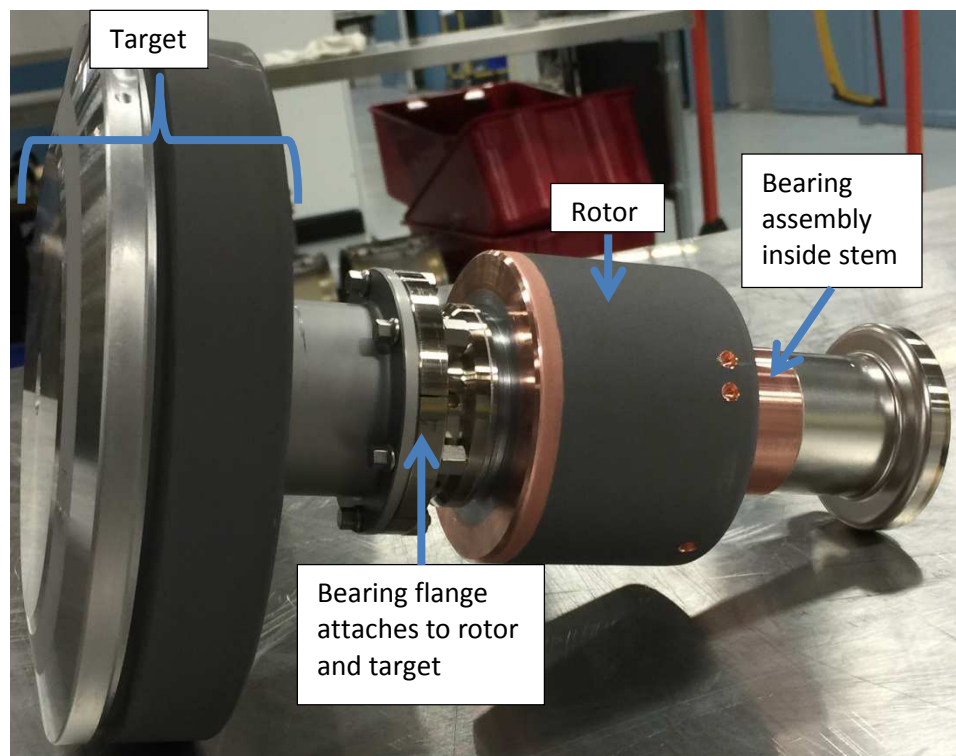


Figure 3.5: Anode assembly under test.

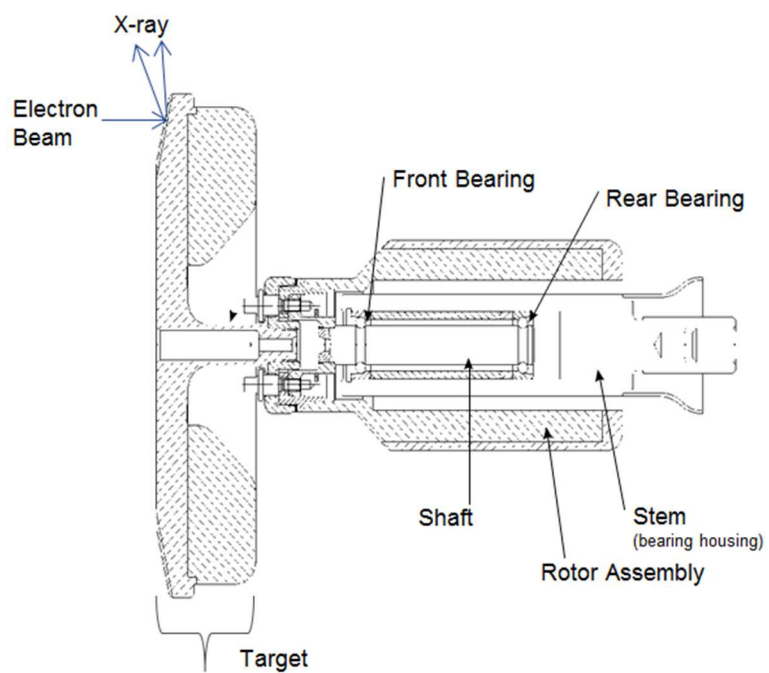


Figure 3.6: Cross-section of anode assembly.

3.2 Test Platforms

There are two platforms in which to gather data for a transfer function: one at the full casing level of the x-ray tube, the other at the anode level in a bearing rig. The manipulation of the data to create the transfer function between the two systems is in the results section.



Figure 3.7: Full casing-level x-ray tube.

Above is the full casing-level platform. The x-ray bearing in the anode assembly is located on the right hand side as indicated. This platform was already well-established and in operation prior to the work of this thesis and will not be thoroughly discussed.

The bearing rig was created for this thesis to develop the transfer function against the already existing casing-level platform. The design of the rig had the following goals:

1. Simulate the casing-level assembly
2. Simulate an x-ray environment
3. Provide a stable, structurally sound platform from which to repeatedly gather vibration data
4. Standardize the vibration data gathering technique
5. Promote reusability for multiple tests

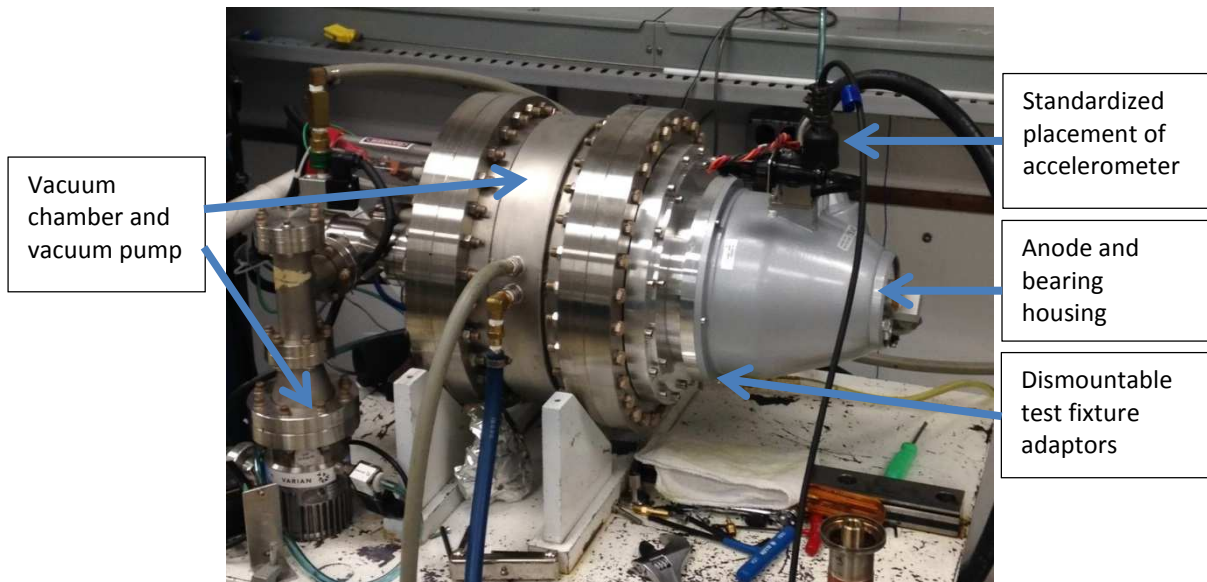


Figure 3.8: Bearing test rig platform.

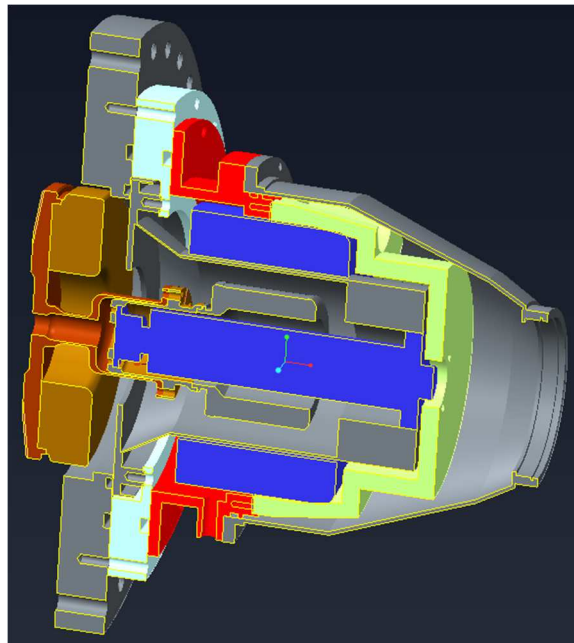


Figure 3.9: Cross-section of anode-end of bearing rig design.

The most essential output is the acceleration (vibration) data collected from the rotating bearing. The bearing rig standardizes the data collection by providing a dedicated structural stiffness and a dedicated mounting location for the vibration accelerometer.

The rig fixtures impact the vibration measurement. It may dampen or amplify the characteristic vibration frequencies under test. The impacts on the vibration output are known as “system interactions” and their impact will not be constant between test setups if not properly controlled. The energy dissipation through the structure changes due to the stiffness of the structure [47]. To limit the variance of system interaction between tests, system interaction will be taken into account by controlling the structural stiffness of the rig through standardized torques and assembly procedures.

Conceptually, all structures are linear elastic and are described through simple harmonic motion: a mass-spring-damper system.

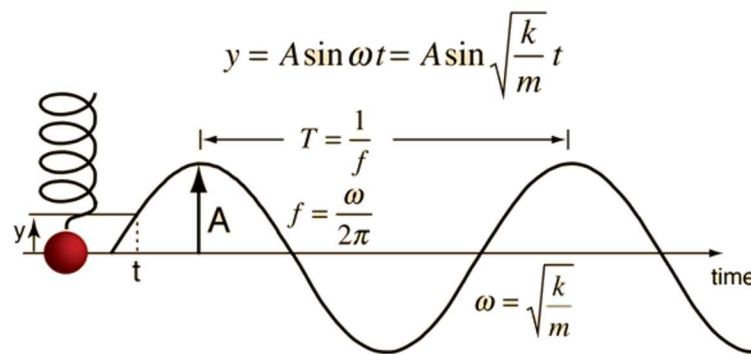


Figure 3.10: Diagram of simple harmonic motion [33].

The mass m and the spring constant k define the sine wave response of the system given an input force. The natural frequency of the system is ω , which specifically means the system’s response, is related to both the mass and spring constant of the structure under test. This implies that if the bearing rig mass doesn’t change, the only factor left to influence system response is the spring constant.

Similar to the diagram above, structures like a bridge or a bearing rig, have a mass and spring constant. The spring constant in a structure is very large, rendering the structure more

“solid” than “springy”. All structures do have some spring to them. A rigid structure’s frequency response behavior is defined by its associated mass and spring constant in the same manner as the ball-spring diagram. Therefore, the concept of simple harmonic motion emphatically creates the need to control the mass and spring constant of the rig if there is to be a predefined, expected response out of the bearing rig system. In other words, for practical application, when the bearing rig is used as a test platform, the bearing vibration is under test, not the system’s impact on the bearing. Bearing vibration is the variable; the test structure and the “ k ” must be held constant to control variation (i.e. gage error) between tests.

The structural stiffness is controlled by standardizing the assembly procedure. The applied torque to the bolted joints provides and determines the structural stiffness [47]. The bolted joints of the bearing rig use a calibrated torque wrench and follow a set of procedures to tighten to the same torque every time. The bolts are incrementally torqued in a star-shaped pattern to evenly distribute the preload and prevent warping or fastener binding of any given fixture.

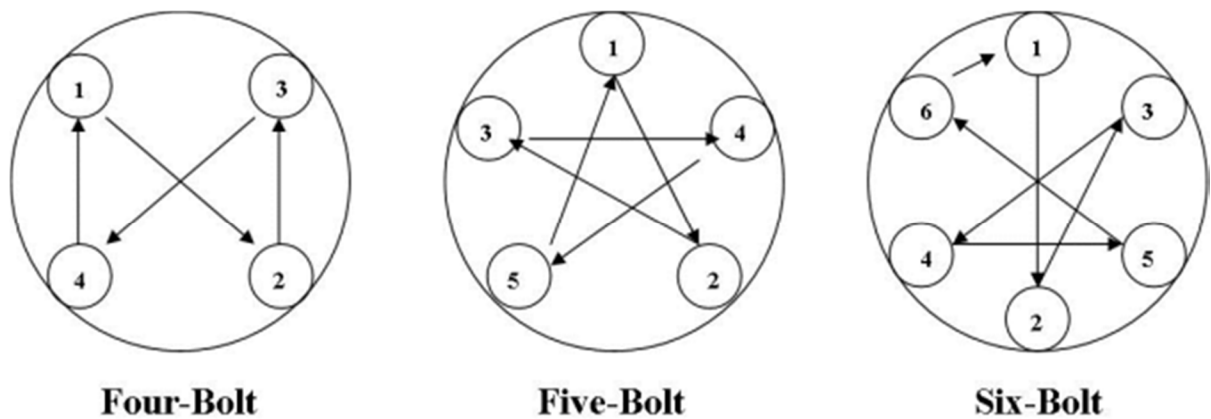


Figure 3.11: Examples of different methods torque star-patterns [7].

As a final note on structure, ideally, the system interactions should not have any natural frequencies that overwhelm the bearing vibration spectrum. This would render the test setup unusable because one would not be able to delineate the bearing frequencies of interest under the mask of system interaction. The exact value of the stiffness of the structure does not have to be calculated, but the stiffness should be repeatable from measurement to measurement as defined through standardized torque procedures.

3.3 Raw Data Collection: Vibration Measurements and Frequency Transformation

Vibration can be measured in terms of acceleration, velocity, or displacement. In this case, acceleration is the measurement of choice. “The nature of mechanical systems is such that appreciable displacements only occur at low frequencies, therefore displacement measurements are of limited value in the general study of mechanical vibration,” [22]. The piezoelectric accelerometer has a very good dynamic range and great sensitivity, which means it measures signals of both high and low amplitude accurately. Acceleration is generally/informally accepted as industry standard and was thus employed instead of velocity for the vibration acquisition and subsequent analysis of this work [22]. Therefore, acceleration is the measurement method used for this bearing study.

The transfer function sought is between the casing-level and the bearing rig sub-assembly level with the following conceptual procedure. Vibration will be measured from a single anode assembly at the casing level. The casing is disassembled to retrieve the anode assembly. The same anode assembly (and thus the same bearing) is loaded into the bearing rig. Vibration is then measured on the bearing rig. The results from each test of the same bearing will be compared against one another to create a single, bearing-specific transfer function between the two test platforms. The process is repeated ten times for ten different bearing casing/rig relations.

A calibrated accelerometer is strategically placed to maximize the potential of obtaining meaningful data. It is located transverse to the axis of rotation and picks up radial acceleration of the rotating mass.

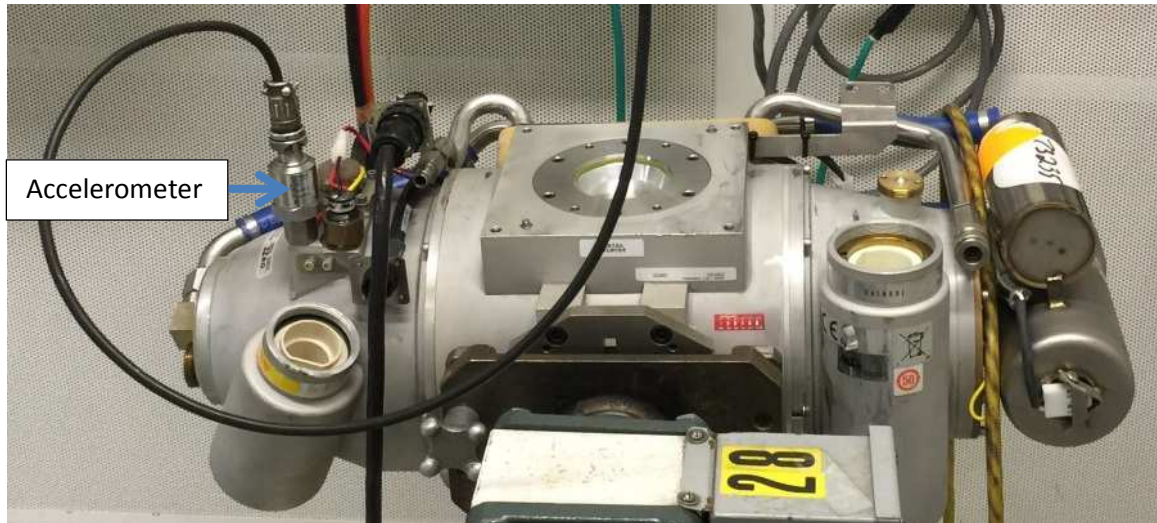


Figure 3.12: Accelerometer placement on x-ray tube casing.

It is mounted using a stud on the flat surface of the fixture to help standardize the data acquisition process and reduce variations in the frequency response of the accelerometer. As an example, B&K provides a diagram of the effectiveness of stud-mounting the accelerometer:

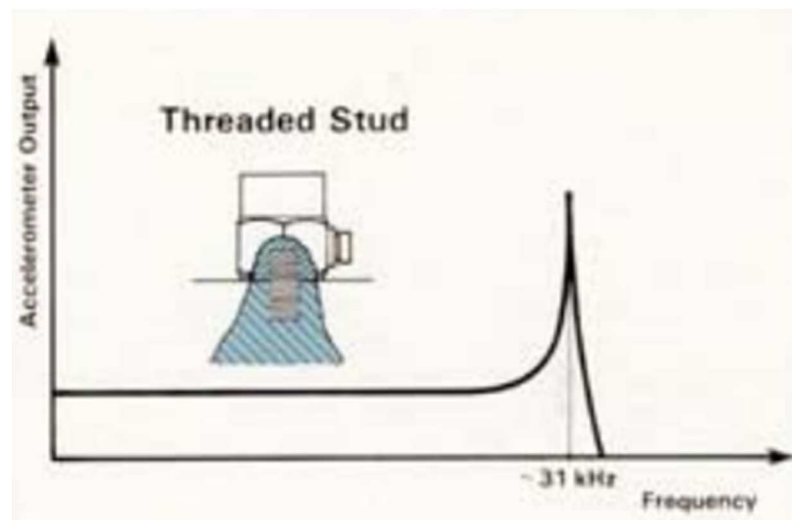


Figure 3.13: Accelerometer system response [22].

It is desired that the accelerometer operate in a linear range well below its natural frequency. That is, the frequencies of interest taken off the bearing rig should be low enough to avoid any potential interaction of the accelerometer.

The data signal from the accelerometer is in the time domain. The data presented in this manner is noticeably noisy, unclear, and seemingly random:

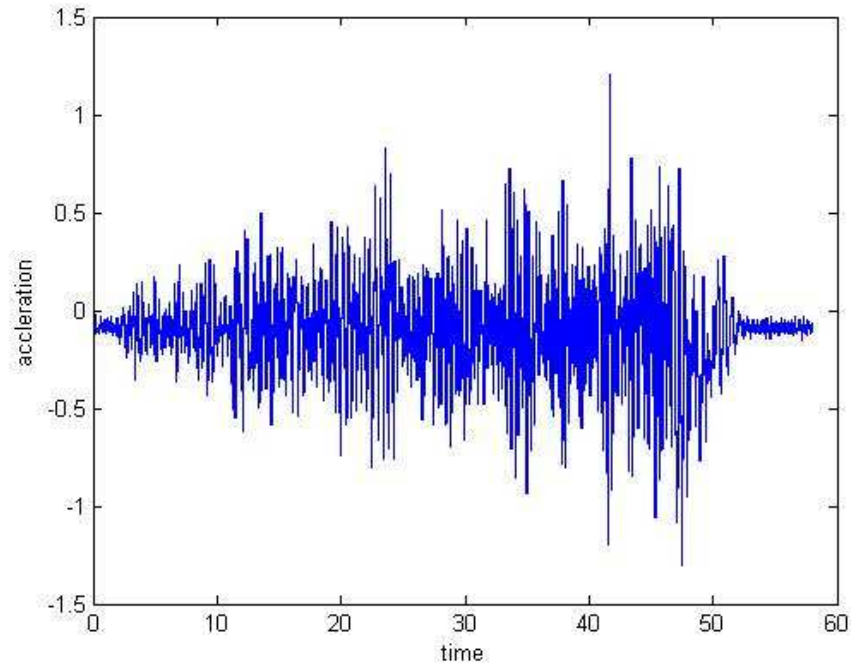


Figure 3.14: Vibration in time series [26].

Conceptually, the diagram above is exactly what is done when measuring the vibration of a bearing: the operator installs the accelerometer onto the bearing rig, runs the bearing, and collects data over time. There are literally thousands of frequencies represented in a single superposition-type plot such as this. Therefore, this signal is fed into a conditioning amplifier and a lab view program for post processing. The program performs a Fast Fourier Transform (FFT) to differentiate between frequencies and associated magnitudes. The following diagram graphically explains the FFT.

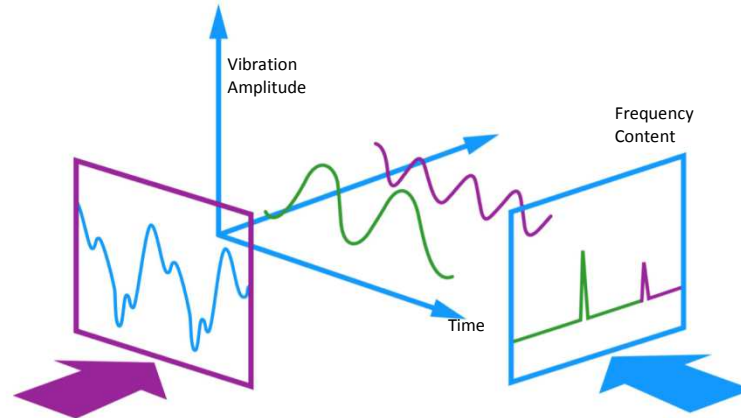


Figure 3.15: Synopsis of Fast Fourier Transform [27].

The figure outlined on the rectangle on the left-hand side of the diagram represents the overall signal of measured frequency amplitude over time. Looking through it to the three axes, one can see that it is made up of two separate frequency signals: the overall signal in the left rectangle is the superimposition of all contributing signals. The three axes represent time, magnitude, and each of the two frequencies that contribute to the whole. When this data set is viewed through the figure outlined in blue (the rectangle on the right-hand side of the diagram), there are two distinct peaks. This view is a representation of the Fast Fourier Transform of the frequency vs. time signal represented in the left-hand side spectrum.

The FFT transforms the signal from the time domain into the frequency domain. In this case of frequency of vibration analysis, this is most important because it allows one to focus on the magnitudes of vibration at any given frequency. In other words, it is used to find the frequency components of a signal in a noisy time domain dataset.

The nature of the FFT can sometimes corrupt the original signal data. However, with appropriate filtering techniques, such as windowing and averaging, one can minimize these effects. The transform occurs at a discrete set of frequencies from a time-domain waveform sampled at discrete times over a finite interval of time [43]. The FFT creates bins of data in

which it calculates the vector sum of all signal components. These bins are not frequency selective, which means data can overlap from one bin to the next.

The acquisition of the vibration data occurs over a finite amount of time even though the frequencies imparted by the bearing components are periodic. The finite time frame may cut off the vibration signal in the middle of period, resulting in a waveform that doesn't truly represent any physical phenomena. The extra wave forms on the side of the signal are called spectral leakage [43].

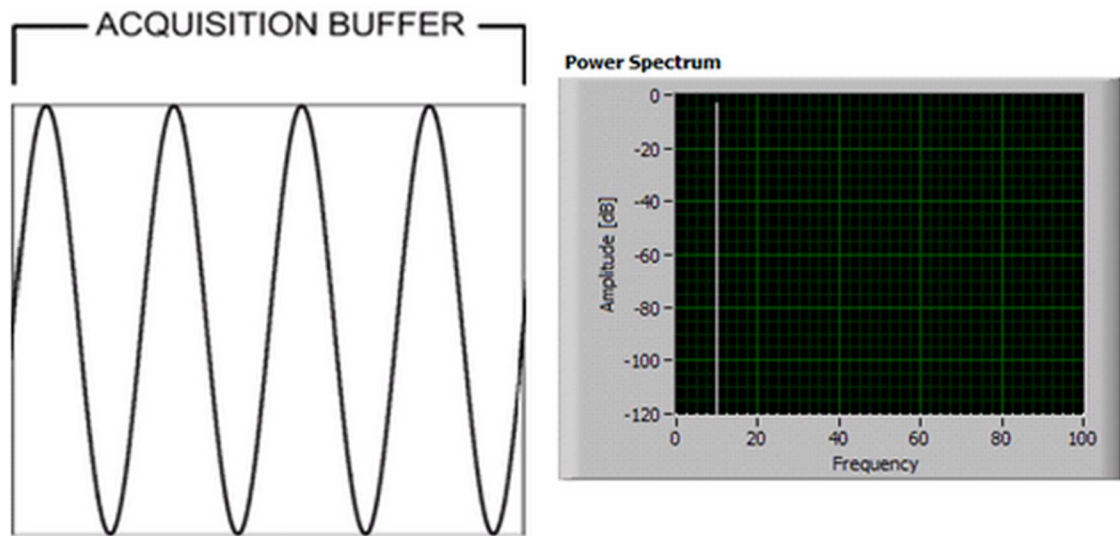


Figure 3.16: Measuring an integer number of periods gives an ideal FFT [43].

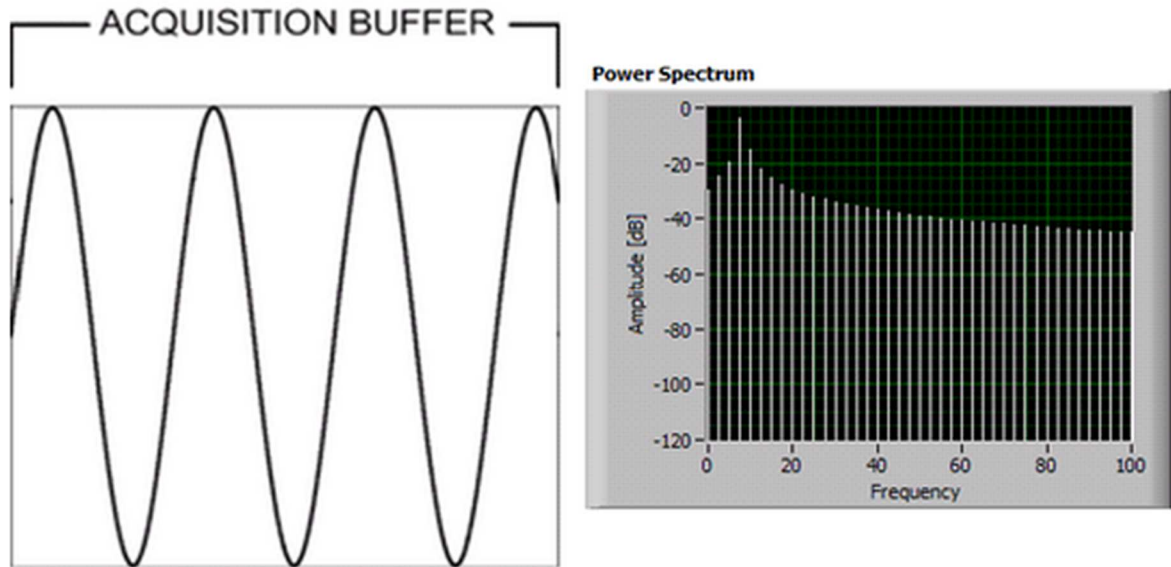


Figure 3.17: Measuring a non-integer number of periods adds spectral leakage to the FFT [43].

The vibration data acquired in this thesis uses a window function to reduce the presence of spectral leakage artifacts illustrated above in the figures. The window function is a signal multiplier used to force the data signal to start and end at zero regardless of the signal being acquired. In doing so, the truncation with a finite time data collection is avoided [14].

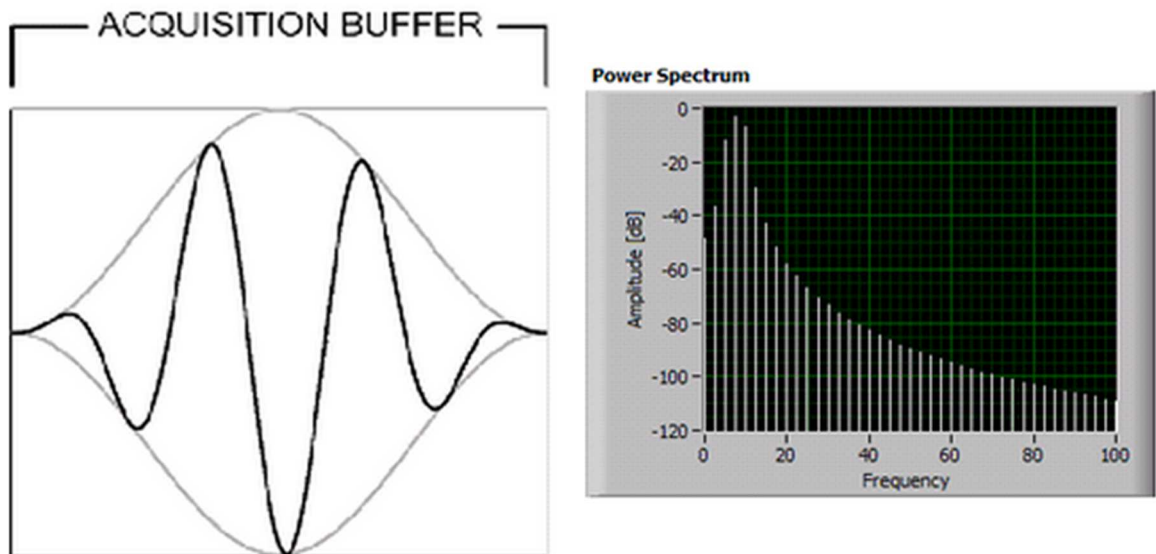


Figure 3.18: Applying a window minimizes the effect of spectral leakage [43].

The window function applied to the vibration signal for this thesis was a Hanning window at 1.3333Hz. This type of window is best suited for random noise vibration. This is appropriate because of the large number of different signals available in the frequency domain; the Hanning window has high resolution compared to other types of window functions available.

Additionally, it should be noted that the use of the window has its drawbacks. Machine vibration (i.e. bearing vibration) is not perfectly smooth. The transient nature of vibration taken over a finite amount of time subjected to a window function can result in extreme data values. The values can either be much smaller or larger than actuality. Therefore, to increase the quality of the data taken in this thesis, each data point in the FFT is the result 15 linear averages.

3.4 Procedures Used for Development of Matlab Model

The logic put forth will help to understand the thought process and validity of the approach to extract meaningful vibration amplitude distributions from spectral FFT data of bearing characteristic frequencies using a Matlab program. It should again be noted that each individual FFT data point taken is a 15 second linear average prior to being subjected to the analytics of this work. It is shown that, despite the averaging techniques used to create the initial FFT spectrum, subsequent data points still create a distribution due to the random nature of vibration, creating the need to statistically describe populations of vibration amplitudes on a per frequency basis.

Initially, Microsoft Excel is used as a basis to understand the vibration signatures from the test platforms. It is a quick method to manually review FFT spectra datasets and visualize how amplitude varies from measurement to measurement and bearing to bearing. The observations from Excel developed the forethought for the Matlab program designed to extract vibration amplitudes at specific theoretical frequencies. Excel is a powerful tool, but Matlab handles vast amounts of data in an automated manner. So, from a high-level, Excel was a proving ground and manual check point during the analytical development of the Matlab script designed to run as an automated workhorse to review populations of data on a large scale. The Matlab script, however, would not be viable without the physical understanding of the bearing vibration provided by manually executing analyses through Excel.

3.4.1 Initial Data Review: Microsoft Excel

Theoretical characteristic frequencies derived from bearing geometry and rotation speed are first explicitly modeled in Microsoft Excel. The bearing design discussion established in the literature review stood as an efficient checklist. The spreadsheet served as a look-up-table, the base for which all the analytical modeling and data capture would rest. The look-up-table consisted of the resonant frequencies and harmonics directly attributed to the geometry of the bearing and an assumed runspeed.

It is crucially important to understand the physics of bearing operation and its impact on vibration spectra. Excel provides that platform. The FFT spectra created during vibration data collection is fed into spreadsheets and quickly plotted. Plotting the data in Excel gives one the ability to get a “feel” for the data by manually correlating spikes with calculated frequencies in the look-up-table. This concept is a derivative of the fact that visual learning is a powerful technique, and played to the idea that “the human mind is one of the most powerful pattern recognition machines” [5]. One cannot simply create a method of analysis without first being a part of the analysis.

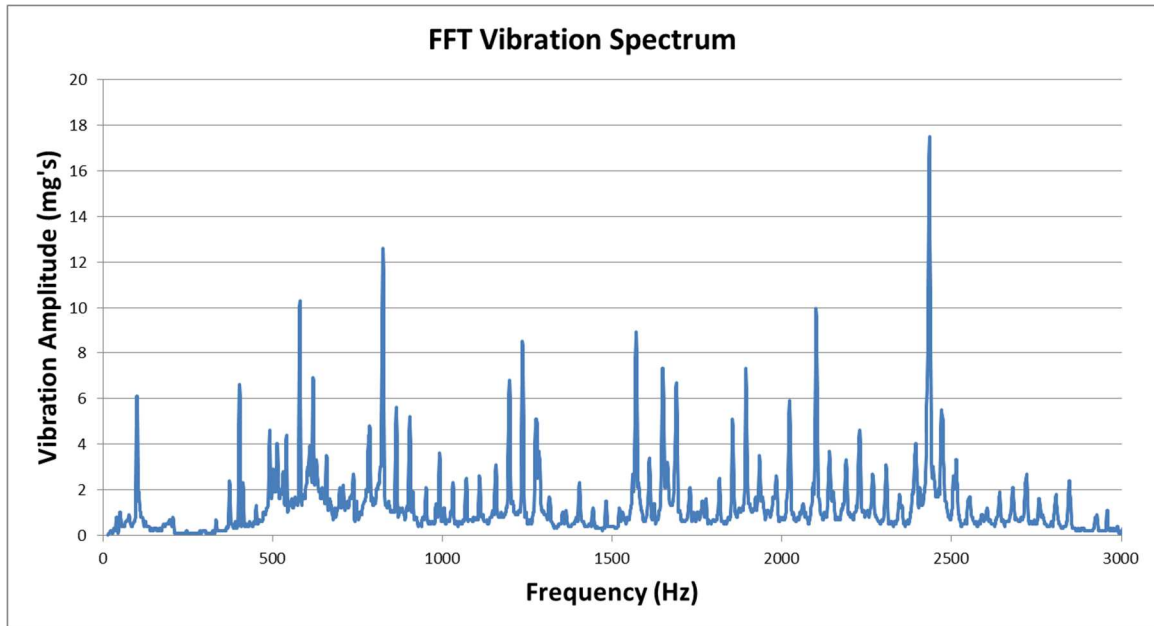


Figure 3.19: Example of FFT spectral data from test procedures.

The graph above is an example of a Fast Fourier Transform vibration spectrum plotted in Excel. From this one can provide justification to move forward with the hypothesis. The work is worth pursuing because the spikes indicate rather discrete frequencies emerge from the floor of the broadband noise during bearing operation. Directly, these spikes provide more information than would normally be available in broadband noise often found in the routine machine condition monitoring with oil bearings. On the other hand, if the spectrum looked like broadband noise, the analytics moving forward would be less promising if not impossible.

As an example to the point that the FFT spectra contained useful data, consider the following: the bearing under test has a theoretical inner race defect frequency at 789Hz. The following three figures, which are three measurements from one bearing, indicate vibration quite near 789Hz. The fact that a vibration peak is in the vicinity of the theoretical frequency allows one to assume the peak represents theory.

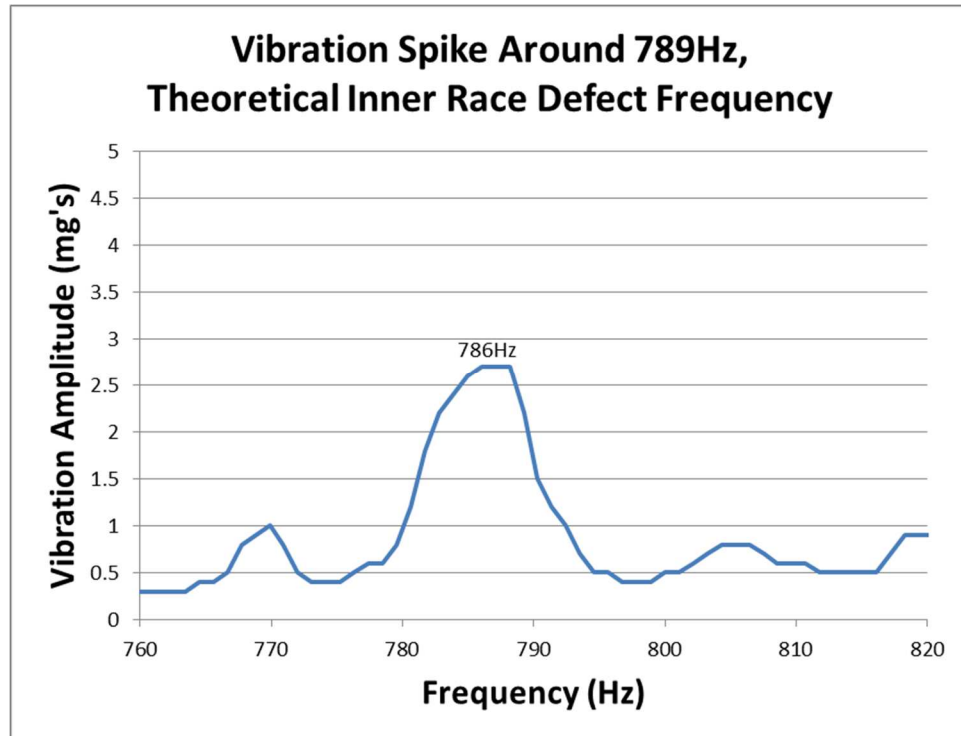


Figure 3.20: Bearing 1, Measurement 1: 786Hz.

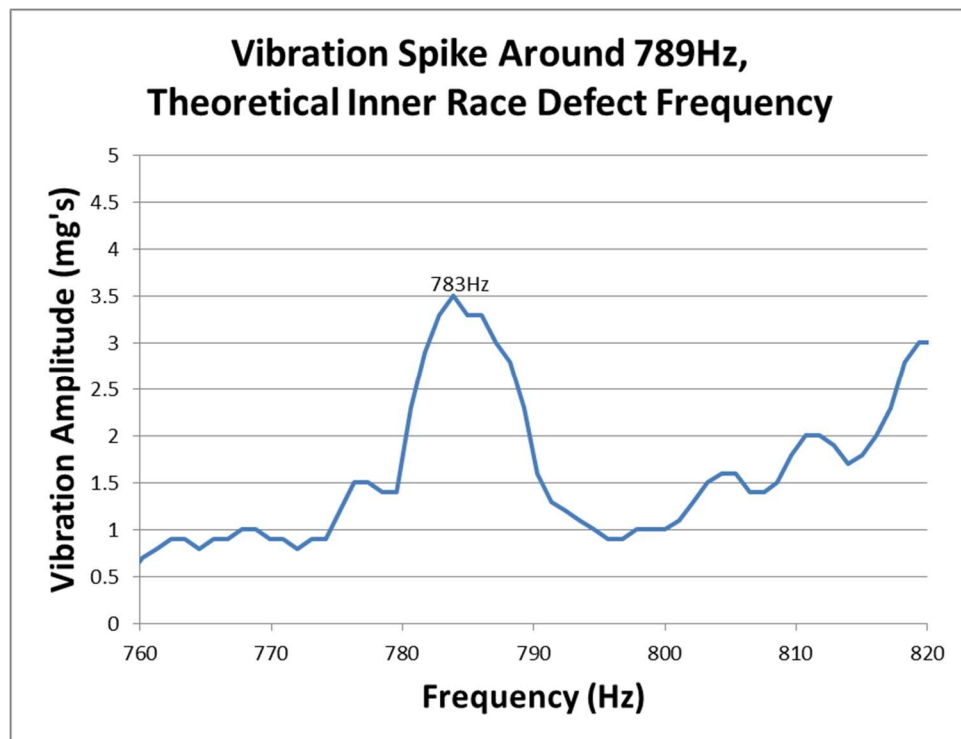


Figure 3.21: Bearing 1, Measurement 2: 783Hz.

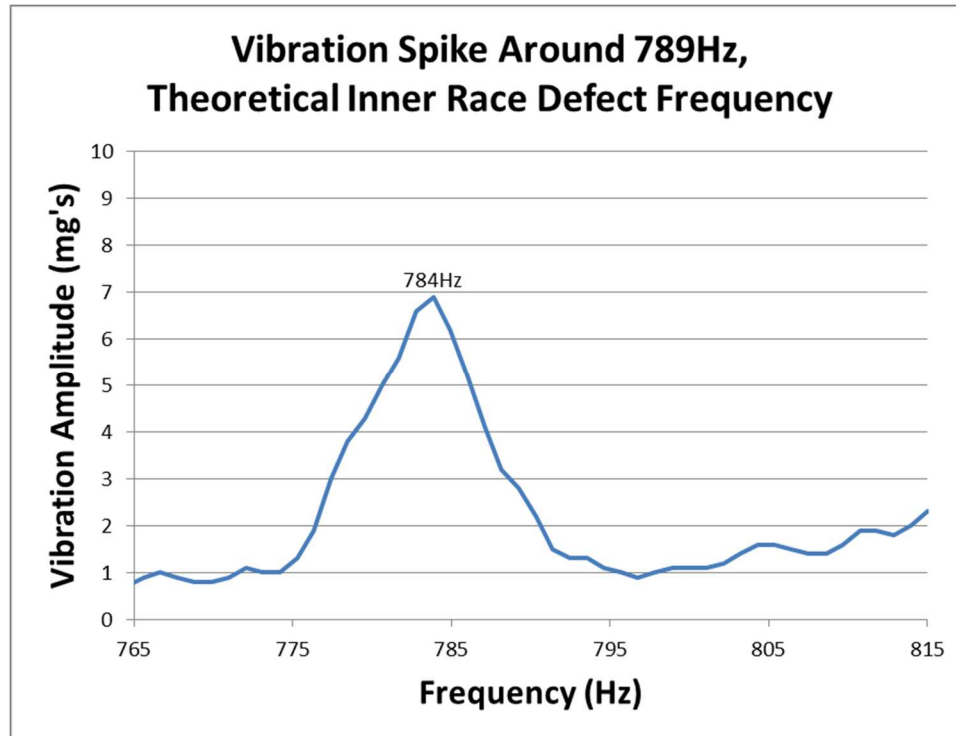


Figure 3.22: Bearing 1, Measurement 3: 784Hz.

3.4.2 Data Observations

Excel and the manual review process, such as the observations made with the 789Hz inner race frequency previously presented, brought to light several observations that drove a need for model refinement. Several things were noted while manually reviewing the data:

1. The spikes in each of the FFT spectra repeatedly indicated that useful information rose out of the broadband background noise typically found when monitoring machines using conventional bearings.
2. The manual use of a cursor and a look-up-table to review the more prominent spikes for comparison against theory repeatedly indicated the presence of correlations between datasets and bearings
 - a. This observation is powerful because it lends itself to creating an automated analysis
3. The presence of two distributions emerged:
 - a. The amplitude of vibration had a distribution at any given empirical frequency
 - b. The empirical frequency had a distribution around any given theoretical frequency

The scenario noted in “3” above means that there is both a distribution for the empirical characteristic frequency as well as the amplitude of the vibration at that frequency. This is seen in the three snapshots of the inner race frequency presented in Figures 3.20-3.22. The two distributions are reasons why manually walking through the data is important to understanding the physics of the bearing. It shows data collected may be inconsistent. If it is possible for vibration spikes to show up with great accuracy in some datasets but not others, more investigation is necessary.

The nature of the data invokes questions into the physics of bearing operation. What causes drift in measurements of a single bearing? What causes drift in measurements between bearings? The Matlab code must be robust enough to handle multiple variations and account for the realities of change. The two questions alone highlighted the realization that theories are based upon assumptions. When those assumptions are understood, a more powerful analytical

Matlab script handled the variations upended in the manual studies. There are two major assumptions used in the manual walk through of the data in Excel:

1. The components of the bearing are at their respective nominal dimensions
2. The rotation speed of the bearing is constant

The assumptions directly impacted the values of the theoretical characteristic frequencies that populated the spreadsheet look-up-table for comparison against the empirical vibration frequencies. The repeatability and accuracy of matching theory with practice rested on fine tuning the assumptions to match reality.

3.4.3 Model Refinement: Monte Carlo Simulation

Departures from nominal dimensions partially explain the observed distribution of vibration frequencies around the theoretical frequency. This concept is modeled using a Monte Carlo simulation. “Monte Carlo simulation is a method for exploring the sensitivity of a complex system by varying parameters within statistical constraints,” [24].

Any process, any part, any action always exists with some departure from nominal, or the expected value. It is not possible to create components that are all the same size every time. Therefore, it is conventional to apply tolerance zones around a desired value to account for and accept manufacturing deviation. When several components come together, each component has its own variation. The deviation of all the parts combined is called a tolerance stackup. The tolerance stackup affects the operation of the assembly and must be taken into account when assigning individual tolerances per component. The Monte Carlo simulation method is a means to understand and statistically quantify the tolerance stackup of the whole assembly and the sensitivity any one component has on the whole. In the case of bearing operations, the interest lies in the effect the variation of the components has on the calculation of the theoretical frequencies.

Generally, it is common to assume a normal distribution of values between the upper and lower control limits. However, where possible, the known distribution of measured values within the tolerance zone should be used. Monte Carlo uses the probability distribution of each component to create a probability of the tolerance stackup by performing random trials. The computer randomly grabs values within the given distribution of each component and applies the values to the frequency equation to create a final distribution output. In the case presented below, the inner race defect frequency is made up of 50,000 trials. Each trial consists of taking one point from each of the component distributions to put into the frequency equation.

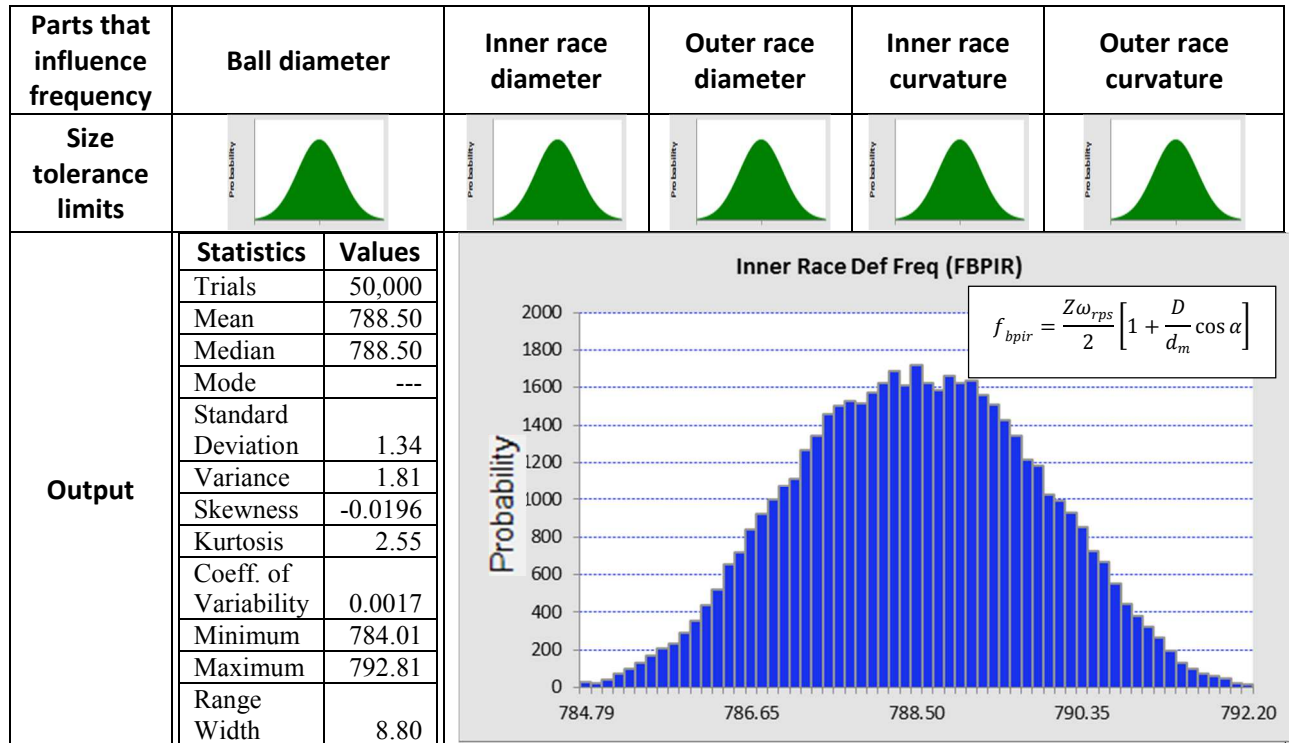


Table 3.1: Monte Carlo simulation of inner race defect frequency due to component tolerance stackup.

The distribution in Table 3.1 is the probability density function of the inner race defect frequency due to tolerance stackup of all components and assumes a constant runspeed of 100Hz. The resonant theoretical frequency is centered around ~788.5Hz. As one can see, the variation in components themselves creates a distribution between 785Hz and 792Hz. Therefore, the conclusion of the Monte Carlo simulation states that tolerance stackup causes a 4Hz departure from the theoretically nominal resonant inner race frequency.

Additionally, there is a second contributor to departure from nominal resonant frequencies. Any frequency of interest in the FFT data set is directly proportional to the runspeed of the shaft. The expected frequency changes based upon the rotor speed (bearing speed), making the analysis quite dynamic. It is seen that variations in runspeed quite significantly account for the distribution of vibration frequencies around the theoretical frequency.

To review the impact, the runspeed is tracked. The runspeed creates a distinct vibration spike on the FFT plot. It is known with certainty that the spike is due to the rotation speed of the bearing by varying the frequency drive and tracking the movement of the spike; there is a 1:1 correlation. For all data in this thesis, the bearing assemblies are controlled by a frequency drive set to rotate the anode at 100Hz (6000RPM).

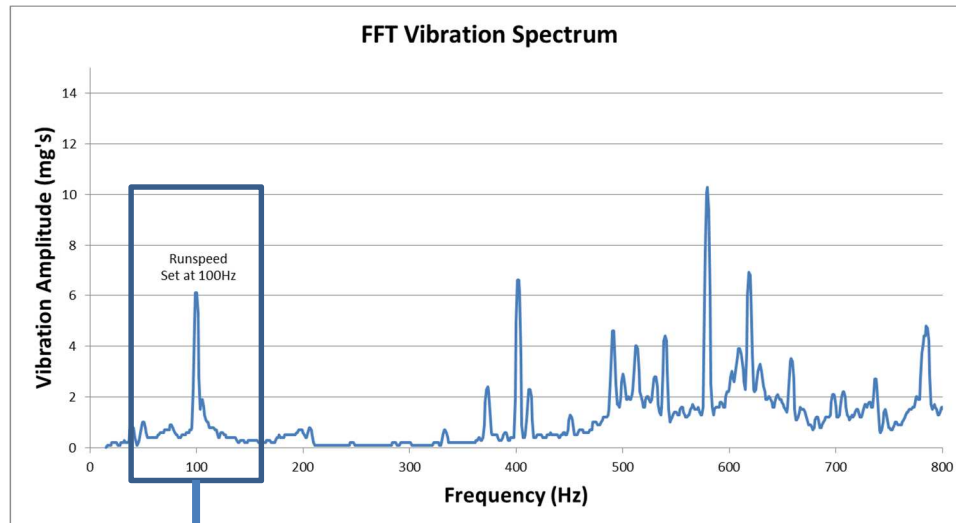


Figure 3.23: Vibration spectrum indicating runspeed vibration peak.

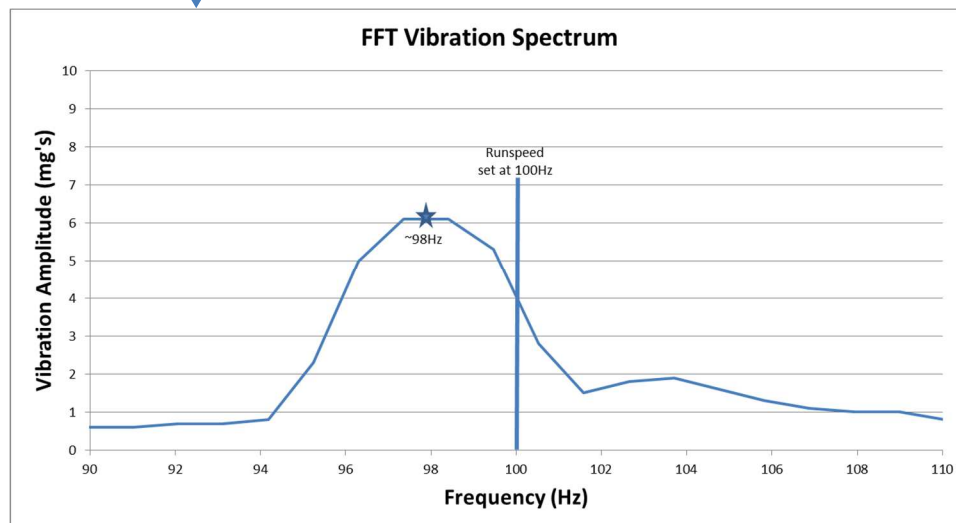


Figure 3.24: Vibration spectrum zoomed in on runspeed vibration spike.

Upon close inspection of the runspeed vibration, it is clear that the assumption that the empirical runspeed matches the frequency drive's intended rotation set point is not accurate. In the example, there is a 2% difference.

Generally speaking for the particular rotor/stator configuration used in this work, the vibration peak is a few percentage points below the set point of the drive. Coupling between the rotor and the stator is not 100% efficient; there is some slip. Slip is defined as "the difference between the synchronous speed of the magnetic field [of the stator] and the shaft rotating speed" [34]. It explains differences between theoretical and experimental values. The slip creates a proportional change across the expected bearing frequencies because each theoretical frequency is directly proportional to runspeed. As an example, the table below lays out the impact of the difference:

	Assumed conditions	Actual Conditions	Difference
Runspped:	100Hz	98Hz	2Hz (2%)
Calculated vibe frequency:	789Hz	773Hz	16Hz (2%)
Calculated 1 st harmonic:	1578Hz	1546Hz	32Hz (2%)

Table 3.2: Effect of rotor slip on resonant and harmonic frequencies.

The percent difference between the actual and assumed conditions is only two percent, but this amounts to a 16Hz absolute differential at the resonant vibration frequency. Accordingly, this error propagates through the data set when reviewing harmonics under the assumption of the nominal 100Hz runspeed condition. The first harmonic, defined as twice the original frequency, is now separated by 32Hz, and so on with more harmonics. Slip creates the need to search for a peak in wider and wider ranges of frequencies with each successive harmonic. Very quickly the process drives out of control; the probability of correctly identifying the peaks in relation to a particular component goes nearly to zero as the tolerance zones of the expected harmonics of different components begin to overlap. This issue is further exacerbated by the presence of system interactions. The background noise may easily fall within and around

the tolerance zones of the expected vibration frequencies rendering it impossible to differentiate between bearing peaks and noise in the data.

The runspeed can be accounted for to accurately find expected vibration peaks. The following three figures are measurements to convey that the runspeed value is quite dynamic despite a single 100Hz set point on the frequency drive.

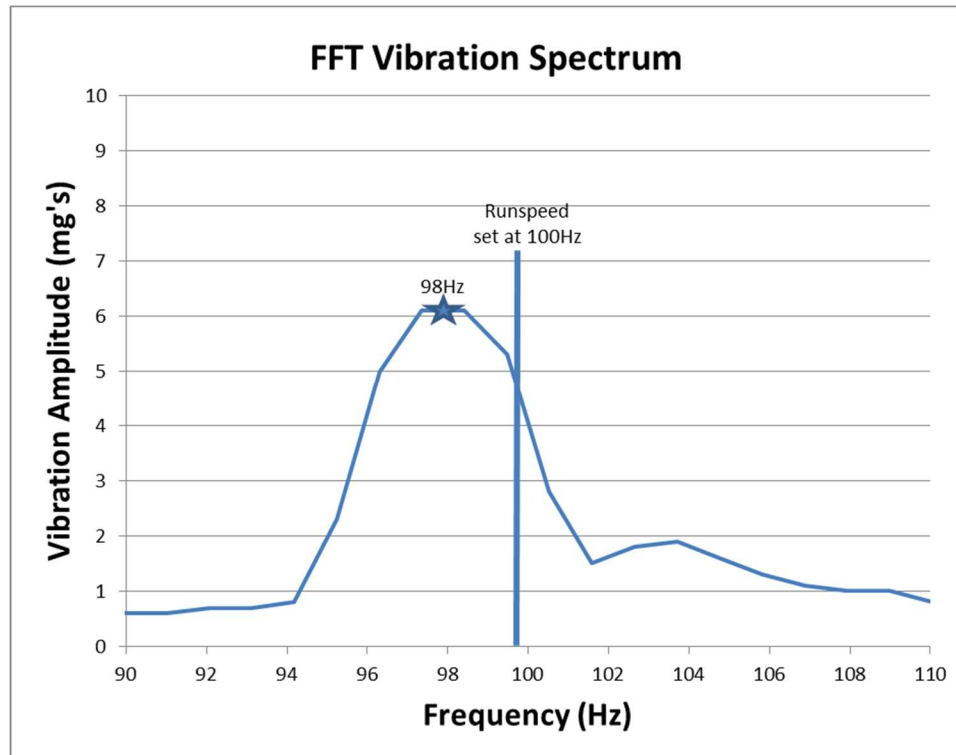


Figure 3.25: Bearing 1, Measurement 1

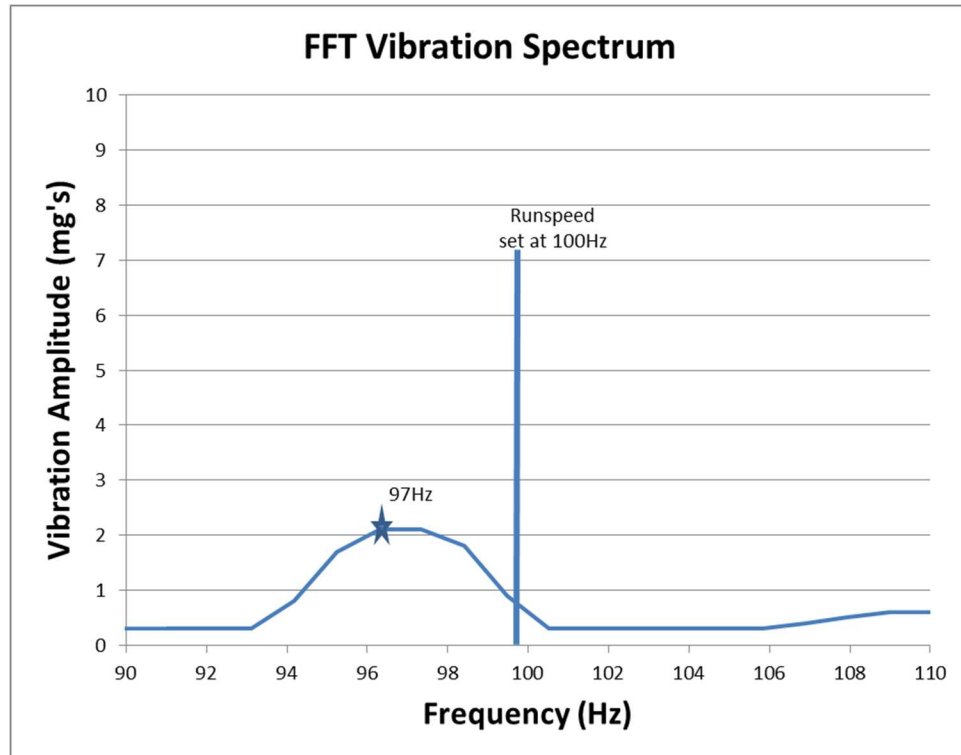


Figure 3.26: Bearing 1, Measurement 2

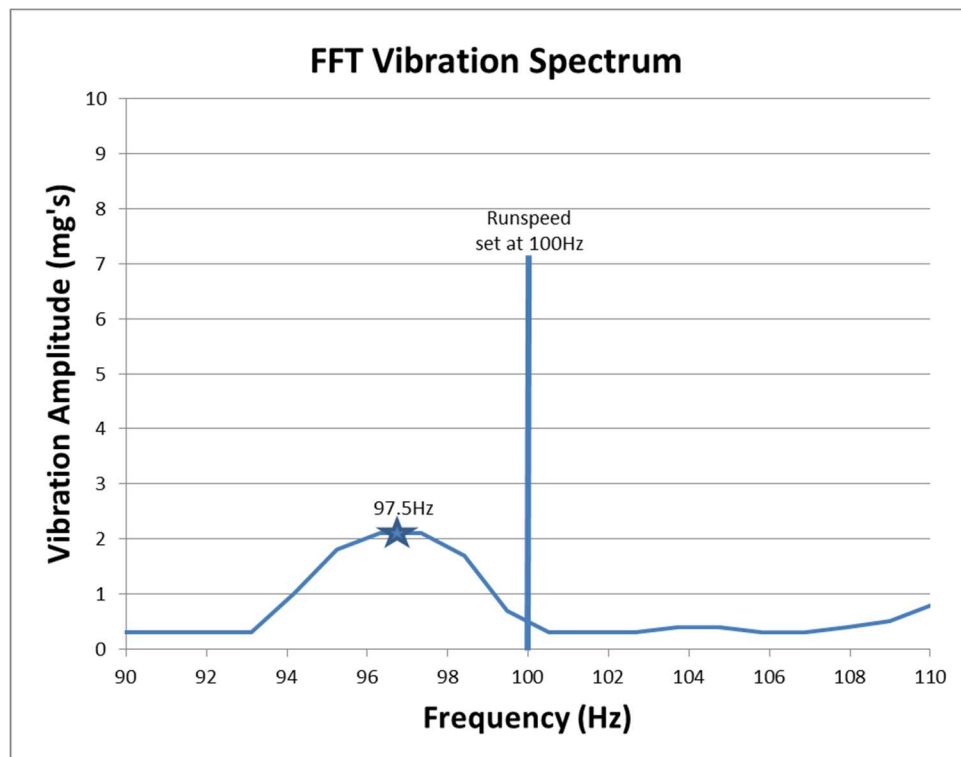


Figure 3.27: Bearing 1, Measurement 3

The Monte Carlo simulation below accounts for the inconsistent runspeeds during data collection and component tolerance stackup.

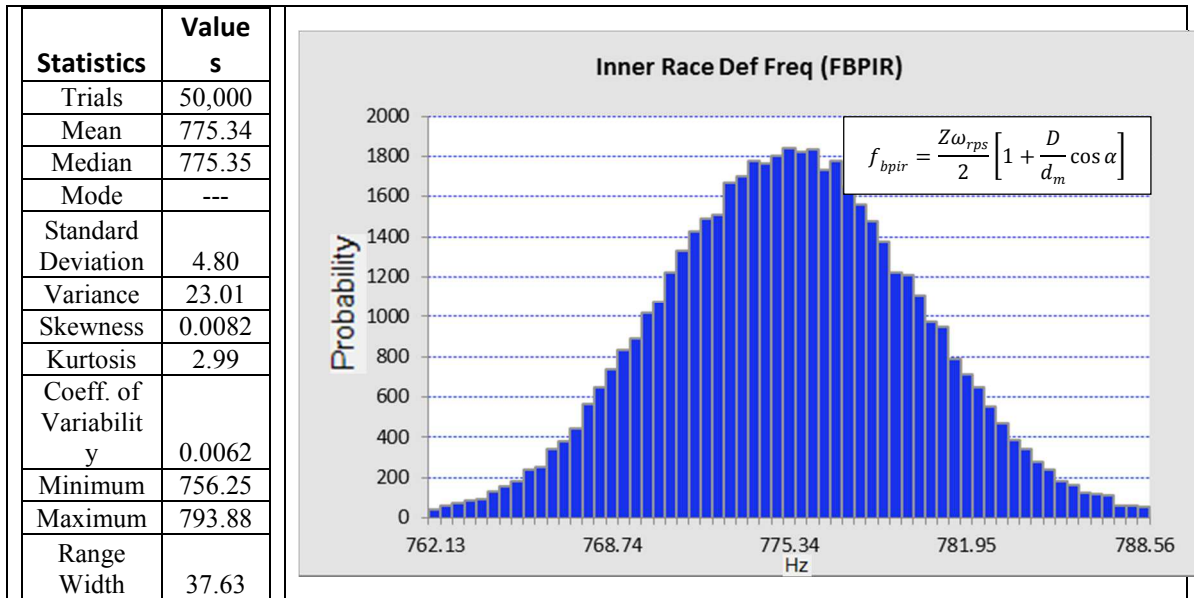


Table 3.3: Monte Carlo simulation: inner race defect frequency due to component tolerance stackup & runspeed variation.

Notice the mean shifted down in value and increased the variance. The increased range is undesirable because it allows for greater inaccuracies when searching for a vibration peak. Therefore, it is advantageous to develop a method to account for the runspeed of the data collected, a process called order analysis.

3.4.4 Runspeed Normalization Through Order Analysis

The method to account for and adjust to the runspeed of the system, as opposed to strictly controlling the runspeed during data collection, is called “Order Analysis”. It is the process of standardizing, or normalizing, the vibration spectrum to the runspeed of the shaft [19]. This improves the consistency from measurement to measurement, essentially making the software robust enough to be used with any speed of rotation.

The Monte Carlo simulations explain variation due to both tolerance stackup and the induction motor slip. Variation in expected frequency is most heavily due to runspeed variation. So, if we apply order analysis to every set of measurements, we can force the data to become representative of any runspeed. The variation in the expected theoretical frequency would be reduced to that of the tolerance stackup.

The following figure is an overlay probability chart for inner race defect frequency to explain the Matlab program’s application of order analysis. The distribution on the right is the theoretical inner race defect frequency probability density function normalized to a 100Hz runspeed; it takes into account the tolerance stackup due to component variation and assumes a single runspeed of 100Hz. The distribution on the left is also the theoretical inner race defect frequency probability density function, but it takes into account induction motor slip and the tolerance stackup due to component variation. The probability is not normalized to a 100Hz runspeed.

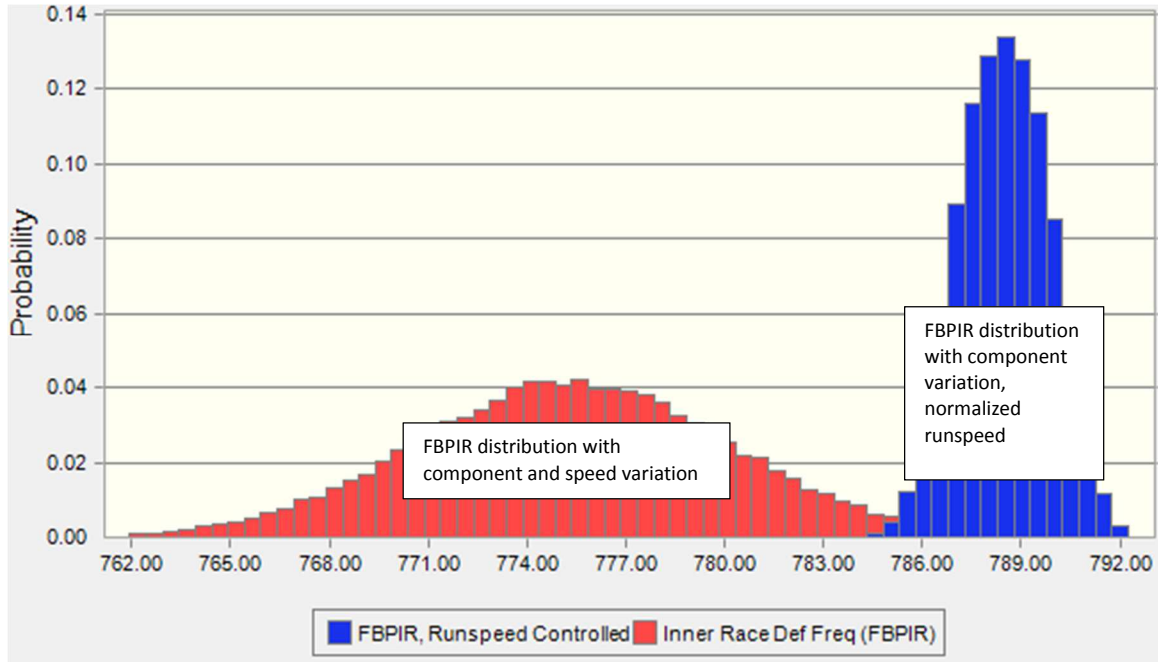


Figure 3.28: Probability distribution comparisons of component and speed variations.

The variation due to rotor slip in combination with the tolerance stackup of the components increased the frequency distribution range width to 37.6Hz from 8.8Hz. It should also be noted that the central tendency shifted downward because the slip model assumes the speed cannot occur at the 100Hz set point. The table summarizes the influence on the spread of the distribution around the example theoretical frequency:

	Standard Deviation	Range Width
Distribution with Component Variation	1.34Hz	8.80Hz
Distribution with Component and Speed Variation	4.80Hz	37.63Hz
Reduction in Uncertainty with Control of Runspeed	$1 - \frac{1.34}{4.80} = 72\%$	$1 - \frac{8.80}{37.63} = 76\%$

Table 3.4: Summary of the influence of component and runspeed tolerance stackup on theoretical frequencies.

The application of order analysis allows one to force the inner race frequency raw data to follow the tighter distribution even when the data was taken at 98Hz. That is, order analysis negates the effect of rotor slip. The application is thoroughly discussed in the results section.

It is shown that the spread of the theoretical distributions is reduced by about 70+% if the runspeed is well-defined. In other words, if the runspeed is controlled, or rather the variations in speed accounted for, the theoretical bearing calculations can be changed accordingly to improve the probability of correctly identifying vibration peaks with greater certainty. This same analysis is done for all frequencies of interest.

4 Results and Discussion

The input to the work is comprised of vibration spectral data and fundamental bearing theory. The output of the work is composed of the following:

1. A Matlab program designed to seek vibration amplitudes at characteristic frequencies
2. A vibration transfer function between a sub-assembly test rig and a full assembly-level casing through the application of the Matlab analysis program

The application of bearing theory, Monte Carlo simulation, and Order Analysis in a Matlab program is promising. Between measurements of a single bearing assembly, the runspeed normalization proves to be a powerful mechanism to review vibration data from measurement to measurement within the same platform. Measurements are stable within each respective system. However, there proved to be little vibration correlation between each platform, given the same bearing. The vibration transfer function developed is about 50% accurate of predicting vibration populations correctly with a 72% confidence interval. This is discussed in detail in the following sections.

4.1 Matlab Vibration Analysis Tool

The concepts outlined in this thesis are successfully implemented in vibration software.

This section discusses the Matlab algorithm to find and collect vibration amplitudes at theoretical frequencies.

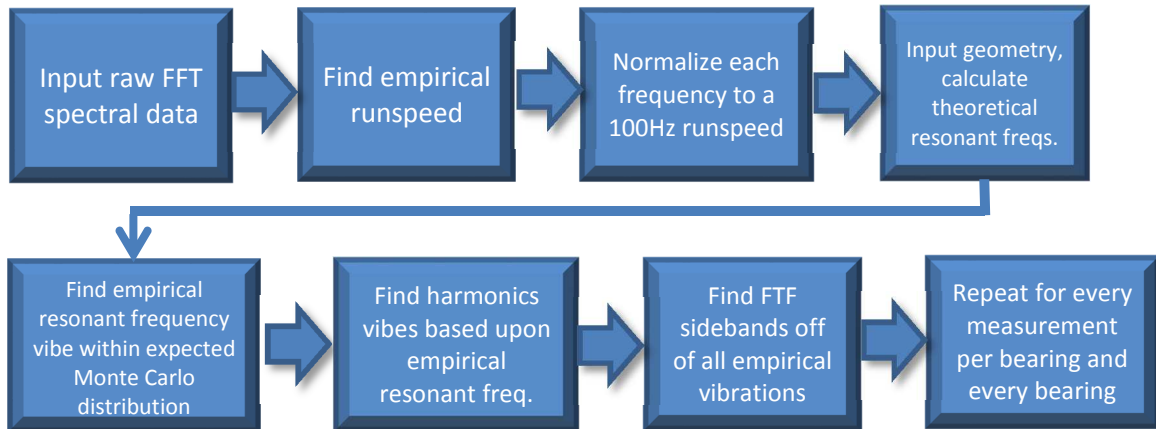


Figure 4.1: Block diagram of vibration analysis algorithm.

The FFT spectral data comes into Matlab as a 2-dimensional spreadsheet. Each cell is vibration amplitude measured with a 15 second linear average. Each column is a subsequent measurement in time. The rows go from 18.6667Hz to ~5000Hz in increments of 1.3333Hz.

4.1.1 Runspeed Detection and the Application of Order Analysis

Bearing runspeed is expected to be in the 100Hz range, so the maximum vibration amplitude is sought within a range around 100Hz. It can be seen in Figure 4.3 that although the set point is at 100Hz, the empirical vibration is at 98Hz. This difference in runspeed directly and proportionally impacts bearing-related frequencies. At this point, runspeed normalization through order analysis is applied to track the bearing performance. It should be noted that data manipulation in this manner will accurately track the bearing but skew any stationary background noise, basically any vibrations not directly proportional to runspeed. This is acceptable because the outcome of the analysis is designed to preferentially pick bearing speed related frequencies and ignore everything else.

If the empirical runspeed is measured to be 98Hz, the associated spectral data is normalized with the following formula:

$$f_i \times \frac{100\text{Hz}}{98\text{Hz}}$$

Equation 4.1: Runspeed normalization

The runspeed becomes exactly 100Hz as each frequency increases by 2.04%. The inner race defect frequency, for example, goes from 769Hz to 786Hz. The following example walks through and verifies the normalization concept. The inner race frequency is used to illustrate how the normalization impacts bearing-related frequencies, but the concept is applied to all bearing frequencies of interest.

Figure 4.2: Raw dataset of FFT spectrum: to be used to demonstrate order analysis

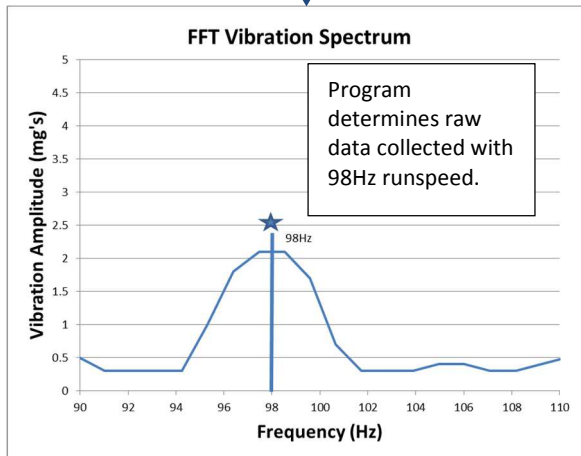
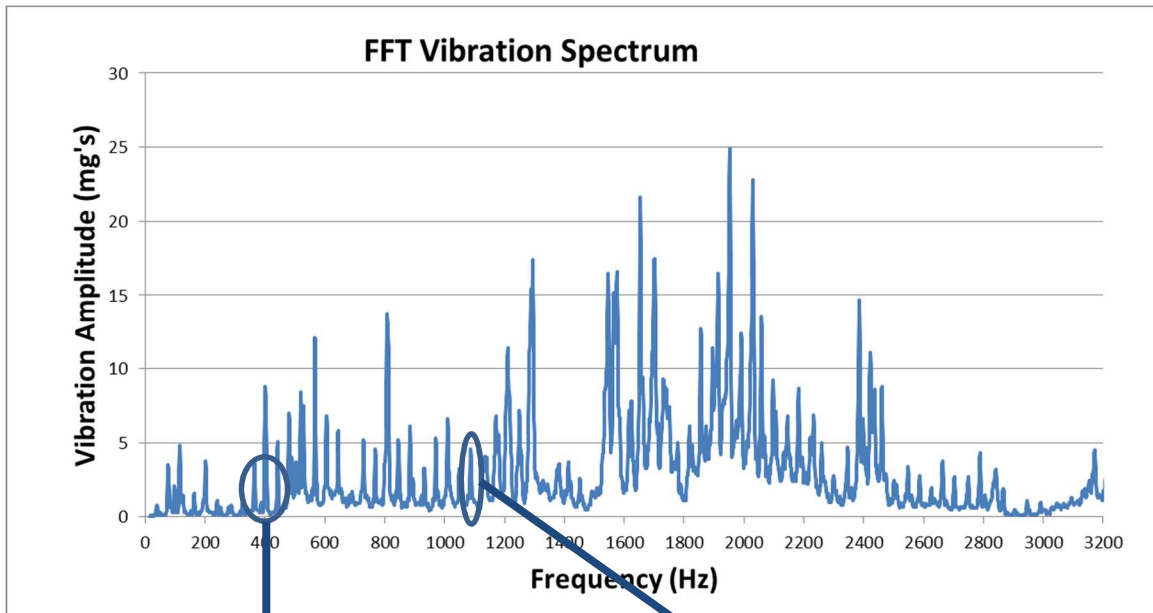


Figure 4.3: Runspeed vibrate at 98Hz with set point of 100Hz.

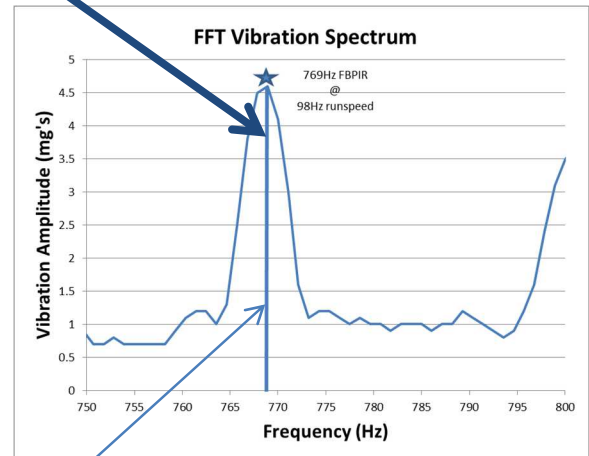


Figure 4.4: Inner race vibrate at 769Hz with 98Hz runspeed.

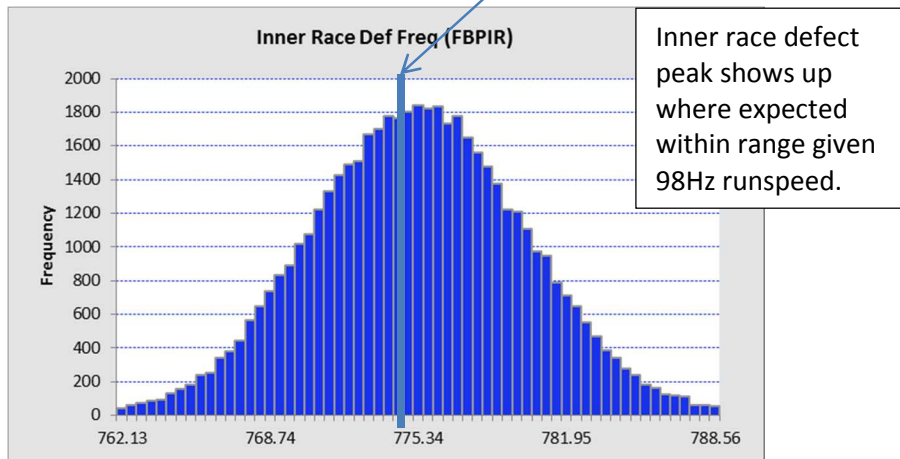


Figure 4.5: Monte Carlo graph of expected inner race frequencies.

The measurement must be normalized to a 100Hz runspeed to be compared against other data sets. All frequencies on the x-axis will increase by about 2% with the application of the ratio 100/98.

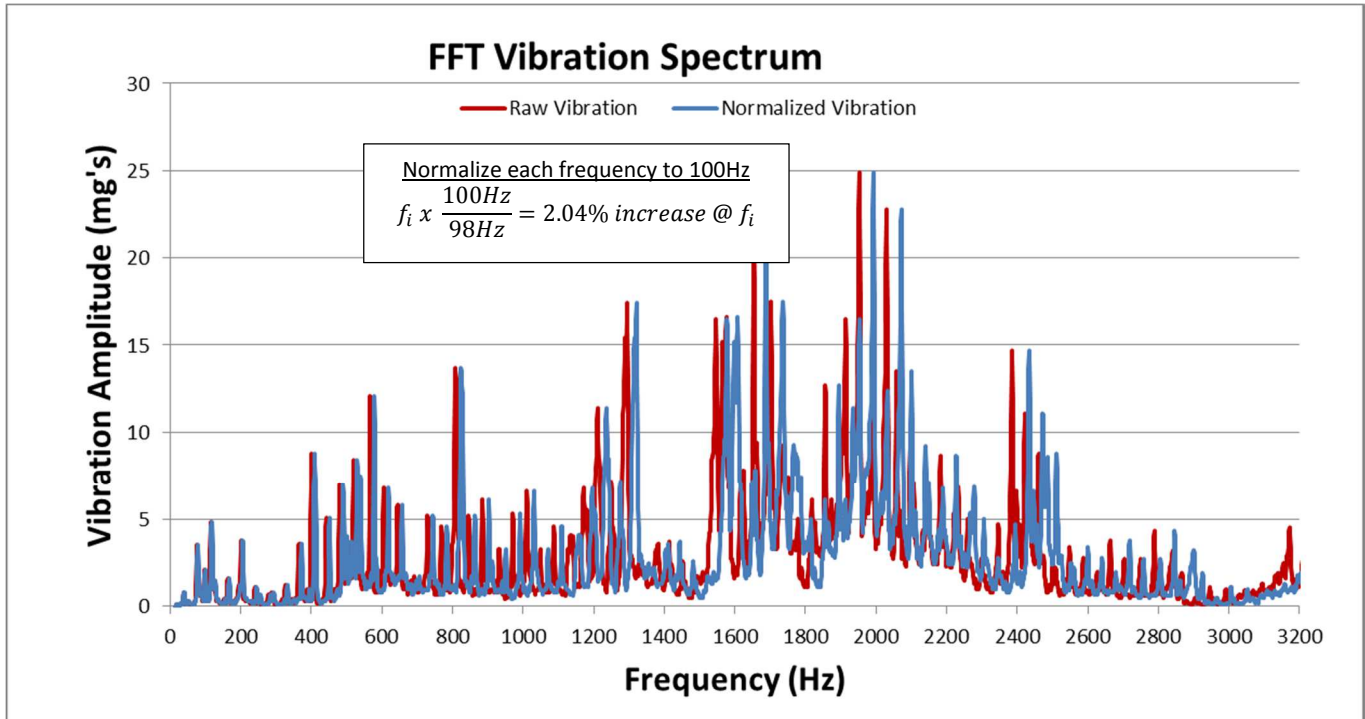


Figure 4.6: Raw dataset shifted by 100/98 for all frequencies

The effect of the normalization causes the spread between the raw data to increase gradually as the x-axis values increase. This is expected because the frequencies change by a percentage, not a finite difference.

The following page serves as verification that runspeed normalization is effectively applied in the search for characteristic vibrations. Note the inner race defect frequency vibration peak normalizes as expected.

Figure 4.7: Normalized dataset to be used for vibration analysis.

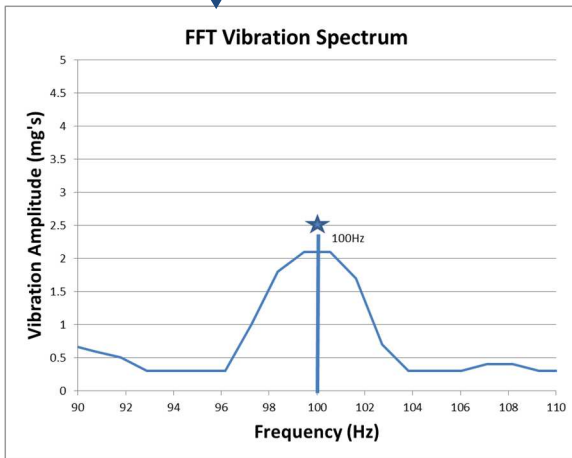
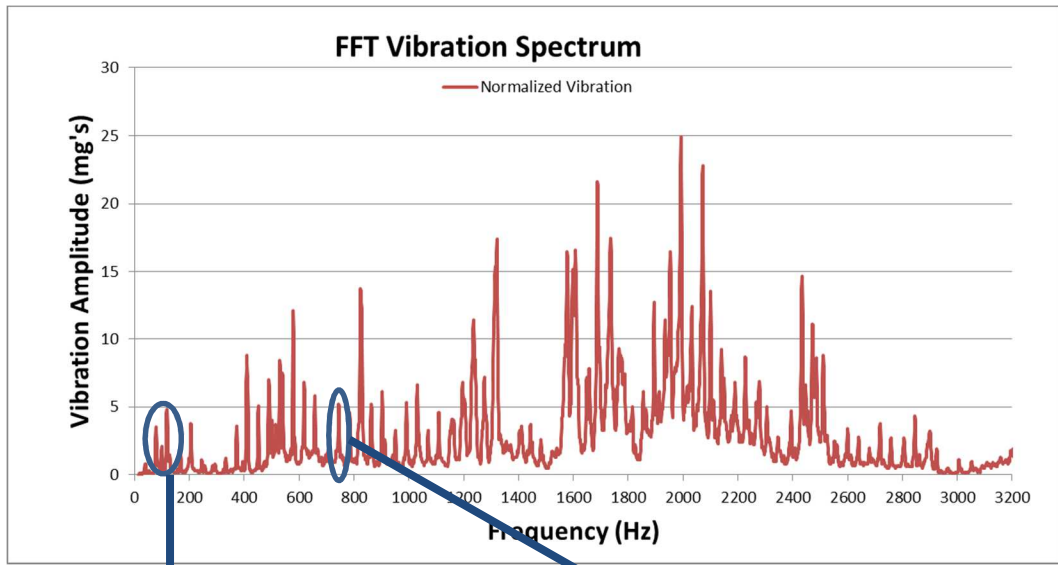


Figure 4.8: Runspeed vbe at 100Hz

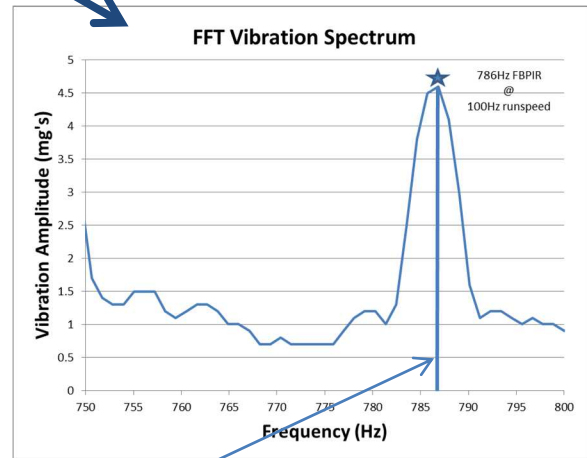
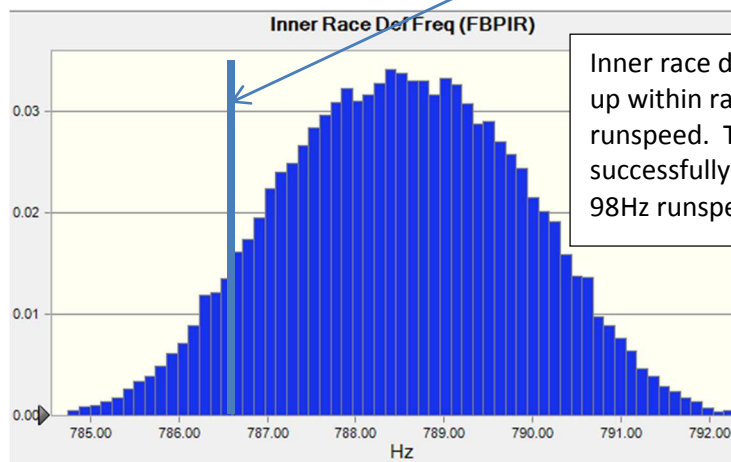


Figure 4.9: Inner race freq. at 786Hz due to 100Hz runspeed



Inner race defect peak shows up within range given 100Hz runspeed. The frequency successfully migrated from the 98Hz runspeed condition.

Figure 4.10: Monte Carlo graph of expected inner race frequencies.

The location of the runspeed in the frequency domain proves to be one of the most important aspects of the automated vibration analysis script. The uncertainty of finding the empirical peak within a range of theoretical frequencies is reduced by greater than 70% as previously mentioned. Thus, it is concluded that normalization is a very powerful means for strengthening relationships of characteristic frequencies between data sets. Taking the shaft speed into account, the program finds the bearing vibration peaks, and their harmonics, without the setbacks incurred with the assumption of a single runspeed value.

4.1.2 Spectral Analysis and Data Mining

The order analysis and normalization processes set the stage for the data mining aspect of the vibration code. It is at this point that the useful information regarding the descriptive vibration amplitudes of the bearing is extracted and stored for analytical purposes.

Anything that is not specifically related to the operation of the bearing is ignored and considered background noise. The effect of system interaction on the bearing is accounted for in two ways:

1. The system on which the bearing vibration data is gathered is standardized. The same set up is used every time and follows a strict set of procedures to remove gage error as much as possible.
2. The influence of the system on bearing operation will be present for every data set and will carry through all analyses.

The natural frequencies of the bearing are calculated based upon the nominal dimensions of the bearing and the 100Hz runspeed. The theoretical characteristics are as follows:

Theoretical Frequencies Component Dimensions: Nominal Runspeed: 100Hz (6000RPM)		
$f_c = FTF = \frac{\omega_{rps}}{2} \left[1 - \frac{D}{d_m} \cos \alpha \right]$	Fundamental train (cage) frequency	39.4Hz
$f_{bpir} = \frac{Z\omega_{rps}}{2} \left[1 + \frac{D}{d_m} \cos \alpha \right]$	Ball pass frequency of the inner race (inner race defect frequency)	788.5Hz
$f_{bpor} = \frac{Z\omega_{rps}}{2} \left[1 - \frac{D}{d_m} \cos \alpha \right]$	Ball pass frequency of the outer race (outer race defect frequency)	511.5Hz
$f_r = \frac{\omega_{rps} P_d}{2D} \left[1 - \left(\frac{D}{d_m} \right)^2 \cos^2 \alpha \right]$	Ball spin frequency	204.6Hz
$f_{BDF} = BDF = 2xf_r$	Ball defect frequency	409.2Hz

Table 4.1: Resonant characteristic bearing frequencies at a constant, normalized runspeed of 100Hz.

The frequencies listed in Table 4.1 above will be henceforth referred to as the “nominal” resonant characteristic frequencies. They represent the base frequencies from which the analysis will take place. The frequencies are used to create harmonics, or integer multiples, of the resonant frequencies. Any vibration spikes found within the expected theoretical frequency range will be referred to as the “actual” or empirical frequency in the data.

After the software normalizes the dataset to the 100Hz runspeed, it next looks for the empirical resonant vibrations. It seeks the largest vibration peak within the theoretical range of frequencies predicted from the Monte Carlo tolerance stackup simulation. For each case, the expected variance around the theoretical frequency due to components is about 1%.

Then, the script seeks the harmonics of each of the resonant characteristic frequencies based upon the value of the empirical resonant frequency value, not the theoretical nominal. This helps to prevent error propagation throughout the data set. For instance, in the runspeed example, the nominal inner race resonant frequency is 788.5Hz while the empirical value

measured is 786Hz. The program adjusts its range of search to match multiples of the empirical 786Hz instead of the nominal 788.5Hz. For sake of discussion, in the search for the 3rd harmonic of the inner race defect frequency, the program centers on the multiple of the empirical resonant of 786Hz, not the multiple of the theoretical resonant of 788.5Hz. The program bounds its search for a peak around 3144Hz, not around 3154Hz. This method increases accuracy.

	Actual	Theoretical
3 rd harmonic	$4 \times 786\text{Hz} = 3144\text{Hz}$	$4 \times 788.5\text{Hz} = 3154\text{Hz}$

Table 4.2: Third harmonic calculations.

Finally, the vibration analysis program seeks the interactions between the frequencies: sidebands. Specifically, the software looks for regularly-spaced spikes due to the fundamental train frequency.

These concepts applied to the inner race frequency are repeated for every measurement of every bearing tested to compile vibration magnitude distributions at all frequencies of interest.

4.1.3 Effectiveness of Matlab Vibration Analysis Algorithm

The following spectral graphs illustrate the success of the concepts applied to determine bearing vibration characteristics. First, the graph below is an example of FFT data manually reviewed in Excel to understand that the peaks did in fact relate to theoretical phenomena.

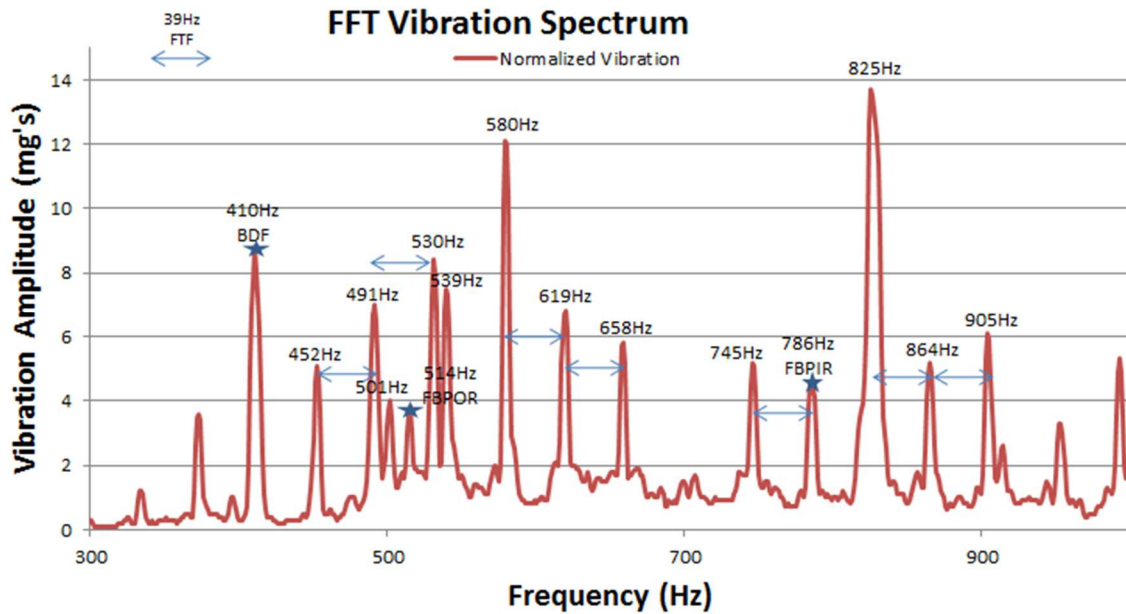


Figure 4.11: Characteristic peaks first identified in Excel to be captured for analysis in the vibration analysis program.

In this snapshot, the stars indicate the location of the empirical characteristic frequencies located as expected. The surrounding peaks are due to sidebands of the fundamental train frequency. It is plain to see that the excessive number of peaks beyond the three primary frequencies (f_{bpir} , f_{bpor} , and f_{BDF}) are the result of sideband interactions off these three frequencies. For illustrative purposes, the arrows are the width of the fundamental train frequency, 39Hz.

The next graph, presented below, is an example of the output from the bearing program. The program is deemed conceptually successful because it is able to recreate the manual Excel graphs and find meaningful peaks in an automated manner. The stars (or black squares with coordinates) represent the vibration magnitude data stored by the program. The continuous lines represent the full spectra of each measurement.

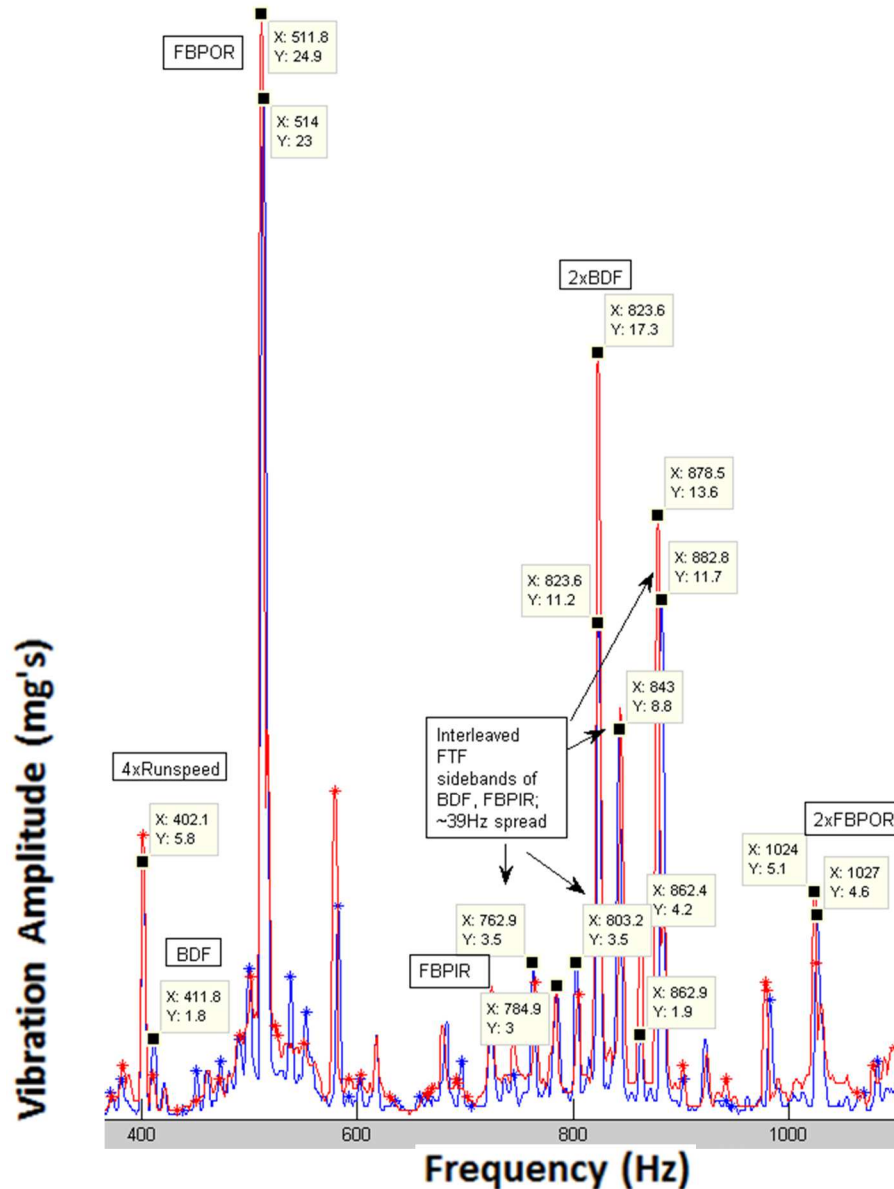


Figure 4.12: Characteristic peaks identified and captured with Matlab algorithm for statistical analysis.

The graph is composed of two signals from the casing level vibration tests. The two signatures are laid on top of one another as a means to indicate the repeatability and reproducibility of the data captured, in part because of order analysis. From a visual inspection, it is seen that each pattern, taken minutes apart, trend together in a macro sense.

The graph on this page is a full view of the previous graph. f_{bpir} , f_{bpor} , and f_{BDF} and their associated harmonics trend together, but with slightly different magnitudes, hence the need to take multiple measurements to create a statistical description of amplitudes. The two spectra do not completely follow each other. Notice the sidebands around FBPOR. The blue spectrum has much more prominent spikes, just part of the random nature of vibration patterns.

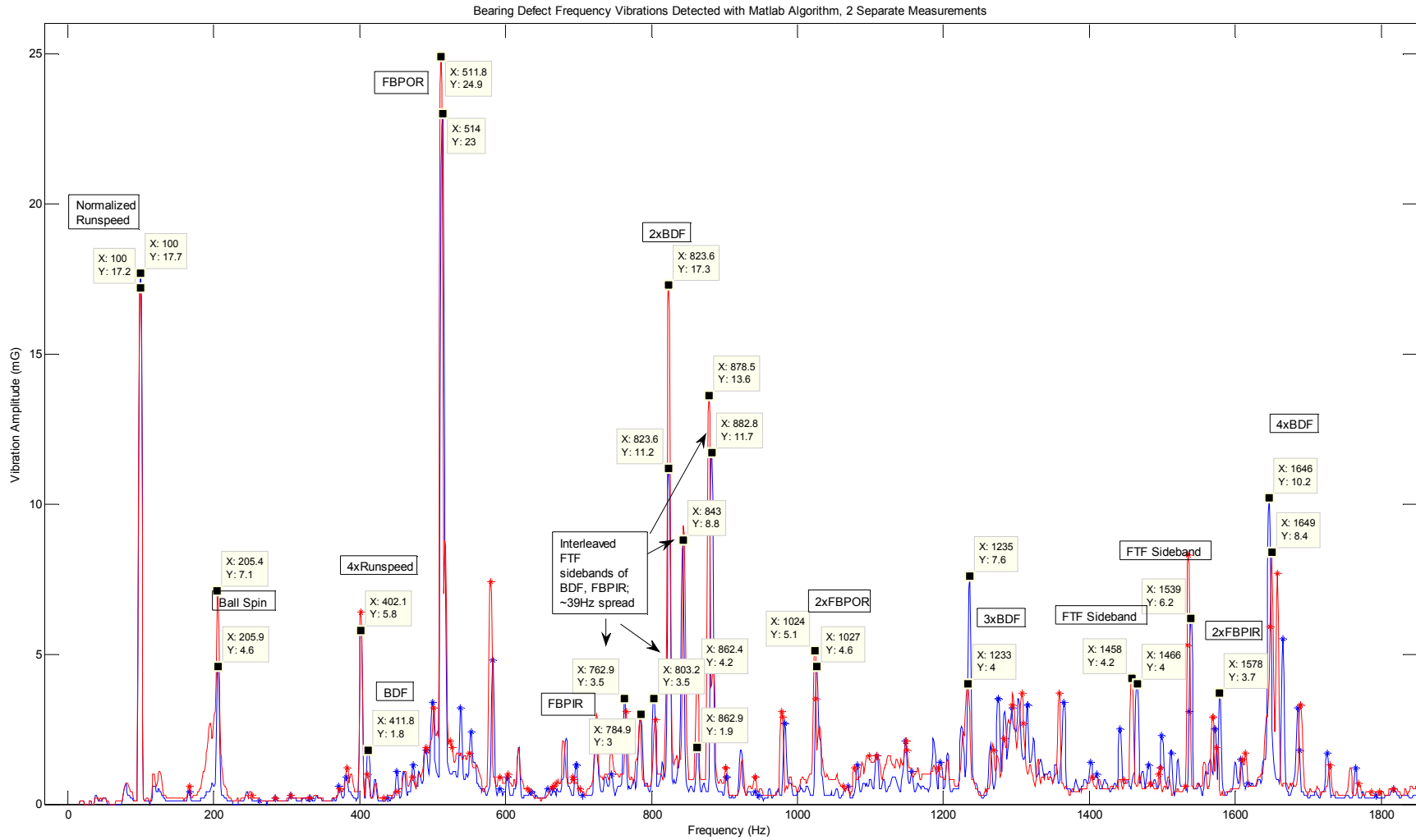


Figure 4.13: Characteristic peaks identified and captured with Matlab algorithm for statistical analysis.

The values of the two signatures displayed in the previous graphs are presented in the following table. The resonant frequencies and harmonics are highlighted. Notice the measured frequencies are below two percent difference from the theoretical nominal values at 100Hz runspeed.

Table 4.3: Table of expected and measured values for two vibration spectra from a single bearing

Row	Type	Nominal Freqs. (Hz)	Measurement1 (Blue)		Measurement2 (Red)		%Diff. Between Nominal and Measured Frequencies, Meas1	%Diff. Between Nominal & Measured Frequencies, Meas2
			Freq. (Hz)	Vibe Amp. (mG)	Freq. (Hz)	Vibe Amp. (mG)		
1	RunsPEED	100.00	100.00	17.7	100.00	17.2	0.00%	0.00%
2	Ball Spin	204.60	205.91	4.6	205.37	7.1	0.64%	0.38%
3	RunsPEED	300.00	306.45	0.3	305.37	0.3	2.15%	1.79%
4	FTF Sideband	330.48	332.79	0.2	331.18	0.2	0.70%	0.21%
5	FTF Sideband	369.83	372.04	0.6	373.11	0.5	0.60%	0.89%
6	RunsPEED	400.00	402.15	5.8	402.15	6.4	0.54%	0.54%
7	Ball Defect	409.17	411.82	1.8	410.21	1	0.65%	0.25%
8	FTF Sideband	432.80	438.17	0.2	433.33	0.2	1.24%	0.12%
9	FTF Sideband	448.52	451.07	1.1	450.53	0.4	0.57%	0.45%
10	FTF Sideband	472.15	473.65	1.3	472.04	0.9	0.32%	0.02%
11	FTF Sideband	487.86	490.85	1.8	490.85	1.9	0.61%	0.61%
12	RunsPEED	500.00	499.99	3.4	501.07	3.2	0.00%	0.21%
13	Outer Race	511.49	513.97	23	511.82	24.9	0.48%	0.06%
14	FTF Sideband	550.84	552.68	2.4	551.07	1.7	0.33%	0.04%
15	FTF Sideband	590.18	592.47	0.5	592.47	0.9	0.39%	0.39%
16	RunsPEED	600.00	602.68	0.9	603.22	1	0.45%	0.54%
17	RunsPEED	700.00	696.77	1.3	693.54	0.8	0.46%	0.92%
18	FTF Sideband	709.82	706.44	0.3	701.60	0.5	0.48%	1.16%
19	FTF Sideband	739.66	744.61	1	744.61	1.8	0.67%	0.67%
20	FTF Sideband	749.16	744.61	1	744.61	1.8	0.61%	0.61%
21	FTF Sideband	779.00	784.94	3	783.86	2.9	0.76%	0.62%
22	Inner Race	788.51	784.94	3	783.86	2.9	0.45%	0.59%
23	RunsPEED	800.00	803.22	3.5	805.37	2.8	0.40%	0.67%
24	2X Ball Defect	818.35	823.65	11.2	823.65	17.3	0.65%	0.65%
25	FTF Sideband	827.85	823.65	11.2	823.65	17.3	0.51%	0.51%
26	FTF Sideband	857.69	862.89	1.9	862.35	4.2	0.61%	0.54%

27	FTF Sideband	867.20	862.89	1.9	862.35	4.2	0.50%	0.56%
28	FTF Sideband	897.04	902.68	0.9	902.14	1.2	0.63%	0.57%
29	FTF Sideband	944.30	947.30	0.3	941.92	0.9	0.32%	0.25%
30	FTF Sideband	983.64	982.78	2.7	979.56	2.9	0.09%	0.42%
31	2X Outer Race	1022.99	1026.8 7	4.6	1023.64	5.1	0.38%	0.06%
32	FTF Sideband	1062.33	1068.8 0	0.6	1063.43	0.6	0.61%	0.10%
33	FTF Sideband	1101.68	1108.5 9	1.6	1097.84	1.6	0.63%	0.35%
34	FTF Sideband	1148.83	1155.9 0	1.1	1150.52	1.8	0.62%	0.15%
35	FTF Sideband	1188.17	1196.2 2	1.4	1193.00	1.2	0.68%	0.41%
36	3X Ball Defect	1227.52	1235.4 7	7.6	1233.32	4	0.65%	0.47%
37	FTF Sideband	1266.87	1274.7 1	3.5	1268.80	1.8	0.62%	0.15%
38	FTF Sideband	1306.21	1315.0 4	3.3	1307.51	3.7	0.68%	0.10%
39	FTF Sideband	1455.79	1464.5 0	4	1457.51	4.2	0.60%	0.12%
40	FTF Sideband	1495.13	1498.9 1	2.3	1496.75	1.2	0.25%	0.11%
41	FTF Sideband	1498.32	1496.7 5	1.2	1494.60	1	0.10%	0.25%
42	3X Outer Race	1534.48	1538.6 9	6.2	1535.46	8.3	0.27%	0.06%
43	FTF Sideband	1537.67	1536.5 4	3.1	1533.31	5.3	0.07%	0.28%
44	FTF Sideband	1558.00	1571.4 8	2.5	1568.80	2.9	0.87%	0.69%
45	FTF Sideband	1573.83	1578.4 7	3.7	1574.71	1.9	0.30%	0.06%
46	2X Inner Race	1577.01	1571.4 8	2.5	1568.80	2.9	0.35%	0.52%
47	FTF Sideband	1597.35	1607.5 1	1.5	1609.66	1.5	0.64%	0.77%
48	FTF Sideband	1613.17	1617.1 8	0.7	1613.42	1.7	0.25%	0.02%
49	FTF Sideband	1616.36	1607.5 1	1.5	1612.88	1.7	0.55%	0.22%
50	4X Ball Defect	1636.69	1646.2 2	10.2	1647.29	5.9	0.58%	0.65%
51	FTF Sideband	1655.70	1646.2 2	10.2	1649.44	8.4	0.57%	0.38%
52	FTF Sideband	1676.04	1685.4 6	3.2	1689.23	3.3	0.56%	0.79%

Table 4.3 Continued: Table of expected and measured values for two vibration spectra from a single bearing.

The frequencies are listed in numerical order. As such, the FTF sidebands are not necessarily related to the highlighted fundamental frequency; they are interleaved from other resonant frequencies and/or harmonics. For example, this is the case for the resonant ball defect frequency at 411Hz (row 7). Notice the surrounding frequencies are not +/- 39Hz (FTF frequency). However, it is the case for the outer race defect frequency at 511Hz. Notice the subsequent frequencies (550Hz, 590Hz) are separated by about 39Hz.

The review of the signatures in the graph and the values in the table allows one to conclude the program is successful. There are some shortcomings, however. Each theoretical frequency has a tolerance band of about 1% in which to search for an expected peak. The concept works well when only one single prominent peak shows up within search bounds. A source of error in the algorithm occurs when the search boundaries of different frequencies overlap. Consider the first harmonic of the ball defect frequency, row 24: the empirical value is 823Hz for Measurement 1. The following FTF sideband in row 25 is the same 823Hz value, calculated from 39Hz plus the inner race frequency 785Hz. The analysis cannot distinguish between the two peaks. Subsequently, the program stores the same vibration amplitude of 11.2mm/s² (mG) for two different theoretical frequencies, 818Hz and 827Hz. The effect of the error can be minimized with increasing the samples to gain a further understanding of the overall population. It may be advantageous to parse the data with further post-processing. One could remove all sideband data and only review resonant and harmonic frequencies. That avenue was not pursued in this work.

If this overlap error occurs when determining the empirical resonant frequency, the error propagates throughout the vibe spectrum when searching for harmonics as discussed in the following example.

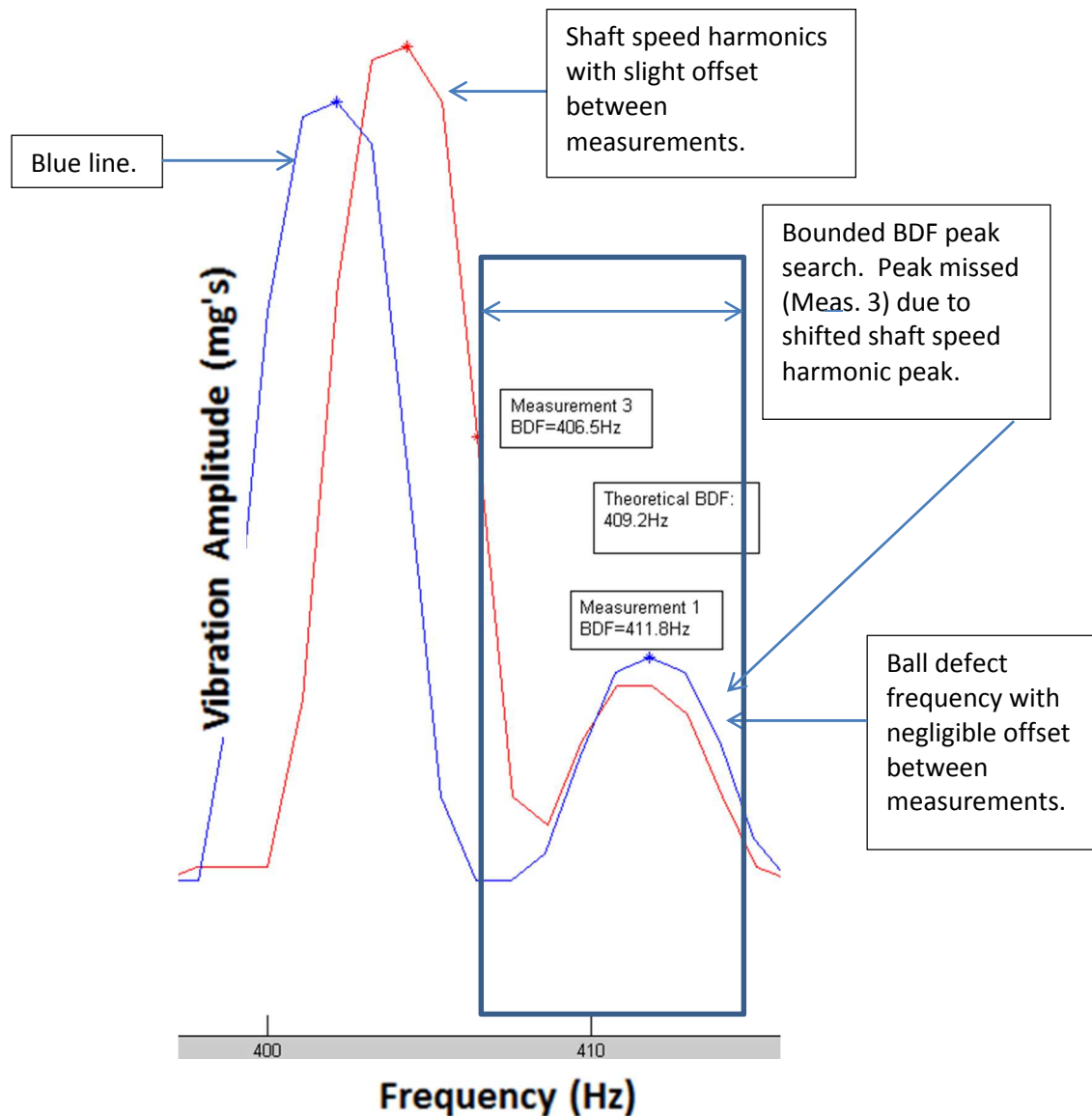


Figure 4.14: Shaft speed harmonic peak and ball defect frequency peak.

The blue line is from the Measurement 1 in the table. The red line represents a third data set taken minutes after Measurement 1. All measurements are from the same bearing. Notice that the BDF peaks on the right hand side of the graph are very similar to one another. However, the two peaks on the left are offset for some reason, another part of the random nature of the vibration. The program seeks the ball defect frequency around the right hand peaks. It correctly identifies 411.8Hz for the blue vibration, but not for the red. The program bounds its search represented by the box. Because the shaft speed harmonic peak on the left

shifted slightly as compared to Measurement 1, the frequency obtained for the BDF in Measurement 3 is inaccurate. The program thinks the maximum BDF peak is on the far left hand side of the box at 406.5Hz.

The error created propagates throughout BDF frequency harmonics.

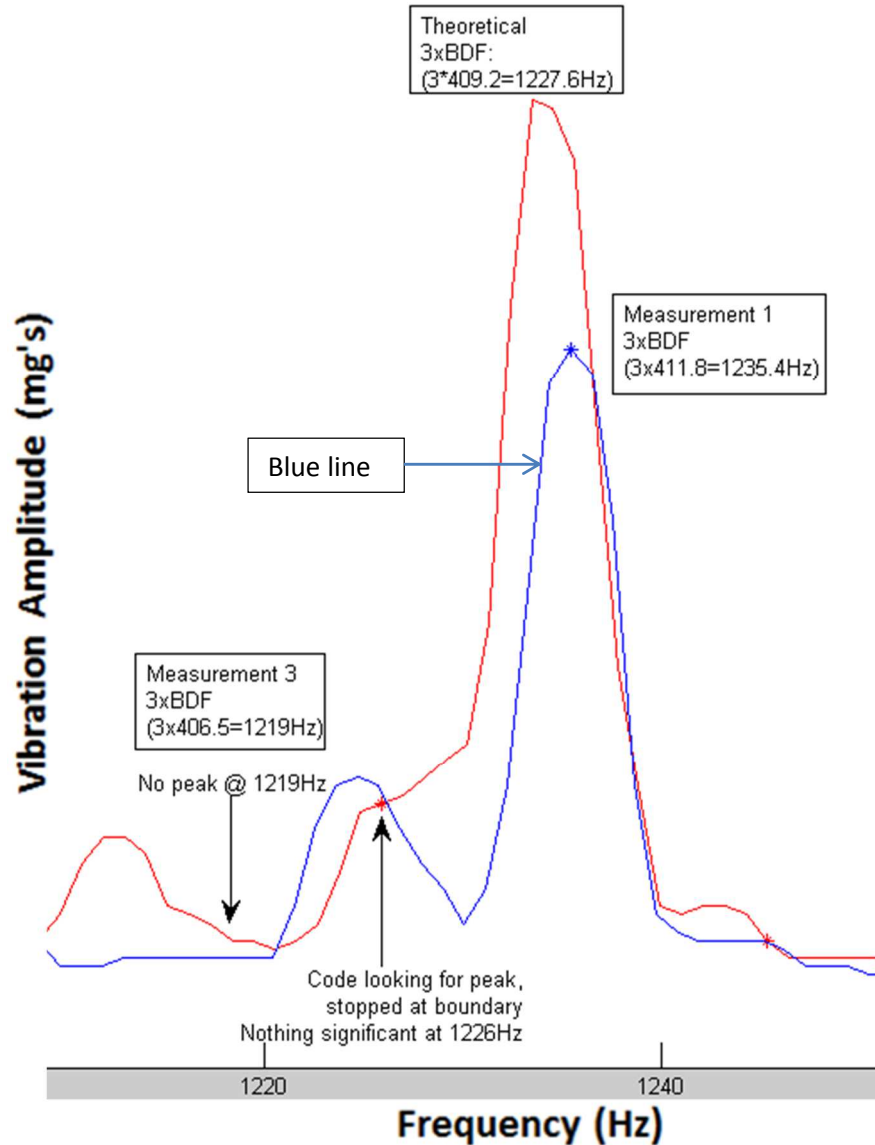


Figure 4.15: BDF error propagates through to harmonics.

The blue graph correctly identifies three times the empirical resonant ball frequency (note the star). In the red graph, it is shown that nothing significant exists at 1219Hz (another indication that the resonant frequency is inaccurate). The search did start moving up to the right towards where three times the ball frequency should be, but it stopped at the edge of the search boundary, the largest value within the search range.

It is observed that the BDF resonant frequency error propagation issue did not occur within the first two measurements of this single bearing. It occurred during the third measurement. Therefore, to accommodate for the random nature of the vibration, multiple samples are taken to minimize the probability of this risk. In general, taking more samples helps to smooth out data.

The previous discussion exemplified vibration from the casing level. Signatures plotted on top of one another showed generally good repeatability between measurements. It is also seen that vibration from the bearing rig had good correlation from measurement to measurement during operation of a single bearing. Each color is a separate measurement.

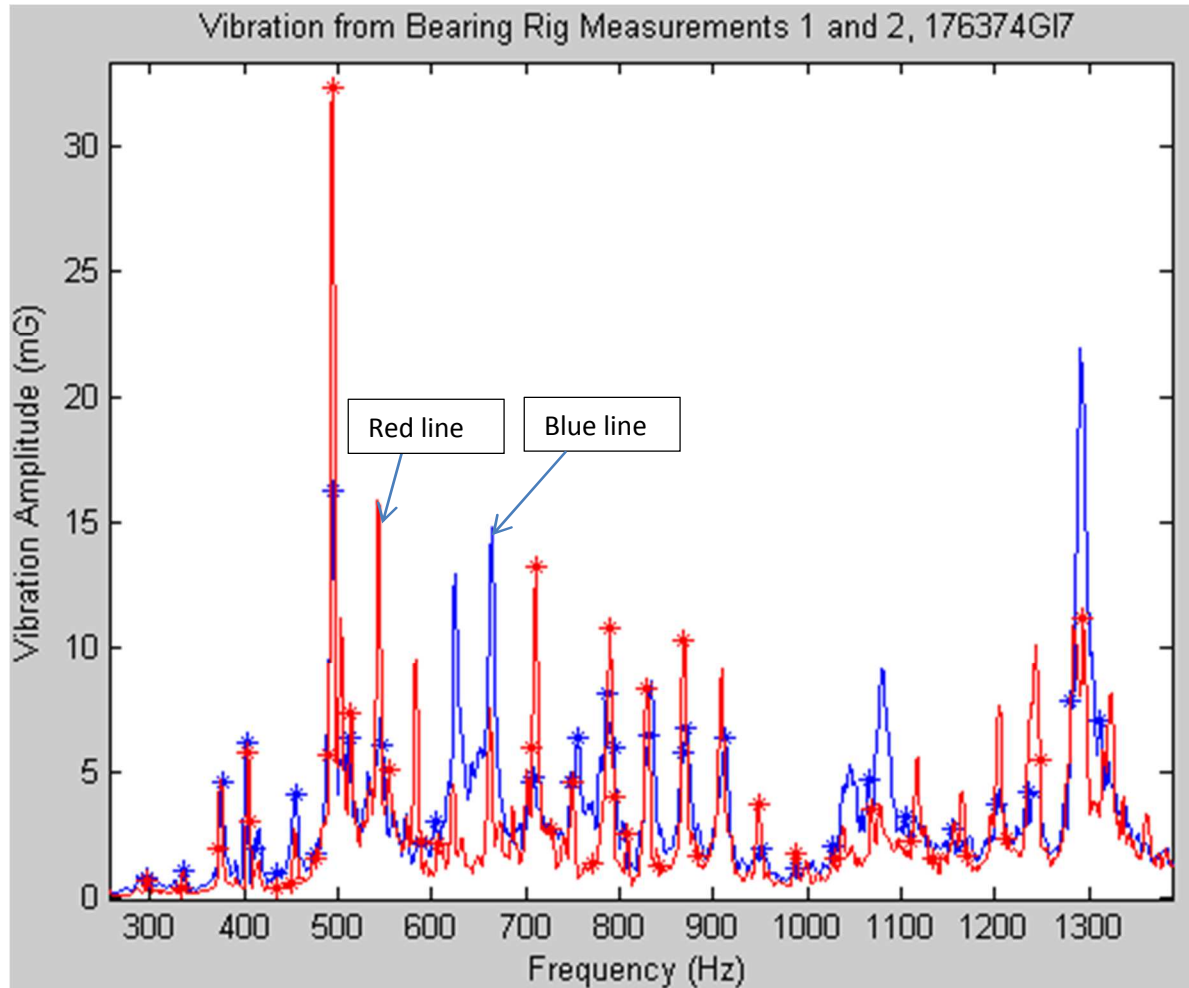


Figure 4.16: Correlation between measurements of a single bearing on the test rig.

Notice the macro trends between the two data sets; the peaks and troughs follow one another.

Additionally, many of the spikes line up with one another.

The figure on this page is a more broad view of the previous graph. The macro trends are similar between subsequent measurements (red vs. blue).

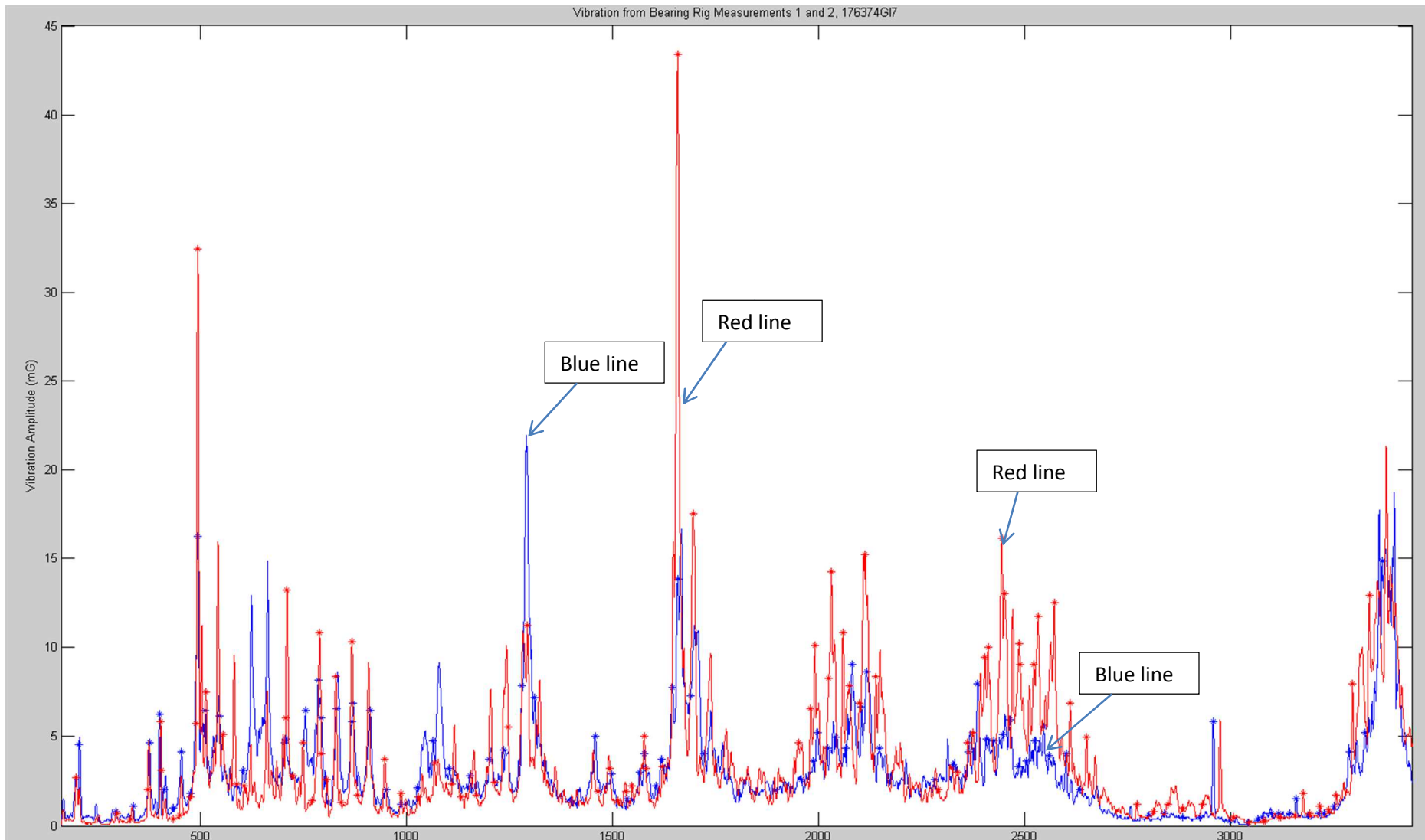


Figure 4.17: Measurement correlation within bearing rig system. One bearing's vibration signature trends to itself over multiple measurements.

It is important that multiple measurements of a single bearing trend together on a macro scale. It increases the accuracy of the collection of data to create a distribution. It would be a concern if peaks and troughs of the macro data were not in phase with one another. Although there are subtle differences in data values between measurements, with enough samples of each bearing, it is possible to create a meaningful distribution of vibration amplitudes from both the casing level tests and the bearing rig tests because the measurement data within its own respective system is stable compared to itself. Therefore, because each system is relatively stable in its own right, the systems are compared against one another for the creation of the transfer function, given the comparison is done with data from the same bearing.

4.1.4 Data Storage

Matlab is an effective medium to review large amounts of data in an automated manner. Much consideration was given to the method in which the data is stored because vibration at a given characteristic frequency has a distribution of amplitudes. Thus the performance of the bearing must be measured multiple times. This creates vast amounts of data to create descriptive statistics. It is important that the method of storage be effective to make sure that data from measurement to measurement represent the same physical phenomenon from data set to data set. In other words, vibration amplitude at the inner race defect frequency of one measurement must be associated with the amplitude of the inner race defect frequency of the next measurement in the subsequent data set. The practice of keeping the data separated between different characteristic frequencies reduces the opportunity to create irrelevant conclusions. If this occurs, the vibration amplitude population will not be physically meaningful.

Matlab stores data in matrices. The vibration program is set up such that any given cell location in a vibration storage matrix represents the same physical occurrence between measurements as required to adequately and appropriately describe the bearing. For example, if frequency f_{bpir} is in cell [1,1], every data set at cell [1,1] will represent the vibration amplitude at frequency f_{bpir} .

Recall the logic that went into finding the vibration at a given characteristic frequency. The vibration script scans the data for the largest peak within a range of frequencies. For f_{bpir} , in our runspeed example, the actual peak is at 786Hz instead of the nominal 788.5Hz. Therefore the vibration amplitude at 786Hz then goes into cell [1,1] in the data set. Cell [1,1] is considered to represent the condition of the inner race defect. Cell [1,1] will represent f_{bpir} no matter where the peak shows up within the expected range. If the next data set produces a peak at

790Hz, which is within the expected range, it is still considered to represent the condition of the inner race defect. Drift in the peak location may be due to several factors, such as a change in friction or rolling characteristics (19). Other factors include effects of the applied Hanning window. It is not the intention to describe the bearing with an account of the distribution of the empirical characteristic frequencies. The intent is to describe the distribution of the amplitude of the characteristic frequencies. The steps presented in the model development section provide certainty that the characteristic peak will fall within a given frequency range. Once the maximum vibration is found within that range, the analysis focuses on the vibration distribution and no longer the distribution of the frequencies.

The following graph is an example of the vibration storage method where only bearing frequencies are represented. The standard data storage method allows one to know what theoretical defect frequency is represented in every cell. Therefore, it is chosen to use the theoretical nominal frequencies to present the data. The x-axis in the graph is based upon the nominal frequencies of interest.

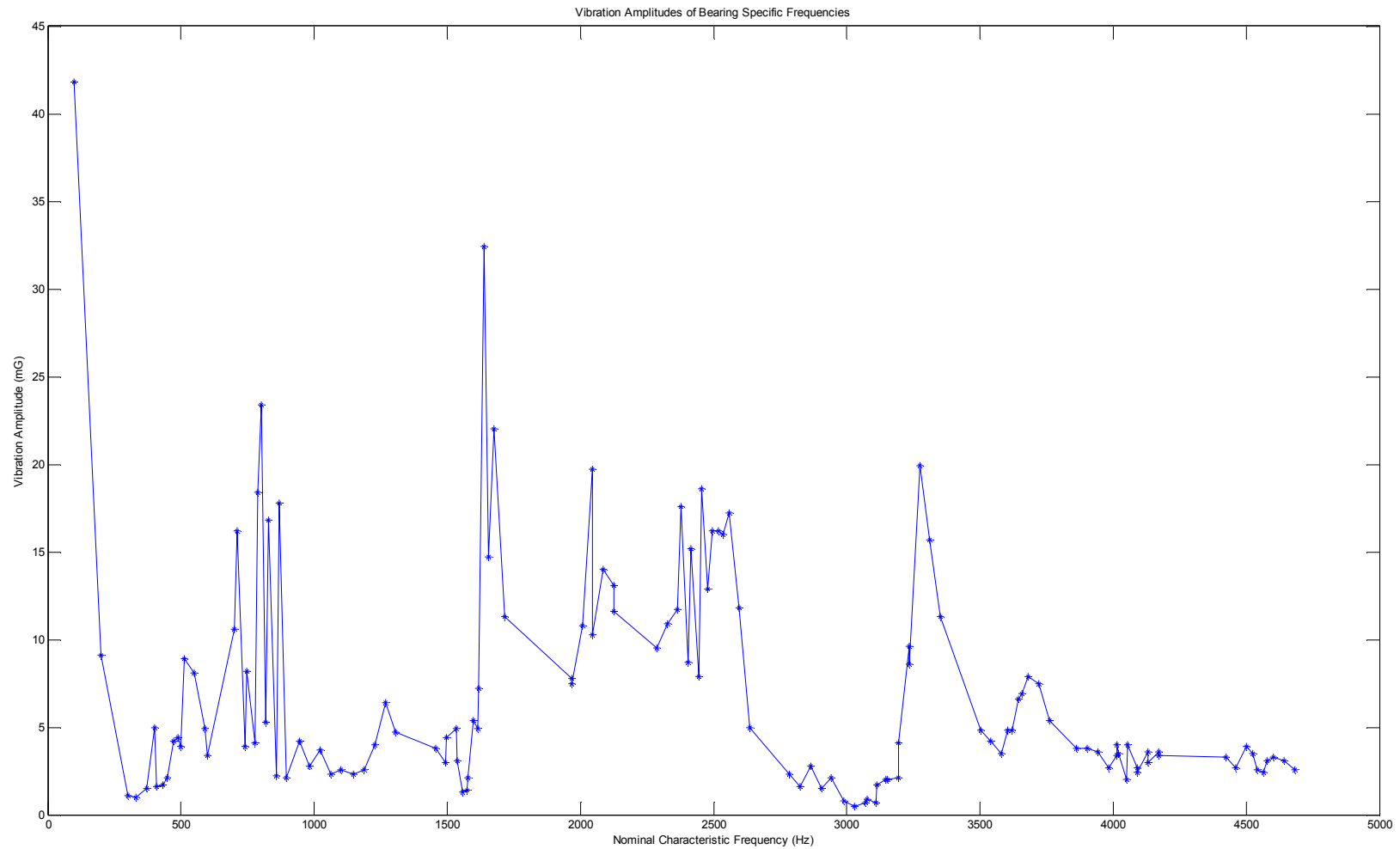


Figure 4.18: Vibration amplitudes from Matlab program plotted against standardized frequency values.

4.1.5 Data Analysis: Method of Descriptive Vibration Amplitude Statistics

With the methodology in place to find characteristic peaks and a standardized data storage mechanism set, the statistical analysis of the vibration data begins. Every bearing in question has multiple measurements per frequency that create a distribution of vibration magnitudes. The dotplot on the next page is an example Matlab output of amplitude distributions collected over multiple measurements. For clarity and granularity, this graph only has resonant frequencies and harmonics. It does not depict sidebands.

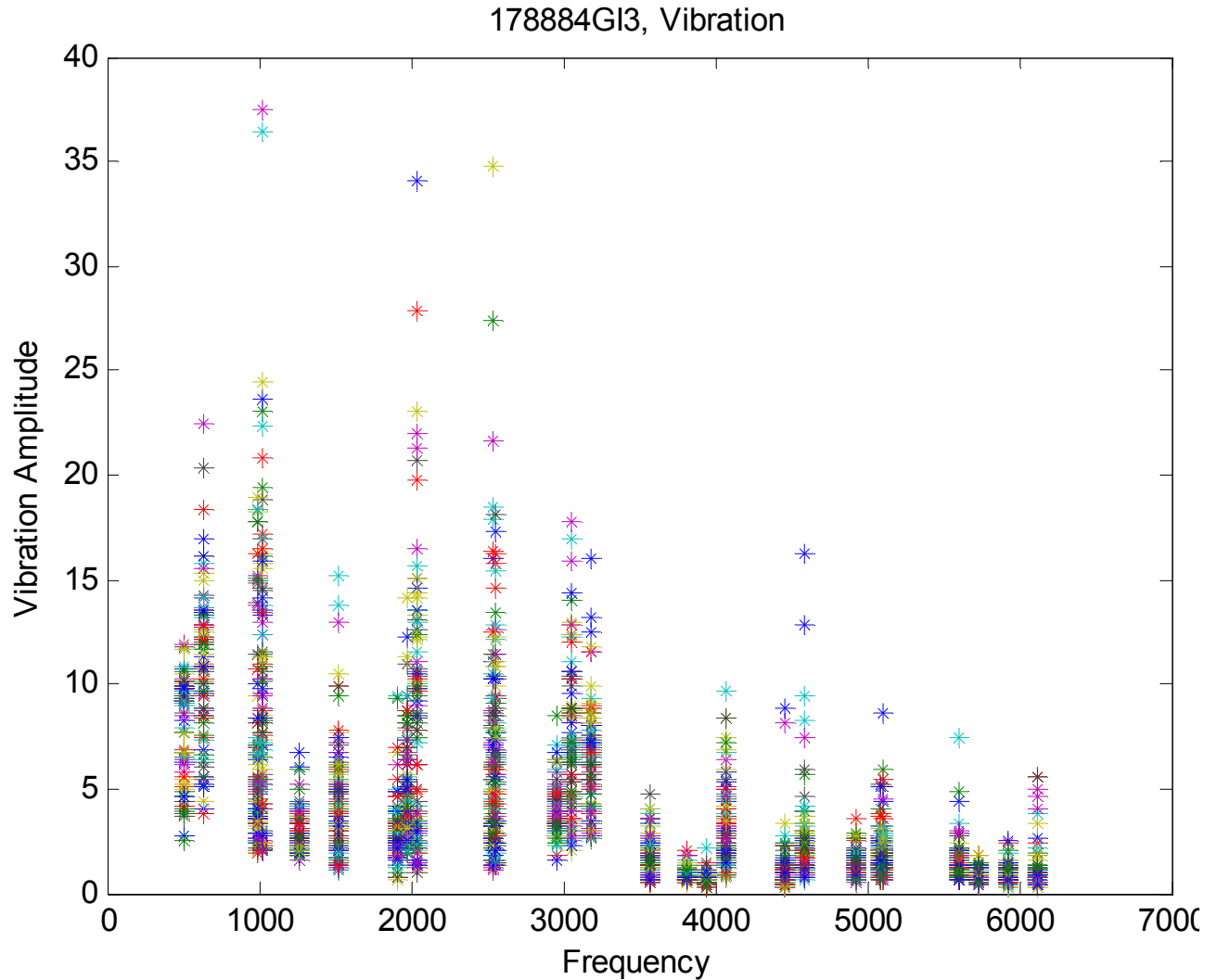


Figure 4.19: Example of Matlab vibration amplitude output of resonant frequencies and harmonics.

The above graph is a good visual example of the spread of the data. Each frequency has a column of data points (stars) where each star represents an amplitude of a different measurement. Each frequency has the same number of data points because every measurement spreads out across the entire frequency range (i.e. one vibration measurement puts a data point at every frequency).

Several of the columns of measurements were individually plotted in a histogram to understand the type of amplitude distribution across measurements. The following is an example of the vibration amplitudes of a single bearing at the outer race defect frequency:

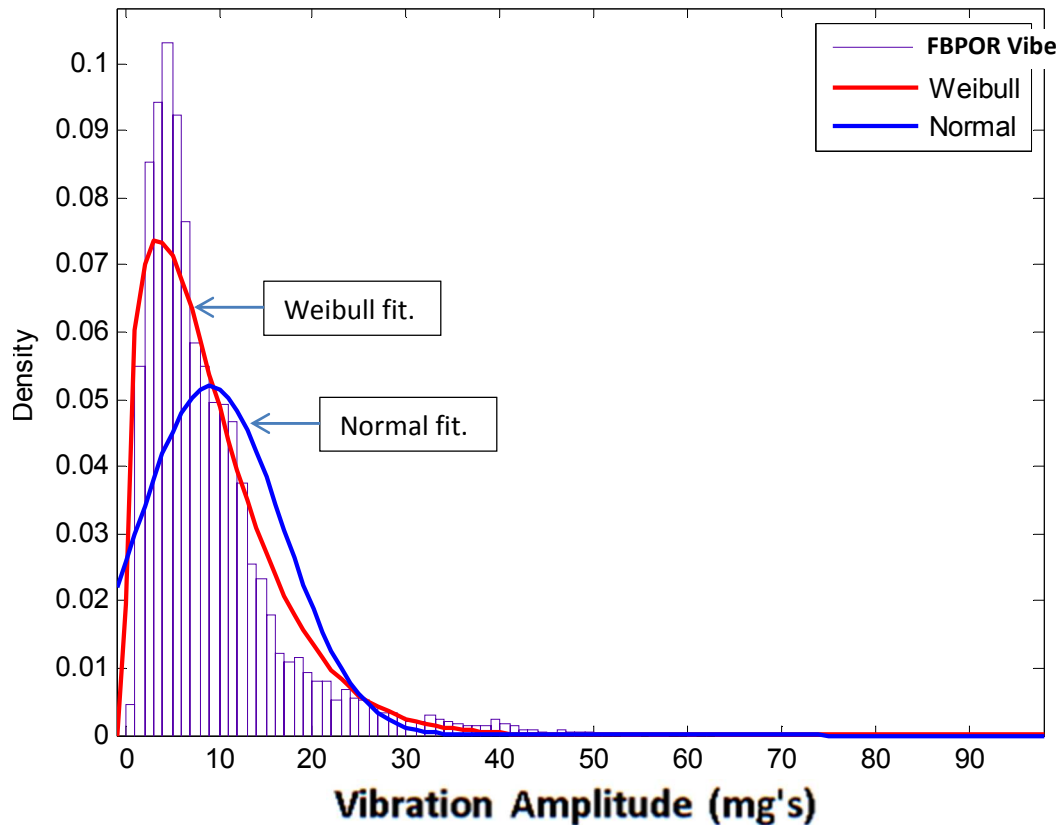


Figure 4.20: Probability density function of outer race defect frequency vibration amplitude distribution.

A visual inspection of the plot indicates the distribution more closely follows that of Weibull statistics, certainly better than a normal distribution. This observation is made multiple times across many frequencies, so it is assumed Weibull statistics describe vibration amplitude distributions.

The Weibull distribution was originally developed for life analysis. It is a means to predict failures, warranty costs, and spare part and/or replacement needs for preventative

maintenance [1]. The model is applicable to vibration distribution because of its versatility to describe a variety of different trends within the same equation.

The Weibull probability density function is characterized as:

$$f(T) = \frac{\beta}{\eta} \left(\frac{T}{\eta}\right)^{\beta-1} e^{-\left(\frac{T}{\eta}\right)^\beta}$$

Equation 4.2: Weibull probability density function.

where β is the shape or slope parameter and η is the scale parameter. The shape parameter controls the behavior of the trend line and has the ability to reduce down to other trends, such as exponential or normal distributions.

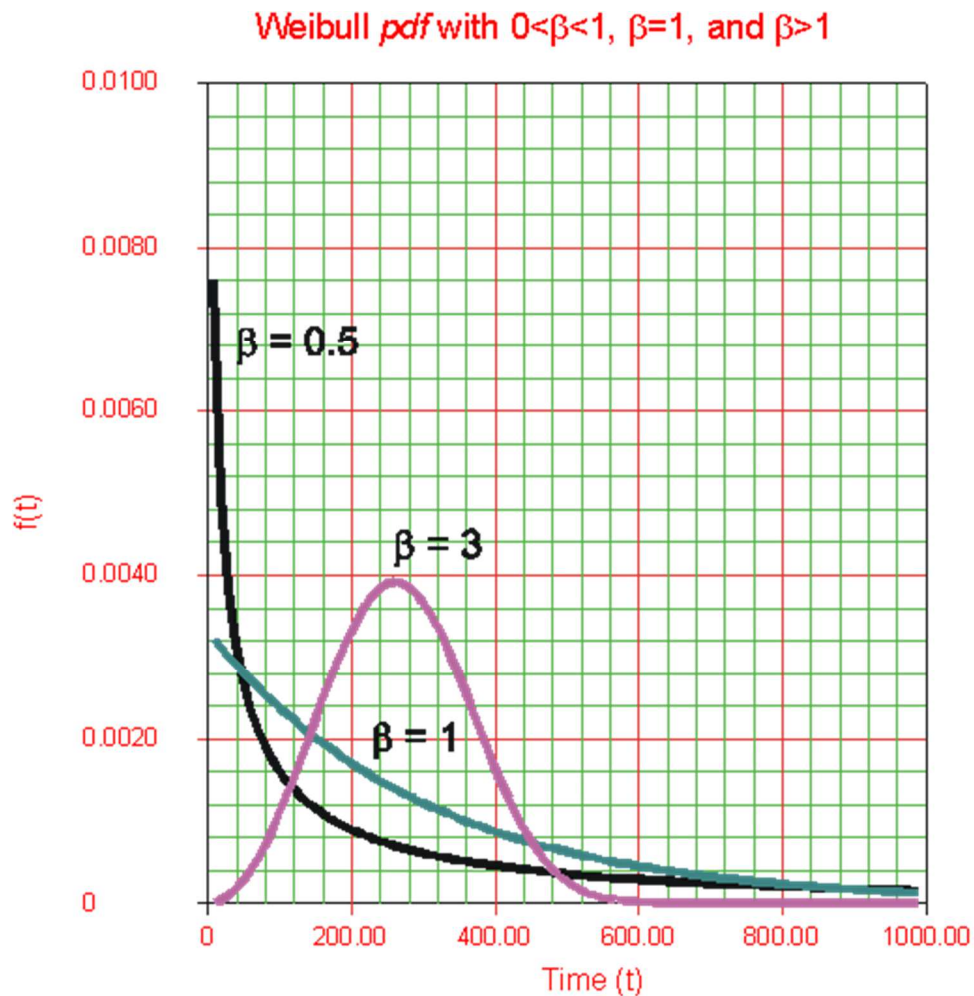


Figure 4.21: Weibull distribution examples with differing effects of the shape parameter β [42].

The figure illustrates the far-reaching implications of a Weibull analysis [1,42]. The versatility of the equation directly led to the decision to use Weibull statistics to describe vibration amplitude distributions at each frequency of interest.

β represents the spread or skewness of the data while η represents the characteristic vibration amplitude of the distribution. η is not an average. It is the value at which 63.2% of the amplitudes will fall below. If we define good vibration to be one that has both a low amplitude and a tight packing, we want to minimize both β and η . In a practical sense, the minimization of β and η will yield a predictable/repeatable low-level vibration of which to describe the bearing.

Consider the following example that depicts the application of Weibull statistics to compare the performance of two bearings. The two distributions below were measured during the course of this work for the outer race defect amplitudes and are compared to illustrate the implications of minimizing both β and η . The blue population on the left has a tighter distribution β as well as a lower characteristic amplitude η than that of the black distribution on the right.

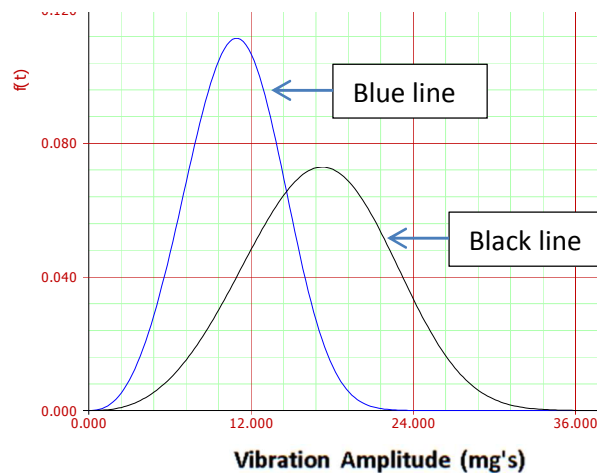


Figure 4.22: Two Weibull probability density functions to compare defects between bearings.

The Weibull statistics are:

	Blue Population	Black Population
β	3.4874	3.5905
η	12.05mG $\left[\frac{mm}{s^2}\right]$	18.92mG $\left[\frac{mm}{s^2}\right]$
ρ^2	0.9795	0.9578

Table 4.3: Example of Weibull statistics of outer race vibration amplitude distributions.

One can now conclude the outer race of the blue population to be statistically 1/3rd less in magnitude and less sporadic. The third term ρ^2 is similar to the r^2 term in a linear regression analysis, which is a measure of how well the model fits the data. A value of 1 indicates a perfect fit, so the distributions both follow Weibull statistics with greater than 95% of the data being explained [11].

4.2 Vibration Transfer Function

A vibration transfer function is one of several applications appropriate for the concepts proved out with the vibration analysis technique of this thesis. The goal is to find a linear relationship between Weibull parameters of the test rig and casing level within a given confidence interval. In this manner, one may measure vibration on the test rig and predict performance at the casing/assembly level.

4.2.1 Visual Observations

Data from like bearings of each measurement system are first plotted against one another to visually inspect correlation between one another, a first-pass evaluation. Two examples are presented below in the next few pages. Please see the appendix for the full set graphs of all ten bearings.

The graph on this page is an example of correlation between the vibration of a bearing at casing level and the same bearing tested in the anode rig. The red data is the bearing tester whereas the blue spectrum is the casing level data, both representative of the same bearing. Through visual inspection, it is seen that lower frequency ranges, which include the resonant frequencies of the bearing, show mild visual correlations between the two systems. However, there are consistently poor visual correlations when reviewing harmonic frequencies. Notice peaks/troughs of the data are not in sync with one another after 1600Hz.

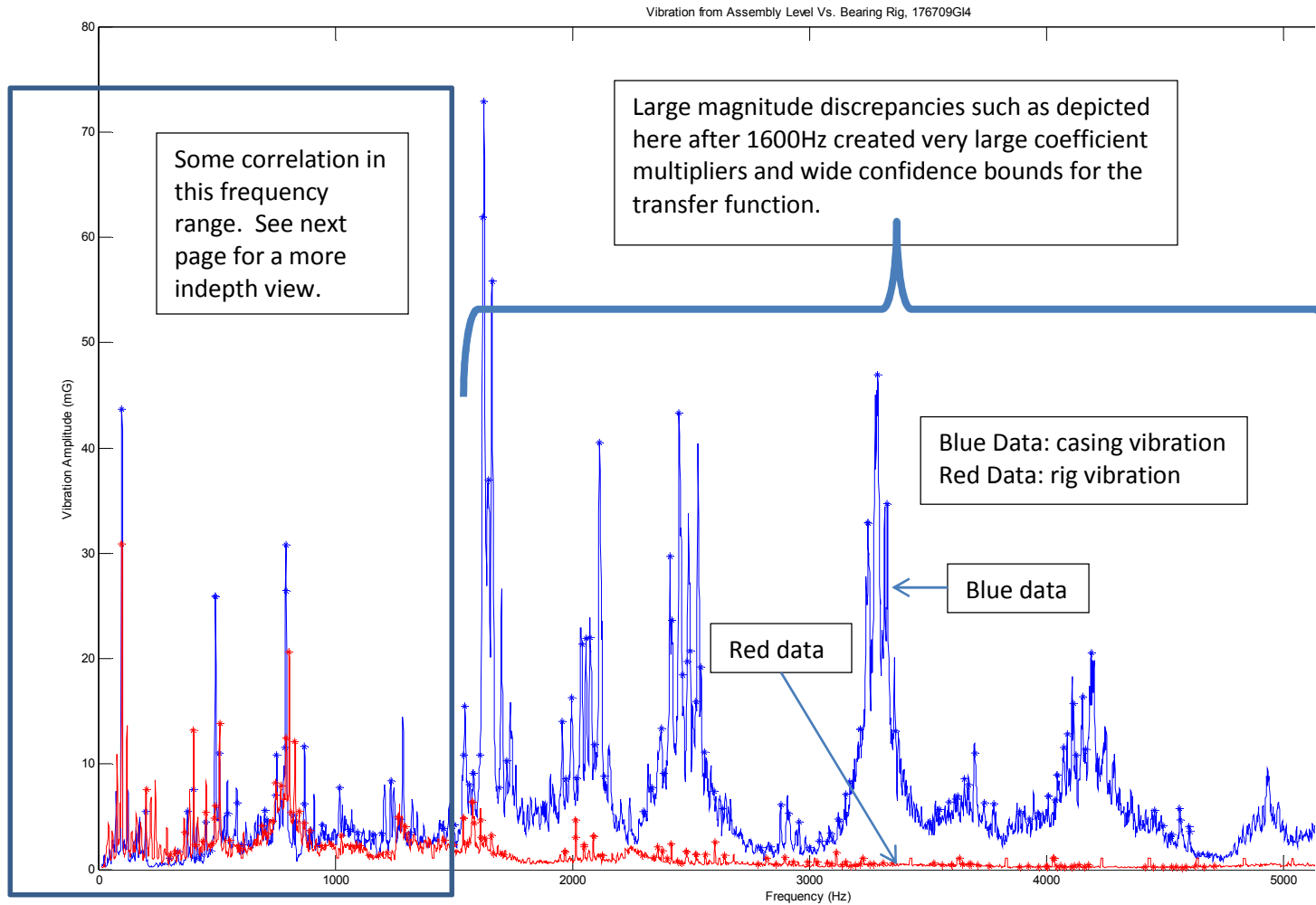


Figure 4.23: Example 1 of casing level vibration compared against bearing rig, 0-5000Hz.

This is a zoomed-in view of the previous graph. Notice that within the lower frequencies, the macro trends are in synch with one another.

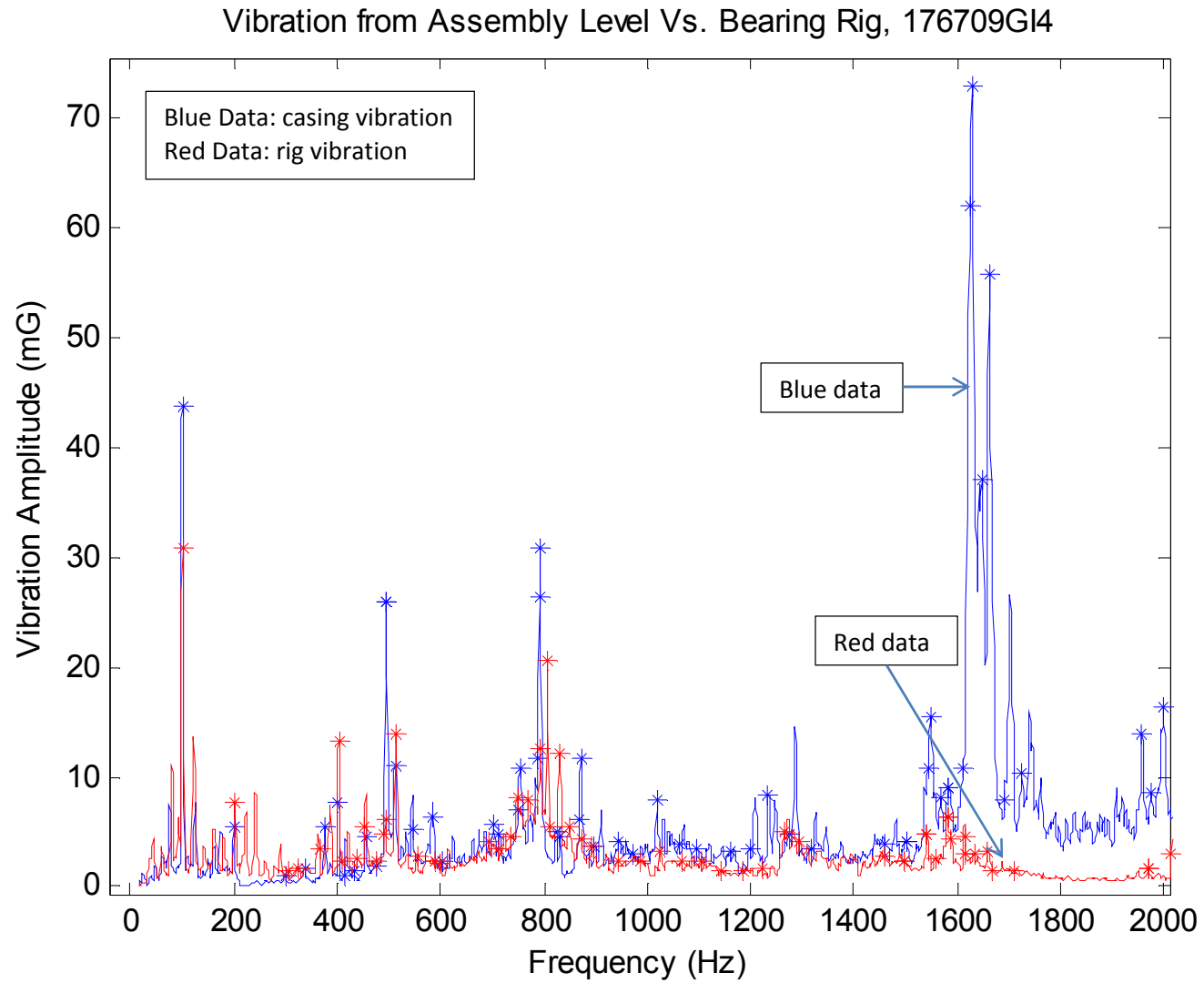


Figure 4.24: Example 1 of casing level vibration compared against bearing rig, 0-2000Hz.

The graph on this page is an example of a bearing that has slightly better visual correlation (as compared to Figure 4.24), even into some harmonics, between the two test systems. Macro peaks and troughs are mildly in sync with one another, through visual analysis. However, poor correlation exists beyond about 3200Hz.

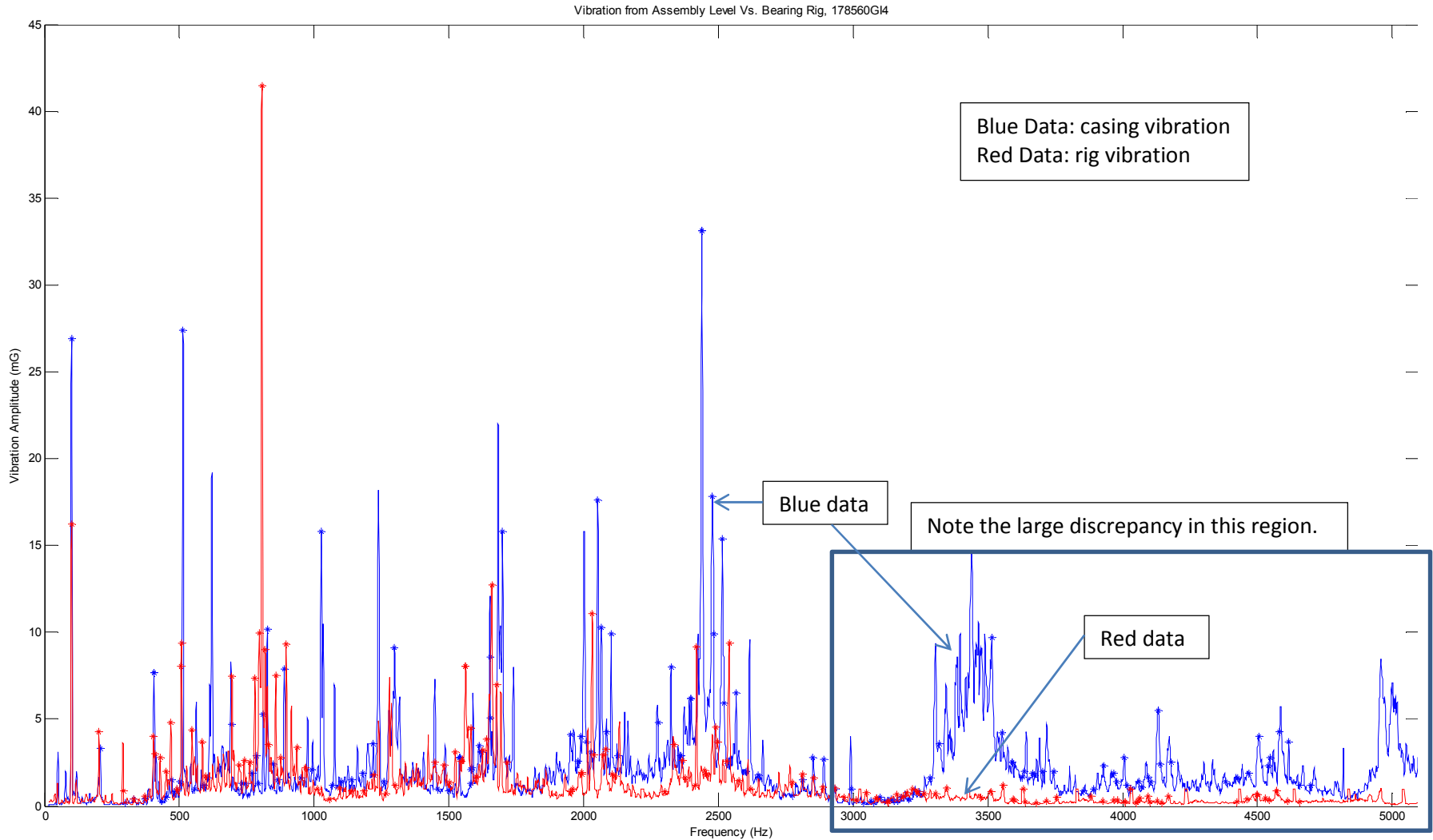


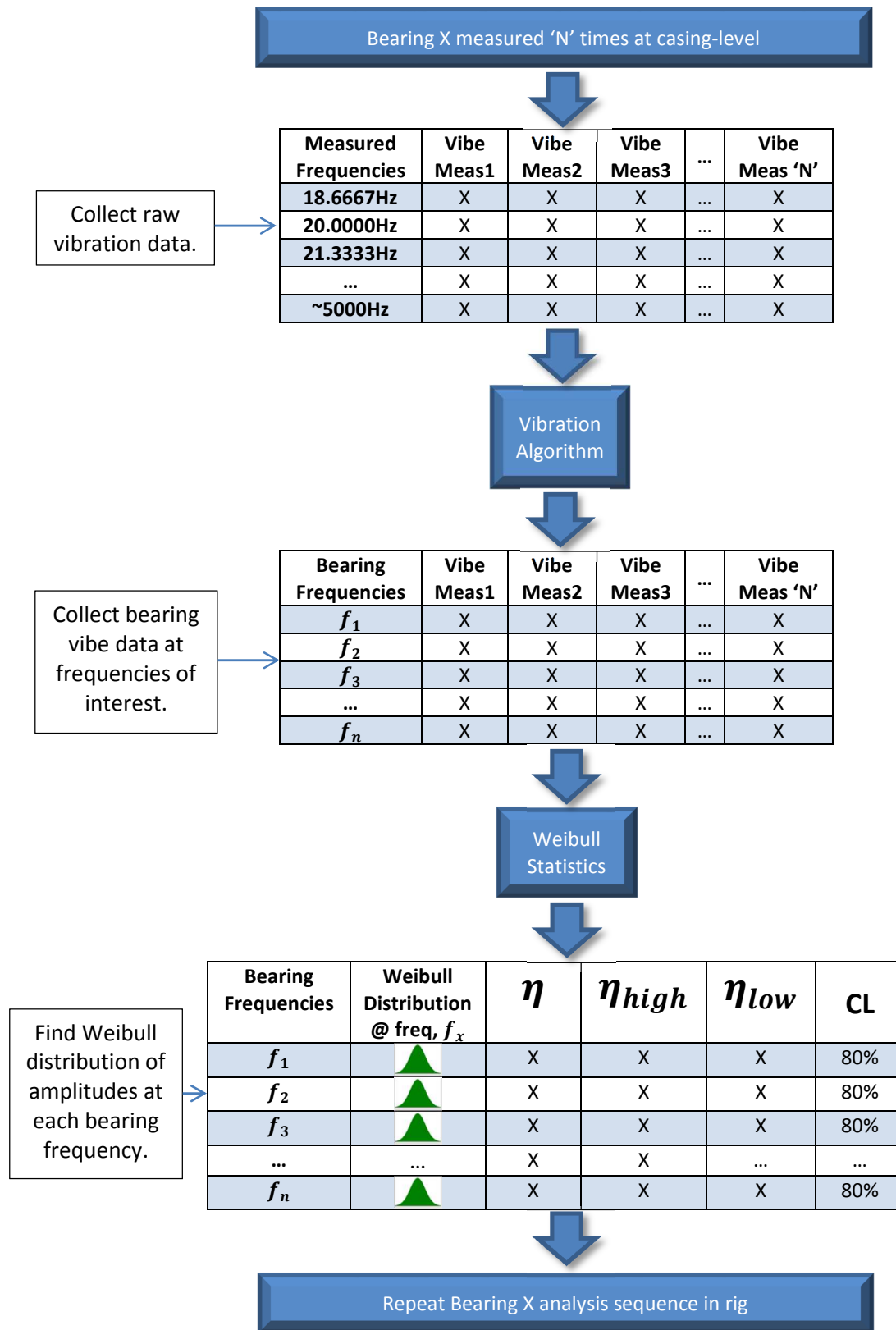
Figure 4.25: Example 2 of casing level vibration compared against bearing rig.

There are a few reasons that may explain poor visual correlation. The bearings used in this test are discrepant material that did not pass noise and vibration requirements for production-quality systems. This may have negatively influenced the results because their performance is inherently less predictable, more sporadic, and not representative of the intended operation. Additionally, there may truly be more system interactions at the casing level beyond 3kHz not represented in the test rig. Both of these hypotheses would have to be further tested with many more bearings. More sampling and more bearings of production quality should smooth large discrepancies to what then can be considered more of a valid snapshot of the true population of vibration amplitudes. Please see the appendix for the full set graphs of all ten bearings.

4.2.2 Bearing Test Rig and Casing Measurement System Correlation Methodology


The process flow block diagram to gather and analyze data for the transfer function follows on the next page. Each bearing is measured multiple times on each system. Each measurement is then fed into the Matlab algorithm to parse the data down to vibration-related frequencies and amplitudes per the script. The distribution of vibration amplitudes on a per bearing, per system, per frequency basis are statistically described with Weibull parameters.

Figure 4.26: Diagram of Data Collection and Analysis for Transfer Function Development



The process flow is repeated for ten different bearings. Each bearing's vibration, at each frequency, is now statistically described with the Weibull eta (η) value in both systems with 80% confidence. That is, the upper and lower eta values bound an 80% confidence interval in which to find the characteristic eta value of the bearing vibration at a single frequency. The following table is an output of a single bearing tested at casing level. For this example, there are 7 vibration measurements to determine the eta value and its interval at each frequency. Two sets of tables such as this exist for each bearing, one for the rig and one for the casing.

80% eta confidence interval



<i>Freqs</i>	<i>Vibe₁</i>	<i>Vibe₂</i>	<i>Vibe₃</i>	<i>Vibe₄</i>	<i>Vibe₅</i>	<i>Vibe₆</i>	<i>Vibe₇</i>	η	η_{high}	η_{low}
100	26.3	27.5	26.2	26.7	27.1	26.9	28.2	27.3	27.0	27.7
200	1.2	0.9	0.8	1.1	1.3	1.3	1.2	1.2	1.1	1.3
300	0.2	0.2	0.3	0.3	0.4	0.3	0.3	0.3	0.3	0.3
330	0.6	0.4	0.3	0.5	0.6	0.5	0.5	0.5	0.5	0.6
370	1.1	1.0	0.9	1.1	1.4	1.0	1.1	1.2	1.1	1.2
400	13.6	13.7	13.8	13.5	14.0	13.7	13.7	13.8	13.7	13.9
409	4.0	1.9	2.8	2.3	3.0	2.6	2.7	3.0	2.7	3.4
433	0.7	0.7	0.6	0.5	0.5	0.5	0.5	0.6	0.6	0.7
449	4.0	3.5	4.4	4.2	3.2	3.3	3.8	4.0	3.8	4.2
472	2.0	2.0	2.0	3.0	3.5	2.5	2.9	2.8	2.5	3.1
488	4.0	2.2	2.3	2.8	3.8	2.7	3.6	3.3	3.0	3.7
500	5.3	4.3	4.8	4.3	4.9	4.1	4.5	4.8	4.6	5.0
511	32.7	33.3	31.1	35.0	29.9	29.3	29.6	32.5	31.5	33.6
551	3.9	4.5	2.6	3.3	3.5	2.7	4.3	3.8	3.5	4.2
590	2.0	1.7	1.1	1.2	1.3	0.9	1.2	1.5	1.3	1.7
600	1.3	1.2	1.3	1.4	1.3	1.4	1.3	1.3	1.3	1.4
700	0.8	0.7	0.9	1.1	1.0	0.9	1.0	1.0	0.9	1.0
710	2.6	3.4	0.7	0.9	1.0	0.9	0.8	1.7	1.2	2.3
740	0.6	0.6	0.7	1.1	1.0	1.0	1.1	1.0	0.9	1.1
749	4.3	3.6	0.7	1.0	1.0	1.0	1.1	2.0	1.4	2.9
779	3.4	1.5	2.5	2.8	2.8	2.5	2.8	2.8	2.6	3.1
789	8.1	5.3	2.5	2.8	2.8	2.5	2.8	4.4	3.4	5.6
800	8.1	5.3	5.9	6.0	5.6	4.9	5.8	6.4	5.8	7.0

818	37.8	22.2	23.0	24.3	26.6	24.7	21.1	27.9	24.9	31.2
828	12.6	12.8	23.0	24.3	26.6	24.7	21.1	22.7	20.6	25.1
858	4.3	3.0	2.8	3.4	3.1	2.9	3.1	3.4	3.2	3.7
867	8.0	8.2	2.8	3.4	3.1	2.9	3.1	5.1	4.0	6.5
897	1.2	1.1	1.0	0.9	1.5	1.1	1.2	1.2	1.1	1.3
944	1.7	1.2	1.1	1.1	1.3	1.4	1.1	1.4	1.3	1.5
984	3.6	3.9	2.6	3.7	3.3	3.3	3.5	3.6	3.4	3.7
1023	13.5	8.6	11.4	16.0	16.8	19.9	17.6	16.2	14.6	18.0
1062	5.5	3.8	4.1	4.3	5.6	3.8	4.6	4.8	4.5	5.2
1102	1.2	1.5	1.7	1.8	1.2	1.2	1.3	1.5	1.4	1.6
1149	0.8	0.8	0.7	0.7	0.9	0.8	0.9	0.8	0.8	0.9
1188	2.9	1.4	1.9	2.0	2.3	2.2	1.9	2.3	2.0	2.5
1228	13.1	8.7	8.8	8.9	9.5	13.9	7.2	11.0	9.8	12.3
1267	7.1	4.5	5.6	7.8	7.1	8.2	5.6	7.1	6.5	7.7
1306	5.9	3.7	3.3	3.8	4.8	4.4	5.2	4.8	4.4	5.3
1456	1.3	1.1	0.8	1.1	1.1	0.8	0.9	1.1	1.0	1.2
1495	1.3	1.1	1.0	1.0	1.1	0.8	1.0	1.1	1.0	1.2
1498	1.1	1.1	0.9	1.2	1.6	1.0	1.0	1.2	1.1	1.4
1534	1.2	1.1	1.7	2.1	2.0	2.1	1.8	1.9	1.7	2.0
1538	1.0	1.1	1.5	0.7	0.7	0.6	0.8	1.0	0.9	1.2
1558	1.2	1.1	1.0	2.8	2.4	2.5	2.3	2.1	1.8	2.5
1574	5.0	6.3	4.0	2.4	2.5	2.0	2.3	4.0	3.2	4.9
1577	4.5	6.3	2.9	2.9	2.6	2.5	2.4	3.9	3.2	4.7
1597	1.7	1.2	1.9	1.5	2.6	1.3	1.9	1.9	1.7	2.2
1613	1.6	1.2	1.0	1.2	1.5	1.3	1.1	1.4	1.3	1.5
1616	4.0	1.2	1.4	1.2	1.6	1.3	1.3	2.0	1.5	2.5
1637	8.6	5.1	6.6	5.7	8.1	9.5	5.8	7.7	6.9	8.5
1656	10.2	3.4	4.8	5.2	7.8	9.5	5.6	7.5	6.3	8.8
1676	2.7	1.9	2.0	2.7	3.7	3.0	2.3	2.8	2.6	3.2
1715	0.9	0.8	1.2	1.8	2.2	1.2	1.1	1.5	1.2	1.8
1967	1.5	2.0	2.8	2.7	2.2	2.7	3.0	2.6	2.4	2.8
...	...									

Table 4.4: Sample data set from bearing 178404GI0 at casing level.

Every bearing frequency has its own amplitude distribution, and each test system yields different distributions. Conceptually, the following graph illustrates the data between the two systems as a means to understand the goal of the transfer function. The upper set of three sine waves represents the casing level data and the lower set of three sine waves represents the rig

data. The solid lines represent the characteristic eta (η) values while the dotted/hashed lines indicate the confidence bounds (η_L, η_H) of that characteristic eta value. The goal of the transfer function is to describe the relationship between the two systems at each bearing frequency.

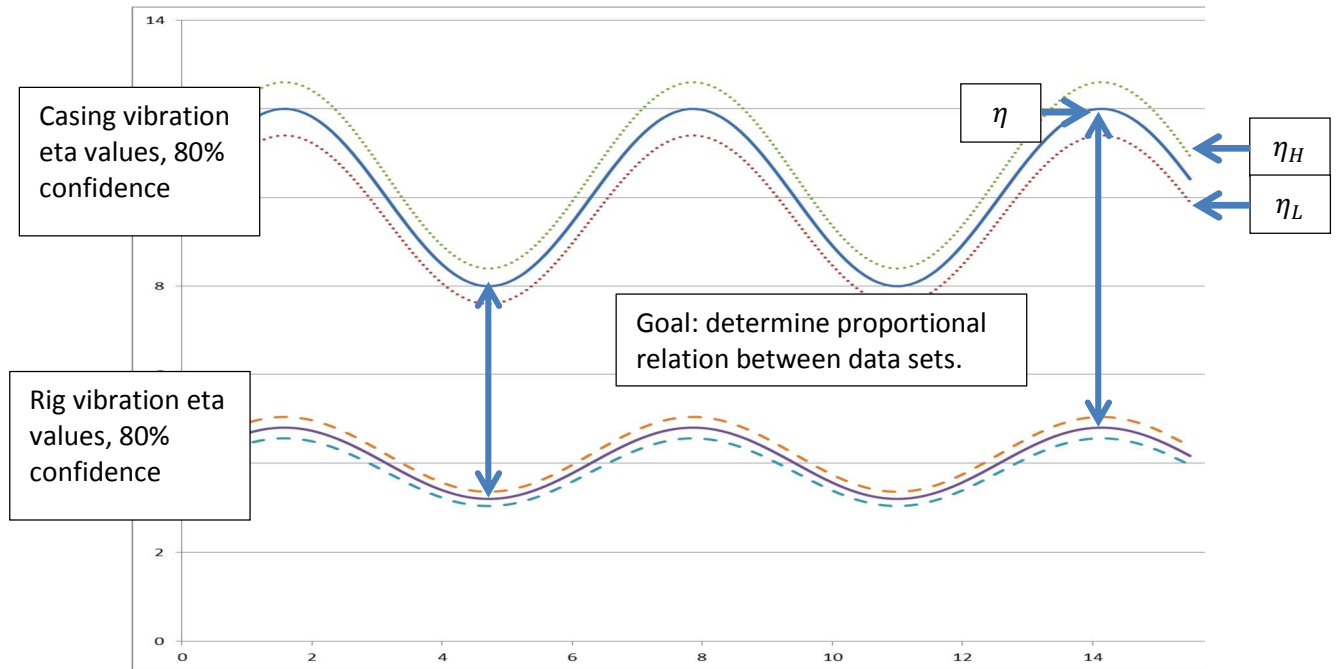


Figure 4.27: Conceptual example of different system responses for the same bearing.

The transfer function between systems is defined as a linear relation for η , η_L , and η_H , as follows:


$$T_{fer} = \frac{Casing_{vibe}}{Rig_{vibe}} @ \text{each frequency}$$

Equation 4.3: Generalized transfer function.

The purpose of the transfer function is to use vibration data gathered on the test rig to predict performance at the casing level. The transfer function will be used as a multiplier against given rig vibration. Mathematically, this would cancel out the “ Rig_{vibe} ” in the equation.

Ten bearing-specific transfer functions are determined (one for each bearing): i.e. Bearing 1 at casing level divided by Bearing 1 at rig level for η , η_L , and η_H , etc, for all ten bearings. It is observed that the transfer function is not consistent from bearing to bearing.

90% CI of Tfer eta values



Bearing:	1	2	3	4	5	6	7	8	9	10	<i>Stats of Tfer</i>		
T_{fer}	$\frac{\eta_{case}}{\eta_{rig}}$	$\frac{\eta_{case}}{\eta_{rig}}$	$\frac{\eta_{case}}{\eta_{rig}}$	$\frac{\eta_{case}}{\eta_{rig}}$	$\frac{\eta_{case}}{\eta_{rig}}$	$\frac{\eta_{case}}{\eta_{rig}}$	$\frac{\eta_{case}}{\eta_{rig}}$	$\frac{\eta_{case}}{\eta_{rig}}$	$\frac{\eta_{case}}{\eta_{rig}}$	$\frac{\eta_{case}}{\eta_{rig}}$	η	η_{high}	η_{low}
100Hz	1.20	1.33	1.08	1.07	1.88	2.02	0.28	1.34	1.06	2.03	1.48	1.16	1.89
200Hz	0.53	1.15	0.06	0.95	0.50	0.04	0.08	0.86	0.16	1.21	0.56	0.27	1.18
300Hz	0.73	0.80	0.05	0.79	0.25	0.03	0.01	0.69	0.93	0.68	0.49	0.24	1.04
330Hz	0.74	1.29	0.60	0.61	1.18	0.31	0.30	0.89	0.66	0.95	0.85	0.63	1.15
370Hz	1.77	1.85	1.47	0.71	0.75	0.97	1.07	0.55	0.80	0.85	1.22	0.87	1.67
...

Table 4.5: Bearing specific transfer function of eta values.

The inconsistent nature of the individual transfer functions makes it necessary to bound the population of η , η_L , and η_H values with their own confidence intervals. The data in the previous table for η illustrates the necessity to create a distribution of the individual ten transfer functions to understand their central tendency and create a generalized transfer function. This concept is repeated for η_L , and η_H transfer functions.

At this point, the transfer function is described with three sets of curves as illustrated in the following figure:

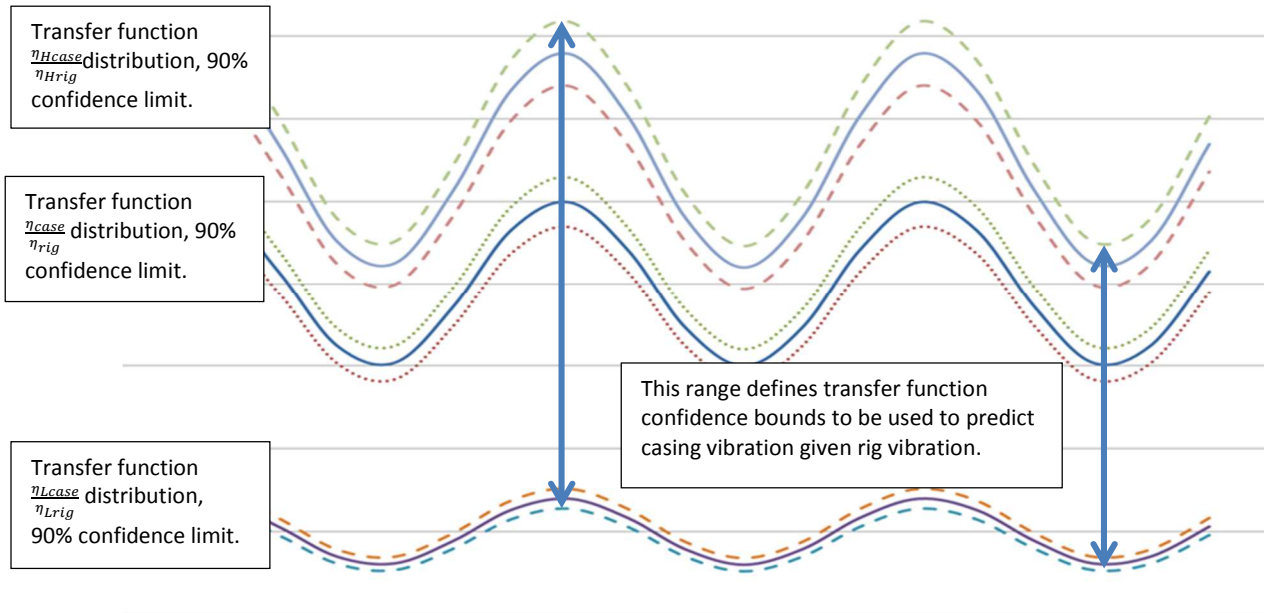


Figure 4.28: Conceptual review of the confidence intervals of the transfer function.

From top to bottom, the sets of curves represent transfer functions for η_H , η , and η_L with confidence intervals. This illustrates that the transfer function has a wide range of possible values, and this range creates the amplitude bounds in a predictive model given rig vibration.

The final transfer function is visually defined by the arrows in the above figure. It is bounded by the upper limit of η_H and the lower limit of η_L as indicated by the arrows. The range of multipliers will yield a range of vibration values at the casing level, given rig vibration, with a 72% confidence interval. 72% confidence is a product of an 80% and a 90% statistical stackup. Now the bearing rig can be used as a DOE enabler because there is a known relationship between the sub-assembly and assembly-level systems.

4.2.3 Effectiveness of Transfer Function

The transfer function is designed to be a means to measure vibration on a test rig and predict the interval in which to expect the η values at casing level. The high-level conclusion is that prediction across the spectrum is about 50% accurate: the predicted η value falls between the upper and lower confidence bounds half the time. The following graph plots the average accuracy of 10 bearings per frequency.

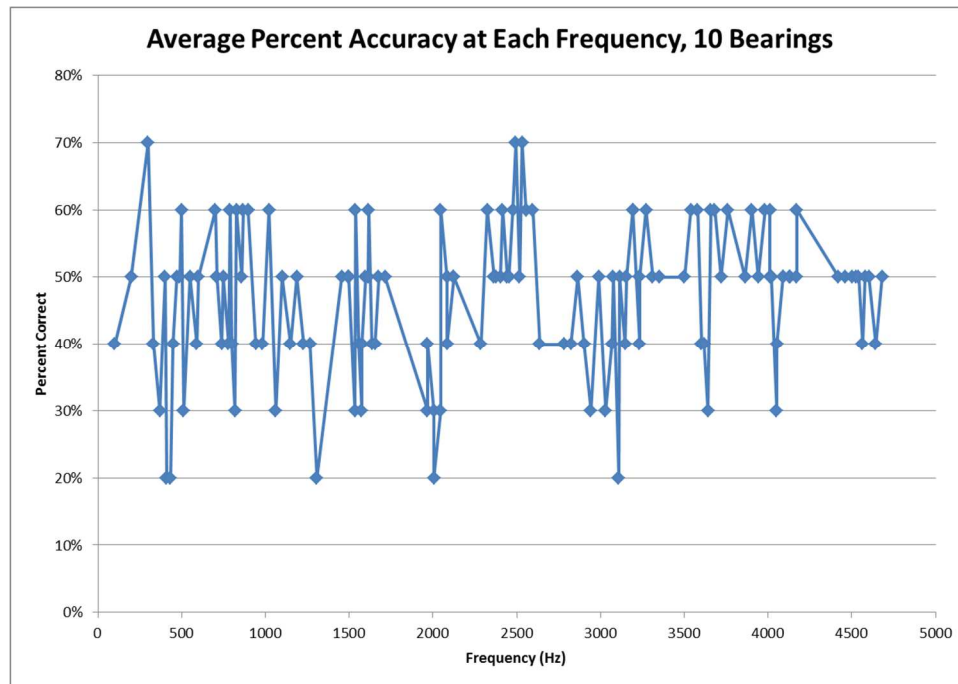


Figure 4.29: Graph of percent accuracy at each frequency for ten bearings.

The overall accuracy for ten predictions is:

Bearing:	1	2	3	4	5	6	7	8	9	10	Avg%
Avg% Correct:	72.2%	15.8%	36.8%	56.4%	51.9%	33.1%	30.1%	64.7%	39.1%	70.7%	47.1%

Table 4.6: Accuracy of transfer function for ten predictions.

The next two pages review the most and least well-correlated bearings as predicted by the transfer function. Please see the appendix for graphical evaluation examples for all ten bearings.

Casing vibration is plotted against the vibration confidence intervals to review effectivity of prediction. It should again be noted again that the plot is of only bearing frequencies. Blue is the upper bound expected, red is the lower bound, green is the actual measured eta vibration at casing level. Any green data that falls within the red and blue boundaries is a successful prediction: the data falls within the 72% confidence eta interval. This first graph is 72% accurate overall and is the best correlation of all ten tests.

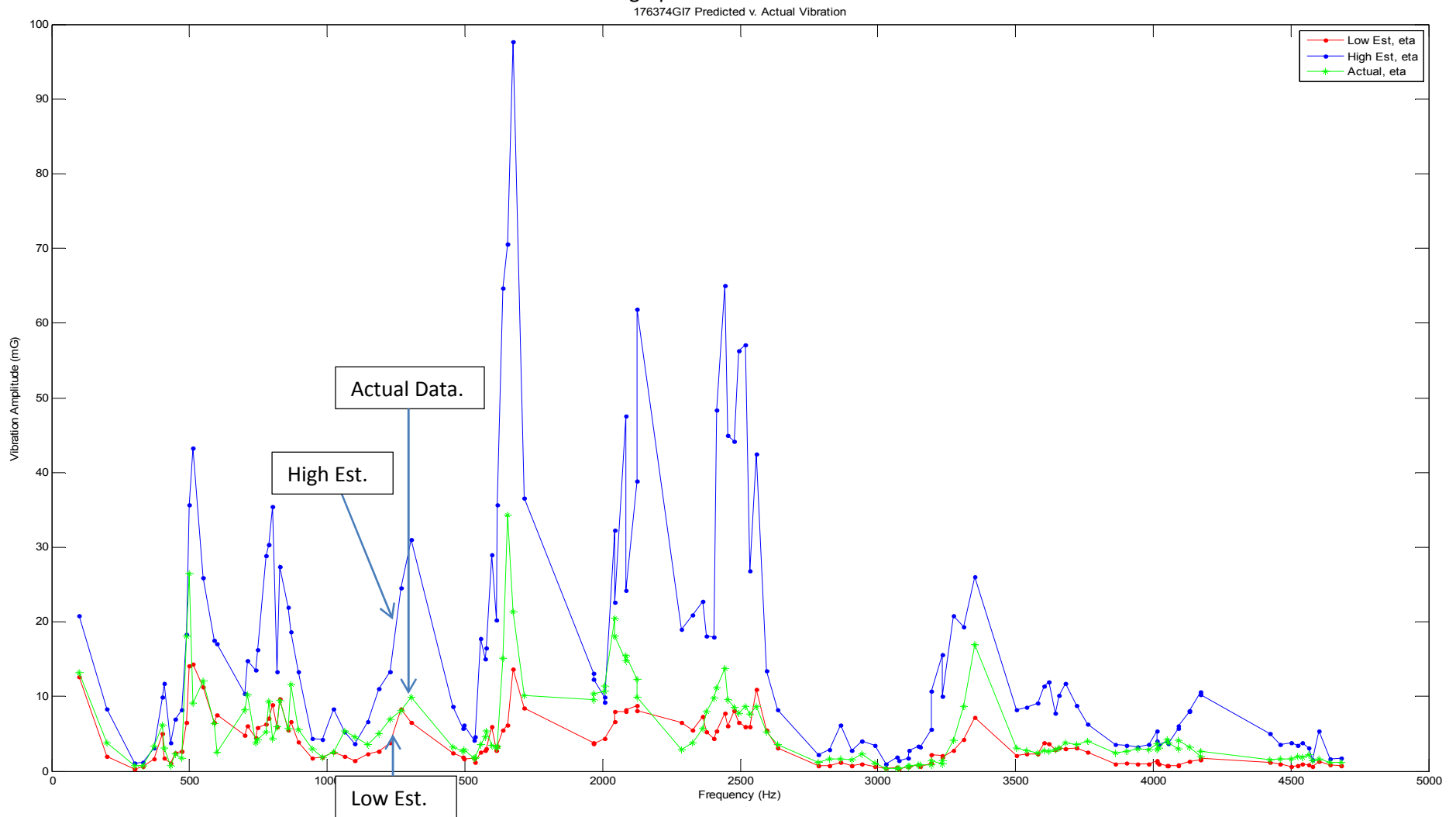


Figure 4.30: Transfer function with the best correlation between predicted and measured data at casing level.

This second graph is 15% accurate and represents the worst correlation of all tests. This is the only bearing where the casing vibration is significantly higher than when tested on the rig. The rig vibration was so low that it skewed the prediction to lower magnitude intervals.

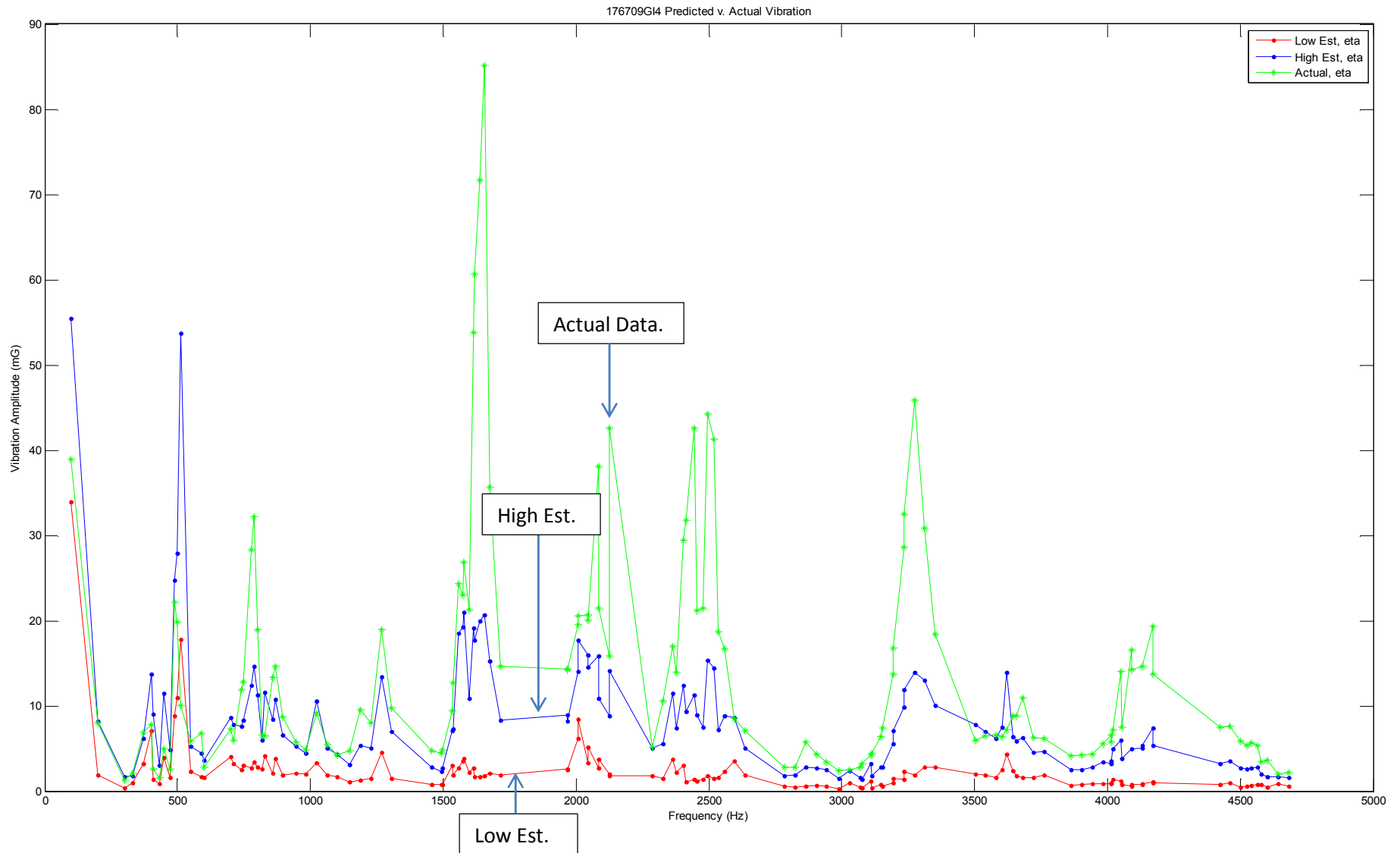


Figure 4.31: Transfer function with the worst correlation between predicted and measured data at casing level.

5 Conclusions and Recommendations

Ball bearings with solid lubrication lack the damping mechanisms of oil and produce theoretically well-defined vibration characteristics based upon given geometry and speed of operation. It is shown that the application of bearing theory, Monte Carlo simulation, and Order Analysis in a Matlab program to track bearing performance is promising. The uncertainty of finding the empirical peak within a range of theoretical frequencies is reduced by greater than 70% with order analysis. It is concluded that normalization is a very powerful means for strengthening relationships of characteristic frequencies between data sets.

The practical implications of the work presented give the bearing engineer additional tools to optimize designs for life and noise by tracking component condition during operation. The tool's concepts were tested and verified through the creation of a vibration transfer function between a sub-assembly bearing test rig and a bearing at final casing/assembly level. The vibration transfer function, developed with Weibull statistics, correctly described distributions of vibration amplitude approximately 50% of the time within a 72% confidence interval.

It is recommended that future work focus on creating a generalized transfer function with a larger sample size. This work used ten casing/rig relations to create a set of ten bearing-specific transfer functions to develop a generalized function. Additionally, the bearings used in this test were of discrepant material that did not pass noise and vibration requirements for production-quality systems. This may have negatively influenced the rig/casing correlation results because their performance is inherently less predictable, more sporadic. Samples in the future should be of sufficient quality to adequately represent the intended design of operation. However, it is important to note that, within each respective system, each measurement had good visual resemblance between one another, indicating the method of analysis and data

collection to be accurate. It is also recommended that future work use the algorithm developed to test bearing designs against one another. The algorithm can be used in the future to track vibration performance over the life of a bearing. Designs could be evaluated and optimized in this manner. For example, the algorithm may be especially useful to track bearing run in. A transfer function is only a single example of the application's use.

BIBLIOGRAPHY

1. Abernethy, Robert B. *The New Weibull Handbook*. North Palm Beach, FL: R.B. Abernethy, 2008. Print.
2. *ABMA STD 9*. 90th ed. N.p.: American Bearing Manufacturers Association, n.d. Print.
3. Albanetti, Edward, and Robert O'Donnell. Ball Bearing Design Temperature Compensating X-ray Tube Bearing. Schaeffler Kg, assignee. Patent US20090268874 A1. 29 Oct. 2009. Print.
4. Angular Contact Load Image. Digital image. N.p., n.d. Web. 6 Sept. 2014. <http://e-katalog.home.pl/cx_bearings/poradnik.php?lang=EN&gr=3&pod=7&sub=3>.
5. Basulto, Dominic. "Humans Are the World's Best Pattern-Recognition Machines, But for How Long? | Big Think." Big Think, 24 July 2013. Web. 25 Nov. 2014. <<http://bigthink.com/endless-innovation/humans-are-the-worlds-best-pattern-recognition-machines-but-for-how-long>>.
6. "Box Plot." *1.3.3.7. Box Plot*. National Institute for Standards and Technology, n.d. Web. 04 Oct. 2014. <<http://www.itl.nist.gov/div898/handbook/eda/section3/boxplot.htm>>.
7. Bruers, Adam. "Auto Repair Do It Yourself (DIY) Car Repair Blog." *Do-it-yourself | Auto Repair Do It Yourself (DIY) Car Repair Blog in Woodbury, MN*. Auto Works Automotive Service Center, 21 Nov. 2014. Web. 23 Nov. 2014. <<http://info.autoworksmn.com/auto-repair-blog/?Tag=do-it-yourself>>.
8. Copping, Mark. "Vibration Analysis Reporting - Bearing Failure Stages & Responses." *Articles*. Reliability Web, n.d. Web. 23 Nov. 2014. <http://reliabilityweb.com/index.php/articles/vibration_analysis_reporting_-_bearing_failure_stages_responses>.
9. "Envelope Analysis - Type 7773." Bruel and Kjaer, n.d. Web. 06 Dec. 2014. <<http://www.bksv.com/Products/analysis-software/signal-analysis/envelope-analysis/envelope-analysis-7773?tab=descriptions>>.
10. Friedman, Alan. "Understanding the Role of Linearity in Vibration Analysis - Maintenance Technology." *Maintenance Technology*, 01 Sept. 2003. Web. 20 Nov. 2014. <<http://www.maintenancetechnology.com/2003/09/understanding-the-role-of-linearity-in-vibration-analysis/>>.
11. Frost, Jim. "Regression Analysis: How Do I Interpret R-squared and Assess the Goodness-of-Fit?" *Regression Analysis: How Do I Interpret R-squared and Assess the Goodness-of-Fit?* Minitab, 30 May 2013. Web. 18 Jan. 2015.

- <<http://blog.minitab.com/blog/adventures-in-statistics/regression-analysis-how-do-i-interpret-r-squared-and-assess-the-goodness-of-fit>>.
12. Ganeriwala, Suri. "Review of Techniques for Bearings and Gearbox Diagnostics." IMAC Conference. Jacksonville. 3 Feb. 2010. Lecture.
 13. Hamrock, Berard J., and Duncan Dowson. *Ball Bearing Mechanics*. Tech. N.p.: NASA Technical Memorandum 81691, 1981. Print.
 14. "The Hanning Window." *The Hanning Window*. Azima DLI, 2009. Web. 17 Jan. 2015. <<http://www.azimadli.com/vibman/thehanningwindow.htm>>.
 15. Harris, Tedric A. *Rolling Bearing Analysis*. New York: John Wiley, 2001. Print.
 16. Hattori, Hitoshi, Harunobu Fukushima, Yasuo Yoshii, Hironori Nakamuta, Mitsuo Iwase, and Koichi Kitade. "Proposal of a High Rigidity and High Speed Rotating Mechanism Using a New Concept Hydrodynamic Bearing in X-Ray Tube for High Speed Computed Tomography." *Journal of Advanced Mechanical Design, Systems, and Manufacturing* 3.1 (2009): 105-14. Web.
 17. Johnson, K. L. *Contact Mechanics*. Cambridge: Cambridge UP, 1985. Print.
 18. Konstantin-Hansen, Hans, and Henrik Herlufsen. "Envelope and Cepstrum Analyses for Machinery Fault Identification." *Sound and Vibration* (2010): 10-12. Print.
 19. Lacey, Steve J. "An Overview of Bearing Vibration Analysis." *Maintenance and Asset Management* 23.6 (2008): 32-42. Print.
 20. Luo, Huageng, George H. Ghanime, and Hai Qiu. Synthesized Synchronous Sampling and Acceleration Enveloping for Differential Bearing Damage Signature. General Electric Company, assignee. Patent US7930111 B2. 19 Apr. 2011. Print.
 21. "Measures of Skewness and Kurtosis." *Measures of Skewness and Kurtosis*. National Institute of Standards and Technology, n.d. Web. 27 Sept. 2014. <<http://www.itl.nist.gov/div898/handbook/eda/section3/eda35b.htm>>.
 22. *Measuring Vibration*. N.p.: Bruel and Kjaer, 1982. Print.
 23. Momono, Tatsunobu, and Banda Noda. "Sound and Vibration in Rolling Bearings." *Motion and Control* 6 (1999): 29-37. Print.
 24. "Monte Carlo Simulation." MathWorks, n.d. Web. 20 Nov. 2014. <<http://www.mathworks.com/discovery/monte-carlo-simulation.html>>.
 25. Montgomery, Douglas C., George C. Runger, and Norma Faris Hubele. *Engineering Statistics*. Hoboken, NJ: John Wiley, 2011. Print.

26. Nadhe, Dharmesh. Time Series Acceleration Signal. Digital image. N.p., n.d. Web. 20 Nov. 2014. <http://i1196.photobucket.com/albums/aa406/dharmesh_nadhe/accleatain_time_domain.jpg>.
27. Parsons, Keith. Time domain vs. frequency domain. Digital image. *WLW052 – 7 Rules for Accurate Site Surveys*. Wireless LAN Professionals, 7 Jan. 2014. Web. 24 Nov. 2014. <<http://www.wlanpros.com/wlw052-7-rules-accurate-site-surveys/>>.
28. Patidar, Shyam, and Pradeep K. Soni. "An Overview on Vibration Analysis Techniques for the Diagnosis of Rolling Element Bearing Faults." *International Journal of Engineering Trends and Technology (IJETT)* 4.5 (2013): 1804-809. Print.
29. Qiu, Liangheng, Carey S. Rogers, Michael J. Danyluk, and Dennis M. Gray. Titanium Carbide plus Silver Coated Balls for X-ray Tube Bearings. General Electric Company, assignee. Patent US7492869 B1. 17 Feb. 2009. Print.
30. Rabinowicz, Ernest. *Friction and Wear of Materials*. New York: Wiley, 1965. Print.
31. "Running-in of Grease Lubricated Bearings." SKF, n.d. Web. 18 Sept. 2014. <<http://www.skf.com/group/products/bearings-units-housings/super-precision-bearings/principles/lubrication/grease-lubrication/running-in-of-grease-lubricated-bearings/index.html>>.
32. Sidebands. Digital image. *Amplitude Modulation*. Reviseomatic, n.d. Web. 20 Nov. 2014. <<http://reviseomatic.org/help/2-modulation/Amplitude%20Modulation.php>>.
33. "Simple Harmonic Motion." *Simple Harmonic Motion*. Hyper Physics, n.d. Web. 24 Nov. 2014. <<http://hyperphysics.phy-astr.gsu.edu/hbase/shm.html>>.
34. "Slip in Electrical Induction Motors." *Slip in Electrical Induction Motors*. Engineering Tool Box, n.d. Web. 25 Nov. 2014. <http://www.engineeringtoolbox.com/electrical-motor-slip-d_652.html>.
35. Stevens, David. "Rolling Element Bearings." *Rolling Element Bearings*. David Stevens, n.d. Web. 22 Nov. 2014. <<http://www.vibanalysis.co.uk/vibanalysis/rolling/rolling.html>>.
36. Tracks through snow. Digital image. Ski Heavenly, n.d. Web. <http://blog.skiheavenly.com/wp-content/uploads/2012/01/snow_tracks.JPG>.
37. Tranter, Jason. "Detecting Bearing Faults." *Articles*. Reliability Web, n.d. Web. 22 Aug. 2014. <http://reliabilityweb.com/index.php/articles/detecting_bearing_faults/>.

38. Tranter, Jason. "Detecting Bearing Faults." *Articles*. Reliability Web, n.d. Web. 22 Aug. 2014. <http://reliabilityweb.com/index.php/articles/detecting_bearing_faults_part_2/>.
39. Tranter, Jason. "Detecting Bearing Faults." *Articles*. Reliability Web, n.d. Web. 22 Aug. 2014. <http://reliabilityweb.com/index.php/articles/detecting_bearing_faults_part_3/>.
40. Triscari, Andrew T. "*Effects of Gallium-Molybdenum Intermetallic on Wear Mechanisms in Herringbone-Spiral Groove Bearing Systems*". Thesis. Milwaukee School of Engineering, 2014. N.p.: n.p., n.d. Print.
41. "Understanding FFT Windows." *LDS ANO14* 1203 (2003): n. pag. LDS Group. Web.
42. "Weibull Distribution: Characteristics of the Weibull Distribution." *Reliability Engineering Resources*. Reliasoft, 2002. Web. 14 Dec. 2014. <<http://www.weibull.com/hotwire/issue14/relbasics14.htm>>.
43. "Windowing: Optimizing FFTs Using Window Functions." National Instruments, 02 July 2014. Web. 17 Jan. 2015. <<http://www.ni.com/white-paper/4844/en/>>.
44. "X-Ray Bearings." *Barden UK Super Precision Ball Bearings*. N.p., n.d. Web. 06 Sept. 2014. <http://www.bardenbearings.co.uk/x_ray_bearings.html>.
45. X-ray Tube. Digital image. *X-Alliance*. N.p., n.d. Web. 5 Sept. 2014. <http://www.x-alliance.com/public/images/components_xraytube.png>.
46. X-ray Tube Schematic. Digital image. *Radiopaedia*. N.p., n.d. Web. 5 Sept. 2014. <http://images.radiopaedia.org/images/3165401/7ef2c07bd518defc594a4328dbfd2b_big_gallery.jpg>.
47. Xu, Weiwei, "*Effect of Bolted Joint Preload on Structural Damping*" (2013). Graduate Theses and Dissertations. <<http://scholarcommons.usf.edu/etd/4794>>.